



TECHNICAL NOTE

D-1781

EFFECTS OF NOSE BLUNTNES, FINENESS RATIO, CONE ANGLE,
AND MODEL BASE ON THE STATIC AERODYNAMIC CHARACTERISTICS
OF BLUNT BODIES AT MACH NUMBERS OF 1.57, 1.80,
AND 2.16 AND ANGLES OF ATTACK UP TO 180°

By David S. Shaw, Dennis E. Fuller,
and C. Donald Babb

Langley Research Center
Langley Station, Hampton, Va.

NATIONAL AERONAUTICS AND SPACE ADMINISTRATION
WASHINGTON

May 1963

N63-15527

code-1

82P

554423

NATIONAL AERONAUTICS AND SPACE ADMINISTRATION

TECHNICAL NOTE D-1781

EFFECTS OF NOSE BLUNTNESS, FINENESS RATIO, CONE ANGLE,
AND MODEL BASE ON THE STATIC AERODYNAMIC CHARACTERISTICS
OF BLUNT BODIES AT MACH NUMBERS OF 1.57, 1.80,
AND 2.16 AND ANGLES OF ATTACK UP TO 180°

By David S. Shaw, Dennis E. Fuller,
and C. Donald Babb

SUMMARY

15527

Static aerodynamic data are presented for 34 blunt bodies which had nose bluntnesses of 0- (spherical), 50-, or 75-percent flat faces, fineness ratios of $1/2$, $3/4$, or 1, cone half-angles of 10° , 15° , or 20° , and bases which were flat, convex, or concave. Tests were performed in the Langley Unitary Plan wind tunnel at Mach numbers of 1.57, 1.80, and 2.16 and through an angle-of-attack range of 180° . The test Reynolds number per foot was about 1.24×10^6 .

The results indicate that, from a static stability standpoint, all the models tested are unsuitable for use as a passive entry vehicle if the vehicle is to enter in the nose-forward condition, since the stable trim points near 180° could not be eliminated by their inherent aerodynamic characteristics. Increases in nose bluntness or fineness ratio and decreases in cone half-angles lead to decreases in stability near angles of attack of 0° . The model base had no effect on the stability near an angle of attack of 0° . Increases in nose bluntness or fineness ratio and decreases in cone half-angles lead to increases in normal force for most of the angle-of-attack range of 180° . The model base had no effect on normal force up to about 90° and only slight effects from 90° to 180° where the convex-base models had the highest values of normal force. Increases in nose bluntness, fineness ratio, or cone half-angles generally lead to decreases in axial force for angles of attack near 0° . The effects of model base are apparent only for angles of attack from 90° to 180° , and at 180° , the concave-base models had the most negative axial force while the convex-base models had the least negative axial force.

INTRODUCTION

The National Aeronautics and Space Administration, and in particular its Jet Propulsion Laboratory facilities, has the prime responsibility of probing

the atmosphere and terrain of Venus and Mars and, at some later date, accomplishing a soft landing on either or both planets. In order to assure the success of such a venture, the shape of the space vehicle to be used must be fixed from its aerodynamic characteristics throughout its entire anticipated speed range. A configuration study, both static and dynamic, is now being carried out in a number of facilities throughout the country to determine the most suitable vehicle shape for such a mission. (One such shape which has been tested extensively is reported in refs. 1 to 4, and reports on similar bodies may be found in refs. 5 to 8.)

As a part of this configuration study, a number of ballistic-shaped bodies which varied in nose bluntness, fineness ratio, cone angle, and model base have been tested in the Langley Unitary Plan wind tunnel. Tests were performed at Mach numbers of 1.57, 1.80, and 2.16 and through an angle-of-attack range of 180° . The test Reynolds number per foot was about 1.24×10^6 . The results of the investigation are presented herein.

SYMBOLS

The coefficients of forces and moments are referred to the body-axis system and are oriented as shown in figure 1. For all models, the aerodynamic moments were taken about a point located one-third of the body length forward of the maximum diameter location.

C_A	axial-force coefficient, $\frac{\text{Axial force}}{qS}$
C_{A_0}	axial-force coefficient at $\alpha = 0^\circ$
C_N	normal-force coefficient, $\frac{\text{Normal force}}{qS}$
C_{N_α}	slope of normal-force curve, $\frac{\partial C_N}{\partial \alpha}$, per deg
C_m	pitching-moment coefficient, $\frac{\text{Pitching moment}}{qSd}$
C_{m_α}	slope of pitching-moment curve, $\frac{\partial C_m}{\partial \alpha}$, per deg
a	diameter of front face of cone frustum, in.
A, B	dimensions used to locate intersection of nose radius with side of model, in.

d	maximum diameter of models, 8.000 in.
K	nose bluntness, percent of flat-face diameter
l	length of models (excluding base), in.
M	free-stream Mach number
p_t	stagnation pressure, lb/sq in. absolute
q	dynamic pressure, lb/sq ft
r	radius at front face of models, in.
R	Reynolds number per foot
S	cross-sectional area at maximum diameter, 0.349067 sq ft
T_t	stagnation temperature, °F
x	distance from maximum diameter to moment center (positive when measured from maximum diameter toward nose), in.
α	angle of attack of model center line, deg
θ	cone half-angle, deg
λ	fineness ratio

APPARATUS AND TESTS

Wind Tunnel

Tests were conducted in the low Mach number test section of the Langley Unitary Plan wind tunnel which is a variable-pressure, continuous-flow tunnel. The test section is approximately 4 feet square and 7 feet long. The nozzle leading to the test section is of the asymmetric sliding-block type which permits a continuous variation in test-section Mach number from about 1.5 to 2.9.

Models

The models tested were selected to form parametric variations in nose bluntness, fineness ratio, cone angle, and model base. Each model was designated by a four-digit number which is explained in the following table:

Digit	Relation to model	Number code
1	Nose bluntness, K, percent of flat-face diameter	1 = 0 percent (spherical) 2 = 50 percent 3 = 75 percent
2	Fineness ratio, λ	1 = 1/2 2 = 3/4 3 = 1
3	Cone half-angle, θ , deg	1 = 10° 2 = 15° 3 = 20°
4	Model base	1 = flat 2 = convex 3 = concave

For example, model 2213 has a nose bluntness of 50 percent of flat-face diameter, a fineness ratio of 3/4, a cone half-angle of 10°, and a concave base.

A general drawing of the models tested is presented in figure 2 and photographs of several models showing the various sting mountings are shown in figure 3. The model design dimensions were determined from the solution of the following equations after fixing a value of $d = 8.000$ inches.

$$\left(\frac{a}{d}\right) = 1 - 2\lambda \tan \theta \quad (1)$$

$$\left(\frac{r}{d}\right) = \left\{ \frac{1}{2} \cos \theta \left[1 - K\left(\frac{a}{d}\right) \right] - \lambda \sin \theta \right\} \left(\frac{1}{1 - \sin \theta} \right) \quad (2)$$

$$\left(\frac{A}{d}\right) = \left(\frac{r}{d}\right)(1 - \sin \theta) \quad (3)$$

$$\left(\frac{B}{d}\right) = \left(\frac{r}{d}\right) \cos \theta + \frac{1}{2} K\left(\frac{a}{d}\right) \quad (4)$$

These equations were derived from the geometry of the models by using the notation shown in figure 2(b). Solutions of these equations yield the following ratios: (Note: the last digit of the model number represents the model base and does not affect the equations.)

Model number	K, percent	λ	θ , deg	a/d	r/d	A/d	B/d
111x	0 (spherical) ↓	1/2	10	0.8237	0.4908	0.4056	0.4834
112x		1/2	15	.7321	.4770	.3536	.4608
113x		1/2	20	.6360	.4542	.2988	.4268
121x	0 (spherical) ↓	3/4	10	0.7355	0.4383	0.3622	0.4316
122x		3/4	15	.5981	.3897	.2888	.3764
123x		3/4	20	.4540	.3242	.2133	.3047
131x	0 (spherical) ↓	1	10	0.6473	0.3857	0.3188	0.3799
132x		1	15	.4641	.3024	.2241	.2921
133x		1	20	.2721	.1943	.1278	.1826
212x	50	1/2	15	0.7321	0.2385	0.1768	0.4134
221x	50 ↓	3/4	10	0.7355	0.2191	0.1811	0.3997
222x		3/4	15	.5981	.1949	.1444	.3377
223x		3/4	20	.4540	.1621	.1067	.2658
232x	50	1	15	0.4641	0.1512	0.1121	0.2621
312x	75	1/2	15	0.7321	0.1193	0.0884	0.3897
321x	75 ↓	3/4	10	0.7355	0.1096	0.0905	0.3837
322x		3/4	15	.5981	.0974	.0722	.3184
323x		3/4	20	.4540	.0811	.0533	.2464
332x	75	1	15	0.4641	0.0756	0.0560	0.2471

In addition to these quantities which describe the forward portion of the models, three different model bases - flat, convex, and concave - were tested. The convex base was made by a spherical radius of 1.25 base diameters such that the entire base was convex and the concave base (which had the same spherical radius) was concave over only 90 percent of the model-base diameter, the model base had a 5-percent flat shoulder. The three model bases are shown in figure 2(a).

Test Conditions

Tests were performed at the following conditions:

M	T_t , °F	p_t , lb/sq in. abs.	R
1.57	125	4.60	1.24×10^6
1.80	125	4.96	1.24×10^6
2.16	125	5.77	1.24×10^6

These tests were actually run from $\alpha = 0^\circ$ to 90° and 180° to 270° ; however, the data herein are presented for $\alpha = 0^\circ$ to 90° and 90° to 180° . The dewpoint, measured at stagnation pressure, was maintained below -30° F for all tests in order to assure negligible condensation effects.

Measurements and Sting Mountings

Aerodynamic forces and moments were measured by means of a three-component, internal strain-gage balance housed within the model. The balance in turn was rigidly fastened to a sting support system. It should be noted that all tests were made with the sting mounted through the base and/or the nose of the models as shown in figures 3(a) and 3(b) except models 1323 and 2323 which were sting mounted only through the sides of the models as shown in figure 3(c). In addition, model 2223 was mounted with four sting positions.

Schlieren photographs of each of the models were taken at various model attitudes. Typical schlieren photographs of some of these models at $M = 2.16$ are presented in figure 4.

Corrections

Angles of attack have been corrected for both tunnel-flow angularities and deflection of the balance and sting due to aerodynamic load. No corrections have been made for balance chamber pressures.

Accuracy

Based upon calibrations and repeatability of data, it is estimated that the various measured quantities are accurate within the following limits:

C_A	±0.015
C_N	±0.015
C_m	±0.003
α	±0.10
M	±0.015

It should be noted that these accuracies do not take into account the sting effects.

PRESENTATION OF RESULTS

The figure content showing the results of the present report is as follows:

Effect of sting mounting position on aerodynamic characteristics in pitch of model 2223	5
Aerodynamic characteristics in pitch of models having a nose bluntness of 0-percent flat face (spherical)	6
Aerodynamic characteristics in pitch of models having a nose bluntness of 50-percent flat face	7
Aerodynamic characteristics in pitch of models having a nose bluntness of 75-percent flat face	8
Effect of nose bluntness on aerodynamic characteristics in pitch	9
Effect of fineness ratio on aerodynamic characteristics in pitch	10
Effect of cone angle on aerodynamic characteristics in pitch	11
Effect of model base on aerodynamic characteristics in pitch	12
Effect of longitudinal variation in moment reference center on stability characteristics in pitch near 180° for models 2121, 2322, and 1313 at $M = 2.16$	13

Figures 6 to 8 contain the basic results of this investigation. It should be noted that figures 9 to 12 were obtained from the faired curves of figures 6 to 8 to show directly the effects of variations in nose bluntness, fineness ratio, cone angle, and model base.

The following table shows the basic data available in this report:

Model	α , deg	Basic data in figure
1112	0 to 90	6(a)
1113	90 to 180	6(b)
1121	0 to 180	6(c)
1122	90 to 180	6(d)
1131	0 to 90	6(e)
1212	0 to 90	6(f)
1213	90 to 180	6(g)
1221	0 to 180	6(h)
1222	90 to 180	6(i)
1231	0 to 90	6(j)
1312	0 to 90	6(k)
1313	90 to 180	6(l)
1322	0 to 180	6(m)
1323	0 to 90	6(n)
1331	0 to 90	6(o)
2121	0 to 180	7(a)
2211	90 to 180	7(b)
2212	0 to 180	7(c)
2213	90 to 180	7(d)
2221	0 to 180	7(e)
2222	0 to 180	7(f)
2223	0 to 180	7(g)
2231	0 to 180	7(h)
2232	90 to 180	7(i)
2321	0 to 180	7(j)
2322	90 to 180	7(k)
2323	0 to 90	7(l)
3121	0 to 90	8(a)
3212	0 to 90	8(b)
3221	0 to 180	8(c)
3222	90 to 180	8(d)
3231	0 to 90	8(e)
3321	0 to 90	8(f)
3322	90 to 180	8(g)

DISCUSSION

Sting Effects

The effects of sting-mounting position on the aerodynamic characteristics of model 2223 (tested with four sting-mounting positions) are shown in figure 5. The results indicate that sting effects decrease with increase in Mach number. For example, at a Mach number of 1.57 there are significant differences in the coefficient values at angles of attack for which the various sting mounts overlap each other, while at $M = 1.80$ these differences are smaller, and at $M = 2.16$ the data are generally in agreement. This effect of Mach number on sting-mounting position corroborates unpublished data on similar blunt bodies in this Mach number range. Examination of the data leads to the assumption that correct coefficients are obtained when the sting is shielded from the airstream by the model, but caution should be taken in utilizing the results obtained for any sting-model combination at high angles of attack relative to the sting.

Effects of Model Geometry

The effects of the four geometric variables of this test series on the aerodynamic characteristics in pitch were similar, though not of the same magnitude, for the different families of blunt bodies. (A family is defined as a group of bodies in which three geometric parameters are held constant and the fourth parameter is varied.) Therefore in order to describe these effects more easily, the data for three arbitrarily chosen families of models are presented in each of the comparison plots of figures 9 to 12. The following discussions of the effects of the geometric variables will not include the effects of Mach number since the trends of the data due to geometric variations are the same regardless of Mach number of the tests.

Nose bluntness, K.— The effects of nose bluntness on the aerodynamic characteristics in pitch of blunt bodies are presented in figure 9. These data show that an increase in nose bluntness leads to a decrease in stability at angles of attack near 0° and that this decrease in stability is almost directly proportional to the percentage of bluntness of the nose. For all positive angles of attack up to about 160° , the C_m values are more negative for the model with the least nose bluntness ($K = 0$ percent) and at angles of attack above about 160° , the C_m curves converge and show little effect of nose bluntness.

Increasing nose bluntness also leads to a greater normal-force slope at the lower angles of attack, and here again the change in slope appears to be directly proportional to the percentage of nose bluntness. The blunter the nose, the greater the C_N value for all positive angles of attack up to about 160° with the exception of model 1221 at angles of attack between 140° and 160° . Model 1221 has greater C_N values than do models 2221 and 3221 at angles of attack from 140° to 160° , although the reason for this exception has not been determined. For angles of attack beyond about 160° , there is little or no effect of nose bluntness on C_N .

The effects of nose bluntness on the axial force are apparent only up to angles of attack of about 70° . For angles of attack from 0° up to about 20° , contrary to what might be expected, the blunter noses have the lower C_A values while for angles of attack from 20° to 70° , increasing nose bluntness leads to an increase in C_A .

Fineness ratio, λ .— The effects of fineness ratio on the aerodynamic characteristics in pitch of blunt bodies are presented in figure 10. It may be seen that at low angles of attack an increase in fineness ratio leads to a large reduction in stability. At angles of attack greater than about 90° , there appears to be little effect of fineness ratio on the pitching-moment characteristics of the models. It is interesting to note the $1/3$ body-length center-of-gravity position chosen for these tests provides a stable configuration near $\alpha = 0^\circ$ for the bodies with the two lower fineness ratios ($\lambda = 1/2$ and $3/4$), but the bodies with $\lambda = 1$ are unstable in this region.

Increases in fineness ratio, as expected, lead to an increase in $C_{N\alpha}$ near $\alpha = 0^\circ$ and to higher normal-force values throughout most of the angle-of-attack range of the tests. There is a small angle-of-attack range near $\alpha = 180^\circ$ where the normal-force values are coincident for the three fineness-ratio bodies; however, even this small range appears to diminish with increasing Mach number.

The effects of fineness ratio on C_A near $\alpha = 0^\circ$ are large where increasing fineness ratio leads to reductions in C_{A0} ; the change from $\lambda = 1/2$ to $3/4$ causes a larger reduction than does the change from $\lambda = 3/4$ to 1. The effects on C_A decrease with increases in angle of attack, and fineness ratio appears to have no effect on C_A at $\alpha \approx 70^\circ$. However, since sting effects are known to be present at high angles of attack relative to the sting, it is felt that this will occur nearer 90° and also nearer $C_A = 0$. For angles of attack from about 100° to 180° , an increase in fineness ratio appears again to cause reductions in C_A , if one takes into account the orientation of forces as shown in figure 1, i.e., reduction in magnitude or absolute value.

Cone angle, θ .— The effects of cone angle on the aerodynamic characteristics in pitch of blunt bodies are presented in figure 11. The data indicate that increases in cone angle lead to greater stability at angles of attack near 0° , and the pitching-moment coefficients for the higher cone-angle models are more negative throughout the positive angle-of-attack range up to $\alpha \approx 150^\circ$. From $\alpha = 150^\circ$ to 180° , there is little or no effect of cone angle on the pitch characteristics of any of the test configurations.

Increases in cone angle have little effect on the normal-force-curve slope through $\alpha = 0^\circ$; however, in general, increasing cone angle causes a decrease in C_N throughout the angle-of-attack range of the tests to $\alpha \approx 160^\circ$ and from here to $\alpha = 180^\circ$ the C_N values are essentially the same regardless of cone angle.

The effects of cone angle on C_A are generally small although increases in cone angle appear to reduce C_A throughout most of the angle-of-attack range of the tests.

Model base.— The effects of model base on the aerodynamic characteristics in pitch of blunt bodies are presented in figure 12, and, as would be expected, the effects are insignificant on the C_m , C_N , and C_A characteristics at angles of attack to 70° . At angles of attack from 90° to about 160° , the C_m values for the concave-base configurations are considerably more negative than those for the flat-base configurations, whereas the convex-base configurations at $\alpha = 90^\circ$ have considerably more positive C_m values than those for the flat base. For angles of attack above about 160° , the C_m values for the convex and concave bodies are the same. In general the convex-base configurations have the greatest C_N values and the least (smallest magnitude) C_A values at angles of attack from 90° to 180° while at these angles of attack the C_N as well as the C_A values for the flat- and concave-base configurations are essentially the same.

It should be noted in figure 12 that at $M = 1.80$ there are large changes in the C_A curves near $\alpha = 170^\circ$ for all models having flat or concave bases (this is true also of all models in figs. 5, 6, and 7). These large changes do not occur for any of the convex-base models tested although there are slight variations in C_A near $\alpha = 170^\circ$ for models 2212, 2322, and 3322 as seen in figures 7(c), 7(k), and 8(g), respectively. The reason for these changes is not readily apparent from schlieren photographs (not presented in present report) but they were repeatable and occurred for all the flat- and concave-base models at $M = 1.80$.

Stability near 180° (blunt base forward).— As may be seen in figures 5 to 12, all models tested were stable for angles of attack near 180° and, for these angles, the models exhibited zero or negative normal-force slopes. (It seems characteristic of very short, blunt bodies that they may have zero or negative normal-force slopes for subsonic and low supersonic speeds when the blunt face is forward, e.g., refs. 3, 4, 6, and 9.) Due to these zero or negative normal-force slopes, the configurations could not be made unstable near 180° by longitudinal shifts in the moment center. To illustrate, figure 13 shows the pitching-moment curves near $\alpha = 180^\circ$ for three of the test models at $M = 2.16$. It may be seen in figure 13 that while longitudinal shifts in the moment center toward the nose (i.e., $x/l = 2/3$ and 1) help to reduce and/or eliminate the stable trends for angles of attack below about 170° , there is still a small region of positive stability near 180° . Since this stable region cannot be remedied by the inherent aerodynamic characteristics of the models, it is felt that from a static stability standpoint all the bodies tested in the present investigation are unsuitable for passive entry vehicles if the vehicles enter in the nose-forward position since heat protection would be required over the entire surface of the body with a resultant weight penalty. (Refs. 3 and 10 state that successful entry is dependent mainly upon the inherent stability and/or structural integrity of the vehicle.) However, one obvious body change which could produce instability at 180° (blunt base forward) and provide

only one stable trim point at $\alpha = 0^\circ$, would be to add larger convex portions to the base in the form of cones, spherical cones or spherical segments which would increase $C_{N\alpha}$ and reduce $C_{m\alpha}$ for the base-forward condition (see, for example, refs. 4, 10, 11).

CONCLUSIONS

The results of tests at Mach numbers of 1.57, 1.80, and 2.16 of bodies which varied in nose bluntness, fineness ratio, cone half-angle, and model base indicate the following conclusions:

1. From a static stability standpoint, all of the models tested are unsuitable for use as a passive entry vehicle if the vehicle is to enter in the nose-forward condition, since the stable trim points near an angle of attack of 180° cannot be eliminated by their inherent aerodynamic characteristics.
2. Increases in nose bluntness or fineness ratio and decreases in cone half-angles lead to decreases in stability near angles of attack of 0° . The model base had no effect on the stability near angles of attack of 0° .
3. Increases in nose bluntness or fineness ratio and decreases in cone half-angles lead to increases in normal force for most of the angle-of-attack range of 180° . The model base had no effect on normal force up to about 90° and only slight effects from 90° to 180° where the convex-base models had the highest values of normal force.
4. Increases in nose bluntness, fineness ratio, or cone half-angles generally lead to decreases in axial force for angles of attack near 0° . The effects of model base are apparent only for angles of attack from 90° to 180° and, at 180° , the concave-base models had the most negative axial force while the convex-base models had the least negative axial force.

Langley Research Center,
National Aeronautics and Space Administration,
Langley Station, Hampton, Va., February 7, 1963.

REFERENCES

1. Wehrend, William R., Jr.: Wind-Tunnel Investigation of the Static and Dynamic Stability Characteristics of a 10° Semivertex Angle Blunted Cone. NASA TN D-1202, 1962.
2. Intrieri, Peter F.: Free-Flight Measurements of the Static and Dynamic Stability and Drag of a 10° Blunted Cone at Mach Numbers 3.5 and 8.5. NASA TN D-1299, 1962.
3. Peterson, Victor L.: Motions of a Short 10° Blunted Cone Entering a Martian Atmosphere at Arbitrary Angles of Attack and Arbitrary Pitching Rates. NASA TN D-1326, 1962.
4. Treon, Stuart L.: Static Aerodynamic Characteristics of Short Blunt Cones With Various Nose and Base Cone Angles at Mach Numbers From 0.6 to 5.5 and Angles of Attack to 180° . NASA TN D-1327, 1962.
5. Wehrend, William R., Jr., and Reese, David E., Jr.: Wind-Tunnel Tests of the Static and Dynamic Stability Characteristics of Four Ballistic Re-Entry Bodies. NASA TM X-369, 1960.
6. Fisher, Lewis R., Keith, Arvid L., Jr., and DiCamillo, Joseph R.: Aerodynamic Characteristics of Some Families of Blunt Bodies at Transonic Speeds. NASA MEMO 10-28-58L, 1958.
7. McDearmon, Russell W., and Lawson, Warren A.: Investigation of the Normal-Force, Axial-Force, and Pitching-Moment Characteristics of Blunt Low-Fineness-Ratio Bodies of Revolution at a Mach Number of 3.55. NASA TM X-467, 1961.
8. Letko, William: Experimental Investigation at a Mach Number of 3.11 of the Lift, Drag, and Pitching-Moment Characteristics of a Number of Blunt Low-Fineness-Ratio Bodies. NASA MEMO 1-18-59L, 1959.
9. Pearson, Albin O.: Wind-Tunnel Investigation at Mach Numbers From 0.50 to 1.14 of the Static Aerodynamic Characteristics of a Model of a Project Mercury Capsule. NASA TM X-292, 1960.
10. Faget, Maxime A., Garland, Benjamine J., and Buglia, James J.: Preliminary Studies of Manned Satellites. Wingless Configuration: Nonlifting. NASA TN D-1254, 1962. (Supersedes NACA RM L58E07a.)
11. Shaw, David S., and Turner, Kenneth L.: Wind-Tunnel Investigation of Static Aerodynamic Characteristics of a 1/9-Scale Model of a Possible Reentry Capsule at Mach Numbers From 2.29 to 4.65. NASA TM X-233, 1959.
12. Harman, Richard W., and Boatright, William B.: Investigation of the Aerodynamic Characteristics of a Reentry Capsule With Various Nose Shapes at a Mach Number of 2.91, Including Studies of Nose Spikes as a Means of Control. NASA TM X-426, 1961.

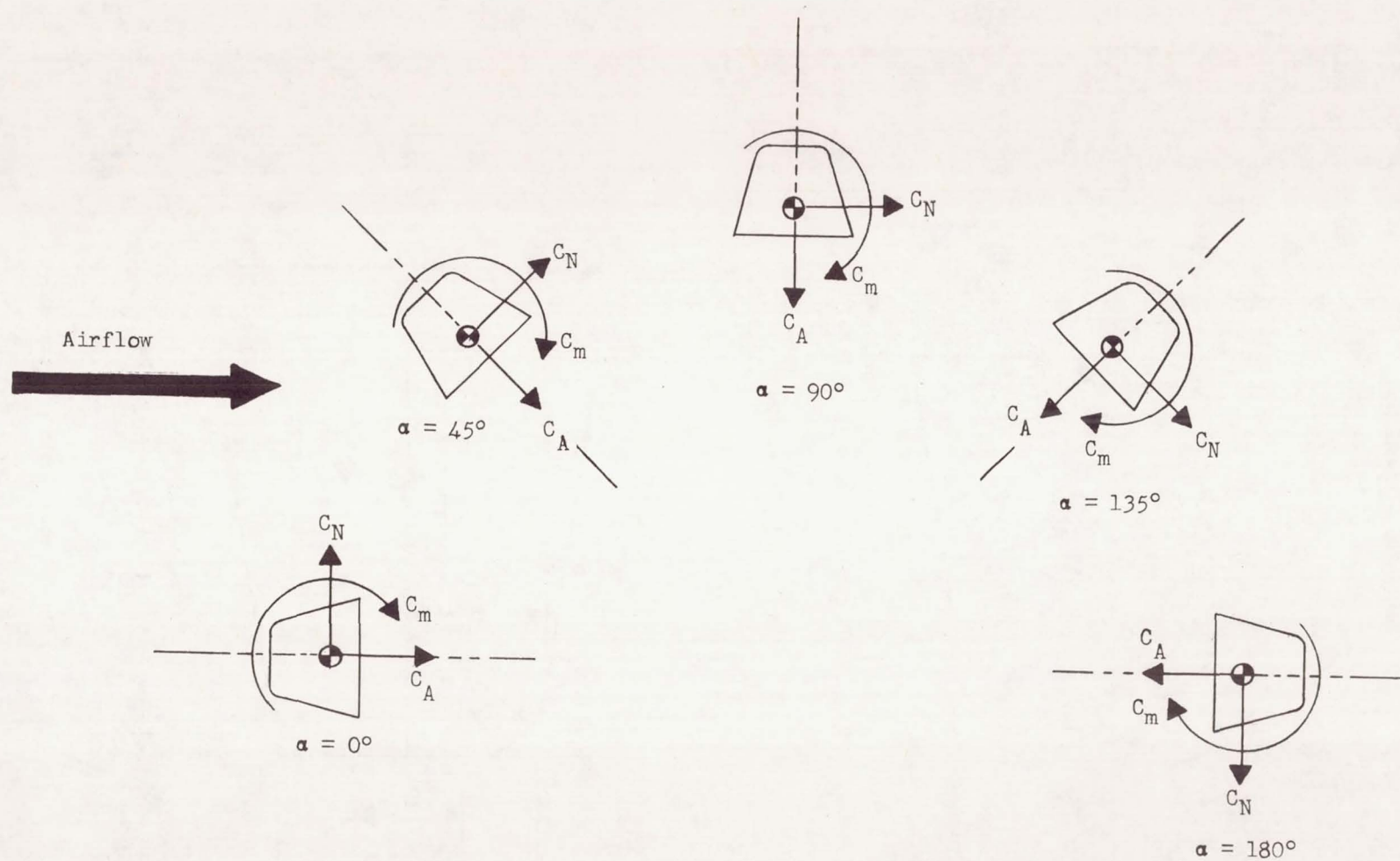
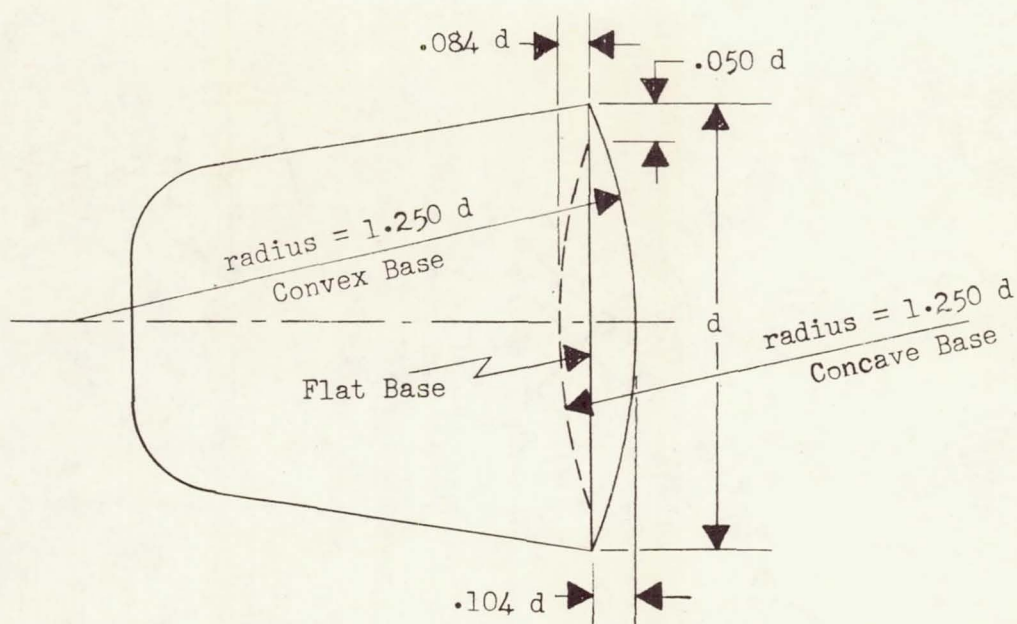
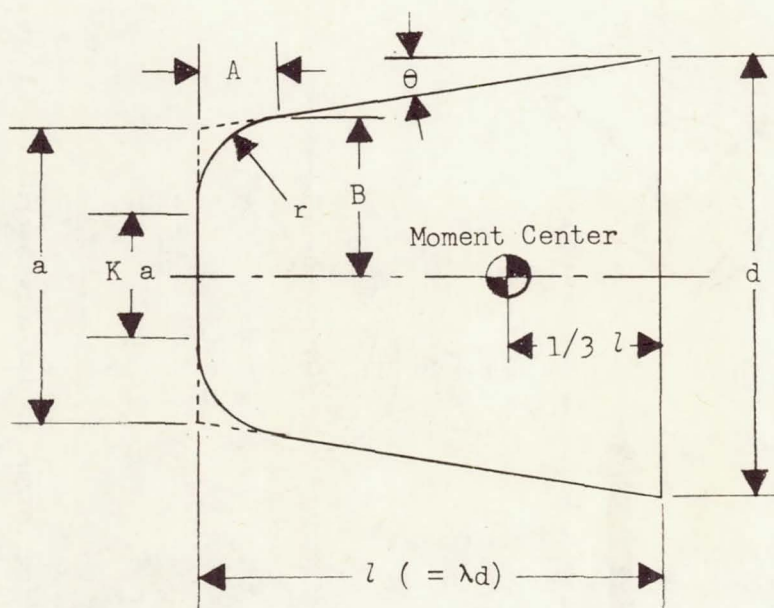


Figure 1.- Body-axis system and model orientation. (Arrows indicate positive directions.)

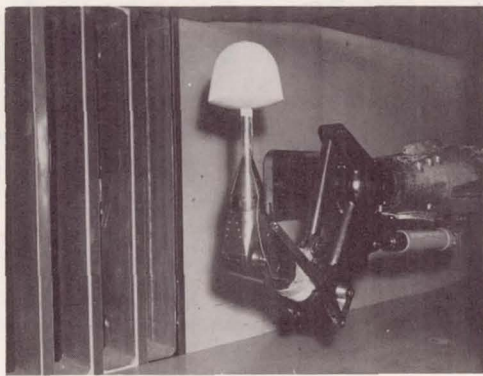


(a) Model bases.

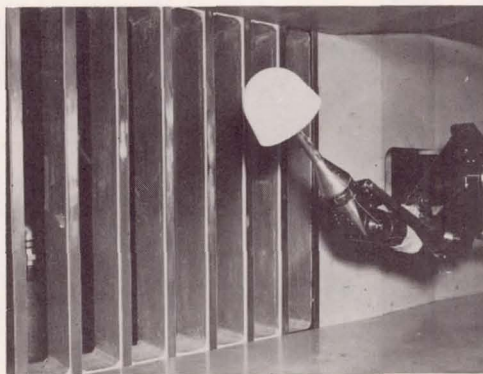


(b) Typical model (with flat base shown).

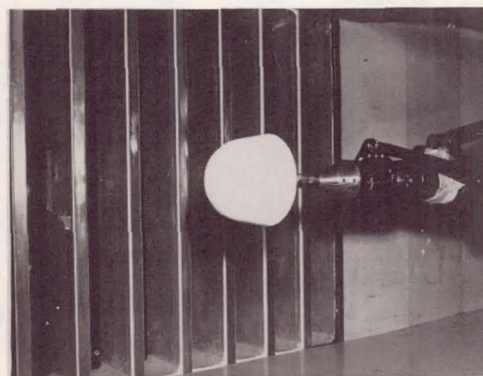
Figure 2.- Model drawings.



$\alpha \approx 90^\circ$



$\alpha \approx 45^\circ$



$\alpha = 0^\circ$

(a) Model 1312 sting mounted through base. $\alpha \approx 0^\circ$ to 90° .

L-63-32

Figure 3.- Model photographs showing various sting-mounting positions.



$\alpha = 180^\circ$



$\alpha = 135^\circ$

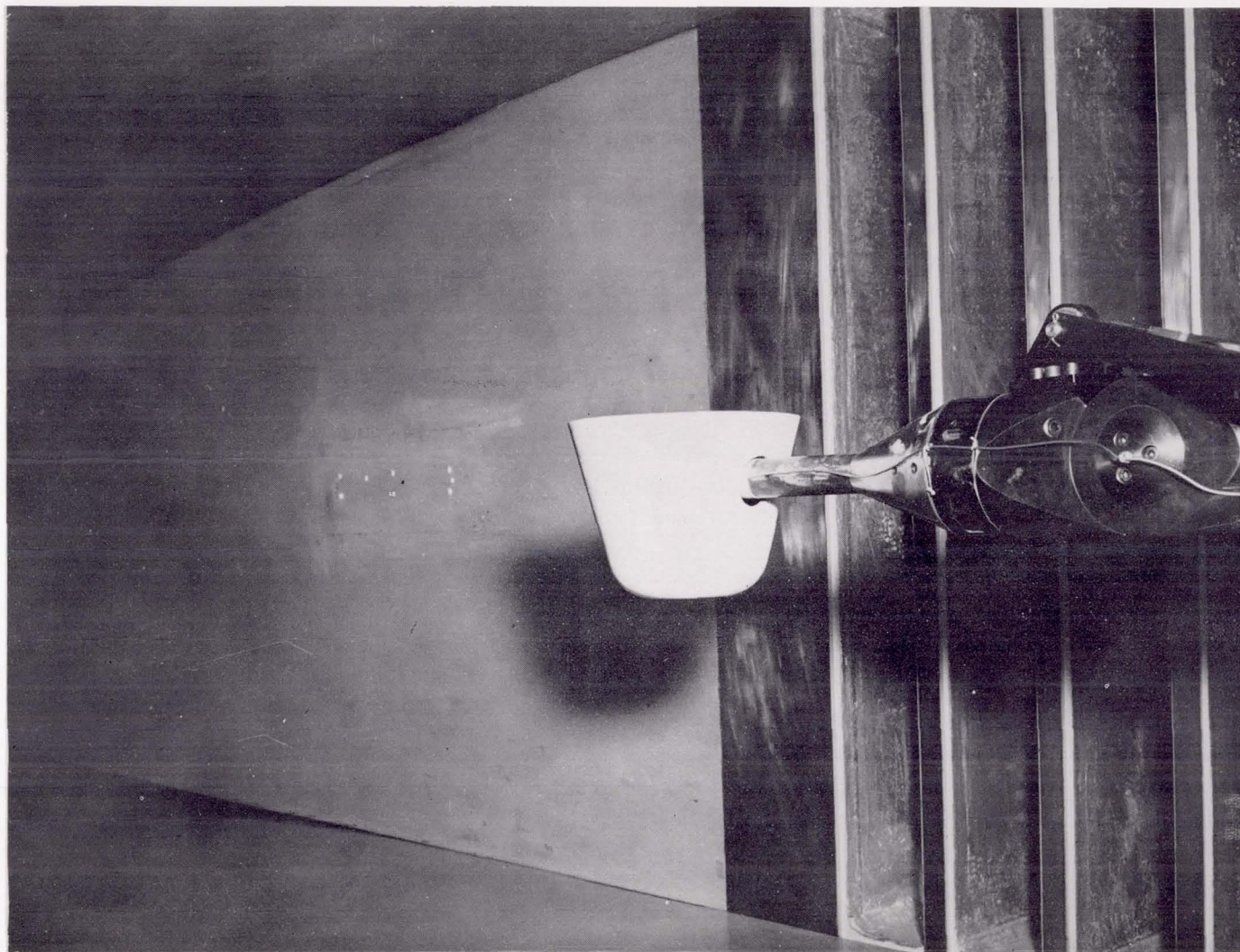


$\alpha = 90^\circ$

(b) Model 2322 sting mounted through nose. $\alpha = 90^\circ$ to 180° .

I-63-33

Figure 3.- Continued.

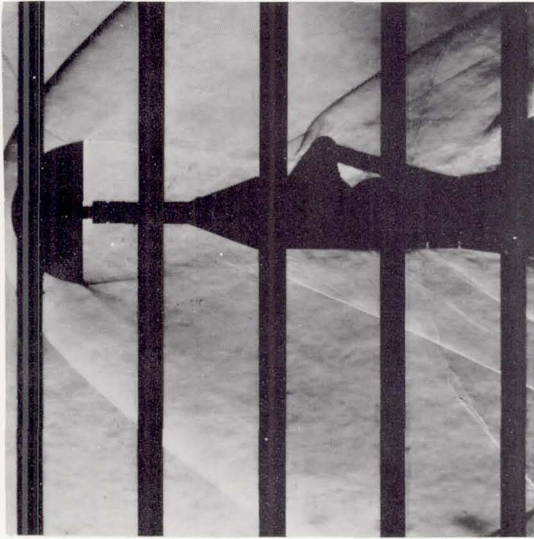


$\alpha = 90^\circ$

(c) Model 2223 sting mounted through side.

L-61-7820

Figure 3.- Concluded.



$\alpha = 1.4^\circ$



$\alpha = 51.5^\circ$



$\alpha = 71.6^\circ$

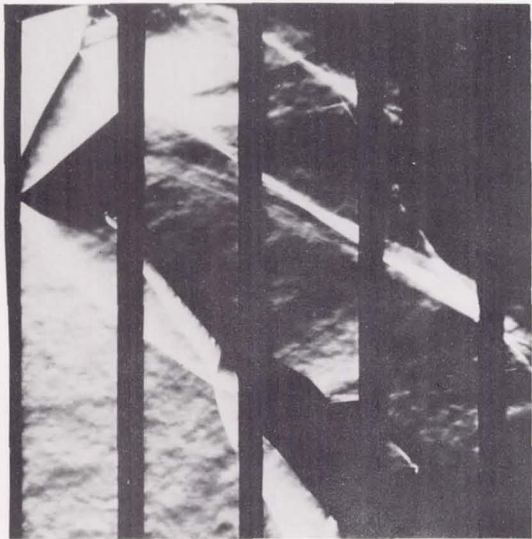


$\alpha = 86.6^\circ$

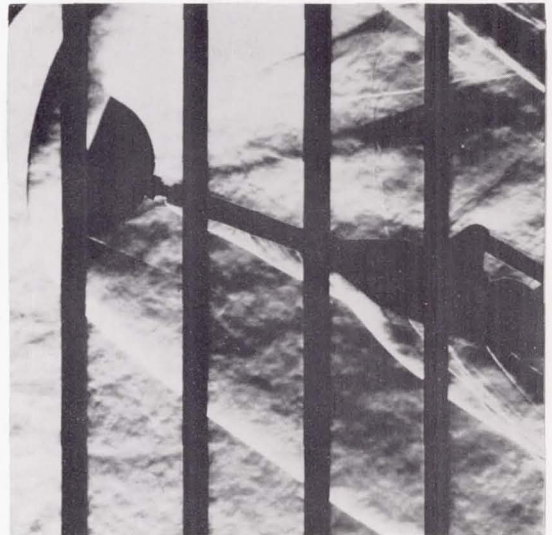
(a) Model 1121.

I-63-34

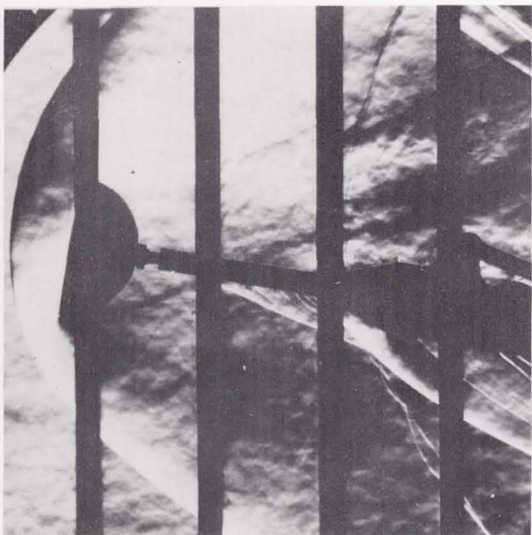
Figure 4.- Schlieren photographs of several models at $M = 2.16$.



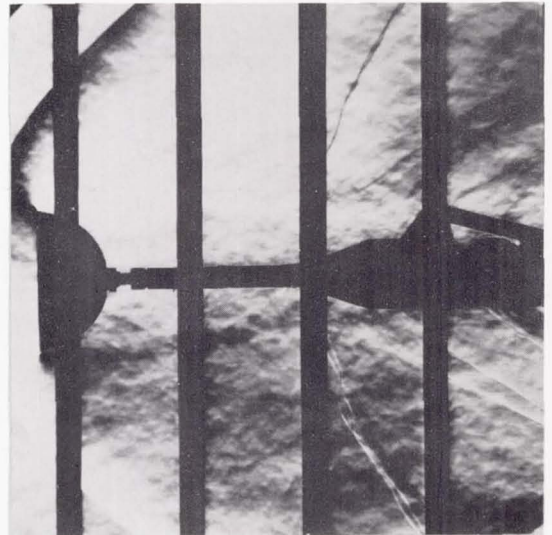
$\alpha = 129.2^\circ$



$\alpha = 159.3^\circ$



$\alpha = 169.5^\circ$

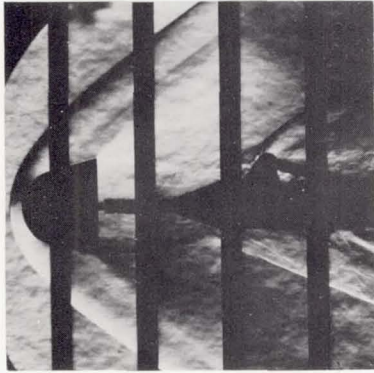


$\alpha = 179.5^\circ$

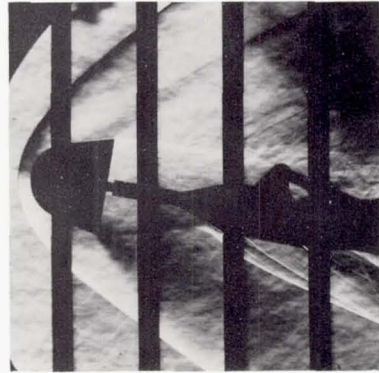
(a) Concluded.

L-63-35

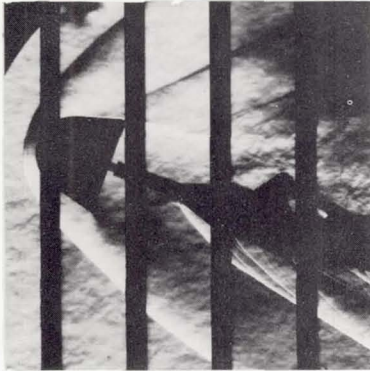
Figure 4.- Continued.



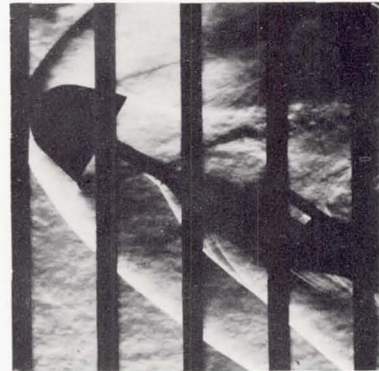
$\alpha = 1.5^\circ$



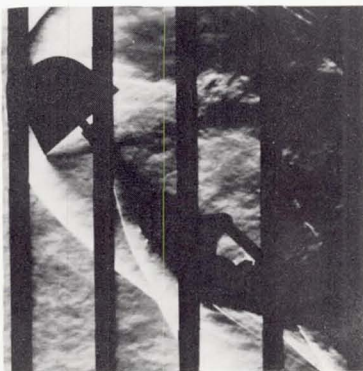
$\alpha = 11.6^\circ$



$\alpha = 21.7^\circ$



$\alpha = 31.7^\circ$

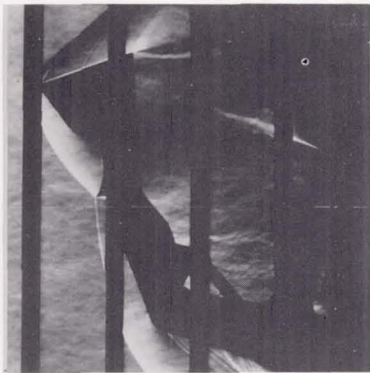


$\alpha = 51.7^\circ$

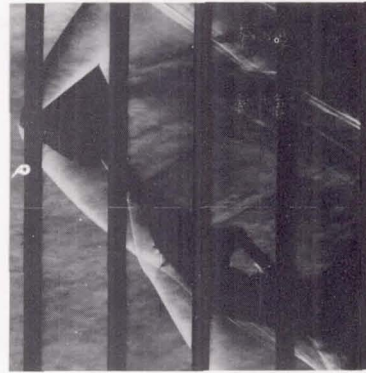
(b) Model 1221.

L-63-36

Figure 4.- Continued.



$\alpha = 109.0^\circ$



$\alpha = 129.2^\circ$



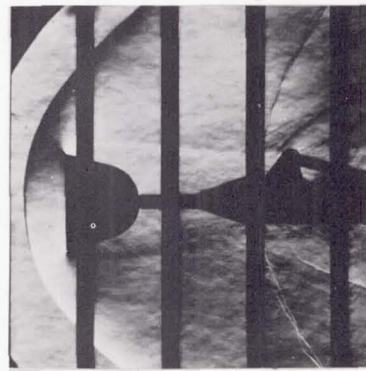
$\alpha = 149.2^\circ$



$\alpha = 159.2^\circ$



$\alpha = 169.3^\circ$

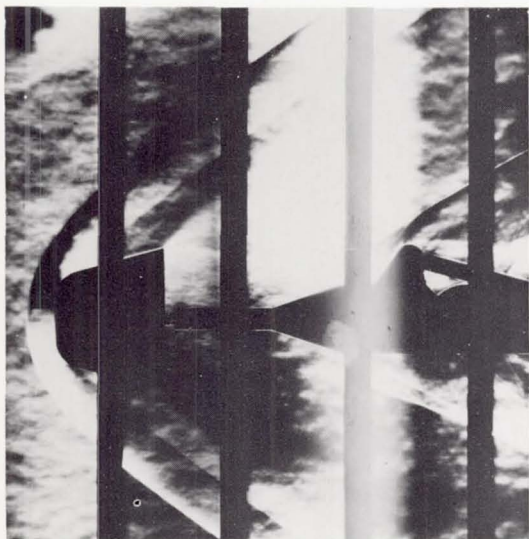


$\alpha = 179.4^\circ$

(b) Concluded.

L-63-37

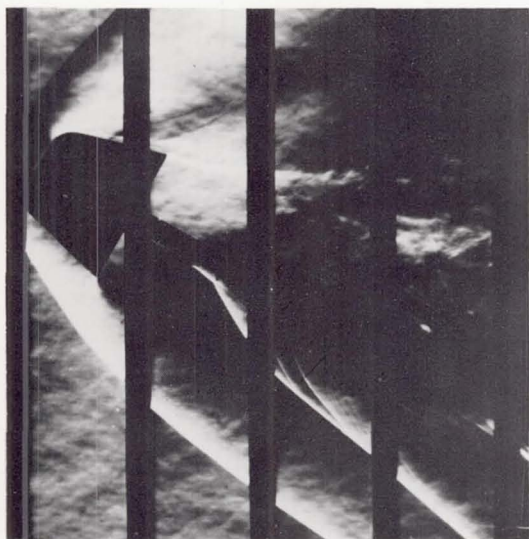
Figure 4.- Continued.



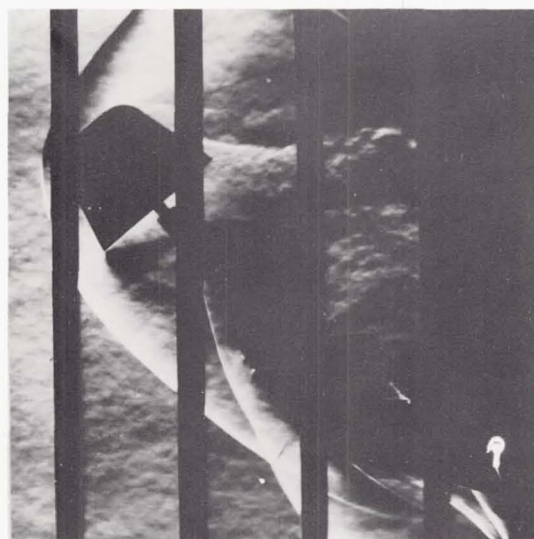
$\alpha = 1.5^\circ$



$\alpha = 21.7^\circ$



$\alpha = 31.7^\circ$

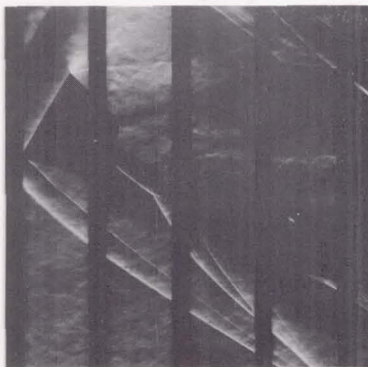


$\alpha = 51.8^\circ$

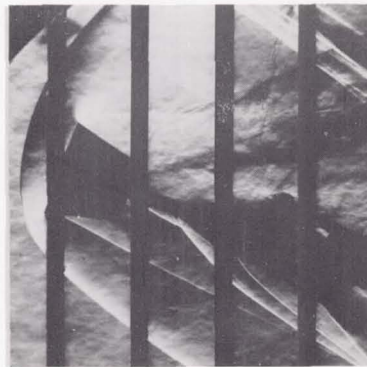
(c) Model 2221.

L-63-38

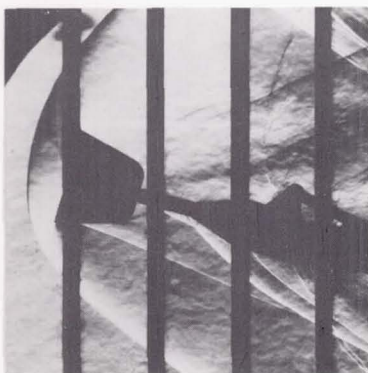
Figure 4.- Continued.



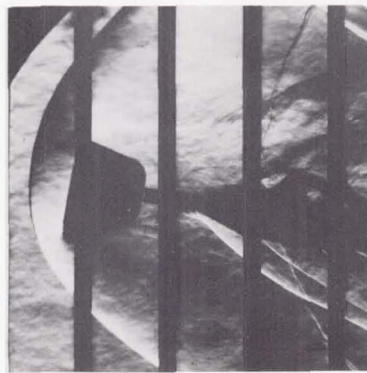
$\alpha = 149.3^\circ$



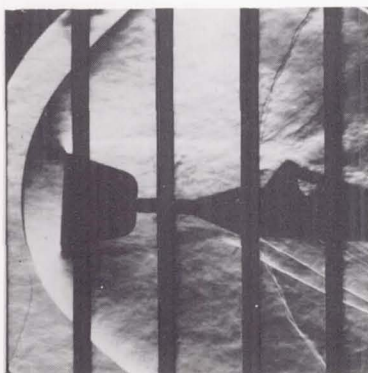
$\alpha = 159.2^\circ$



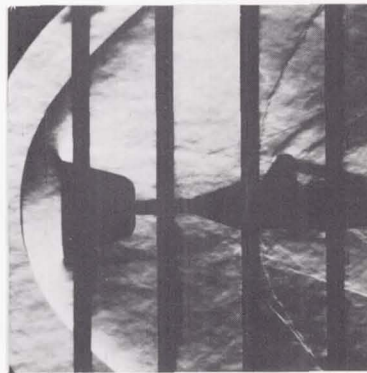
$\alpha = 163.2^\circ$



$\alpha = 169.4^\circ$



$\alpha = 175.5^\circ$

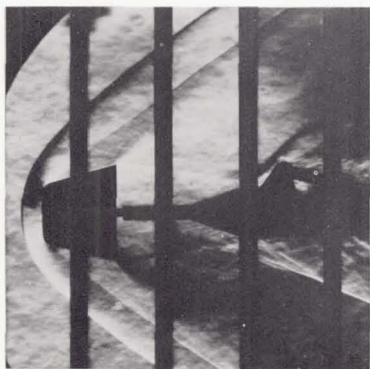


$\alpha = 179.4^\circ$

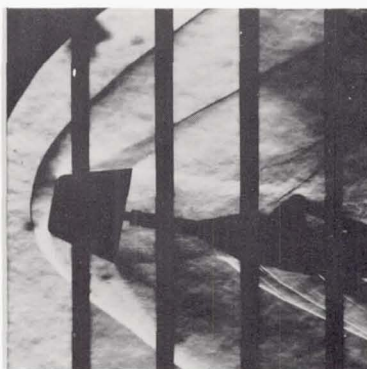
(c) Concluded.

L-63-39

Figure 4.- Continued.



$\alpha = 1.5^\circ$



$\alpha = 11.6^\circ$



$\alpha = 17.7^\circ$



$\alpha = 21.7^\circ$



$\alpha = 31.7^\circ$



$\alpha = 51.8^\circ$

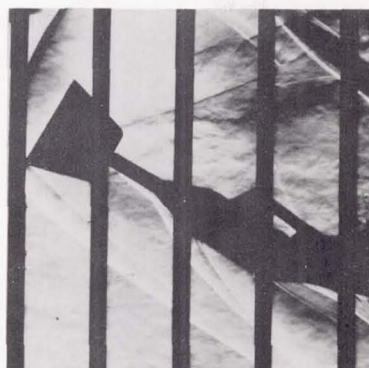
(d) Model 3221.

L-63-40

Figure 4.- Continued.



$\alpha = 129.1^\circ$



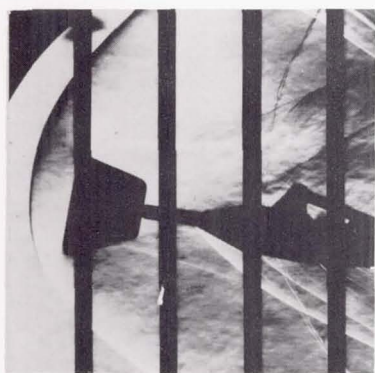
$\alpha = 149.2^\circ$



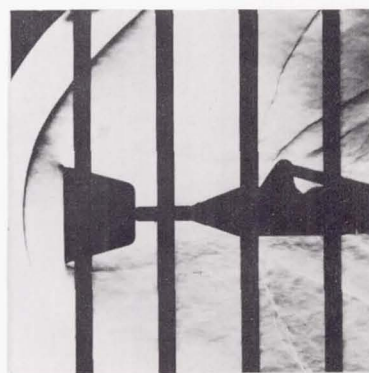
$\alpha = 159.2^\circ$



$\alpha = 163.2^\circ$



$\alpha = 169.3^\circ$

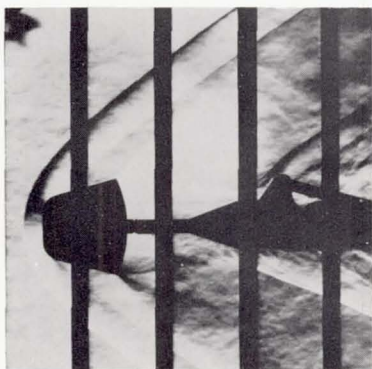


$\alpha = 179.4^\circ$

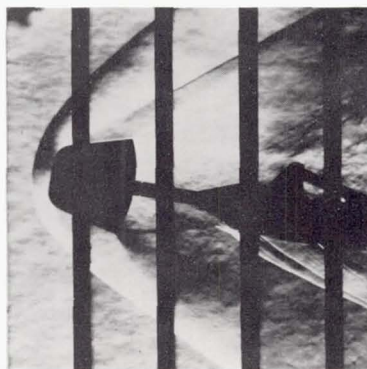
(d) Concluded.

L-63-41

Figure 4.- Continued.



$\alpha = 1.5^\circ$



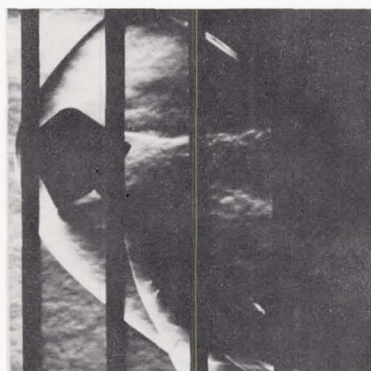
$\alpha = 11.6^\circ$



$\alpha = 21.7^\circ$



$\alpha = 31.7^\circ$

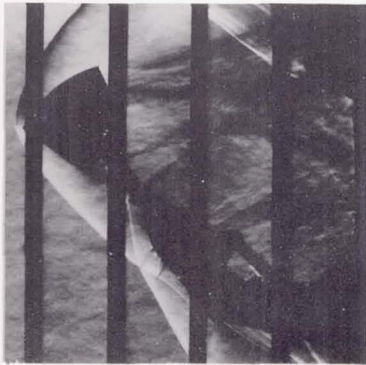


$\alpha = 51.8^\circ$

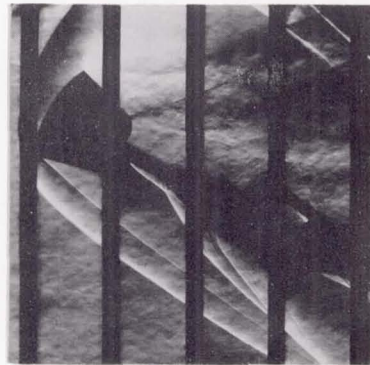
(e) Model 2222.

L-63-42

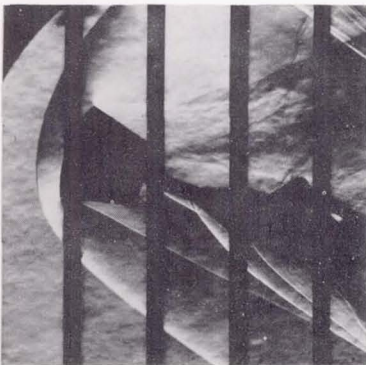
Figure 4.- Continued.



$$\alpha = 129.1^{\circ}$$



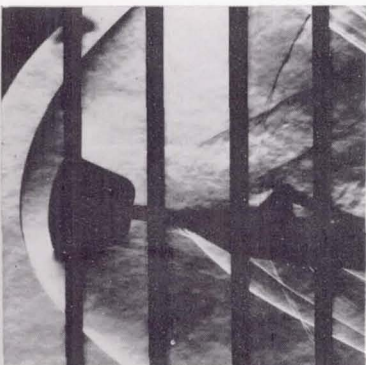
$$\alpha = 149.2^{\circ}$$



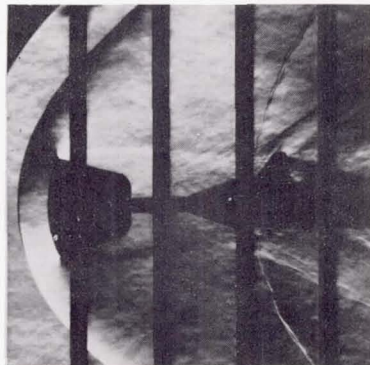
$$\alpha = 159.2^{\circ}$$



$$\alpha = 163.2^{\circ}$$



$$\alpha = 169.3^{\circ}$$

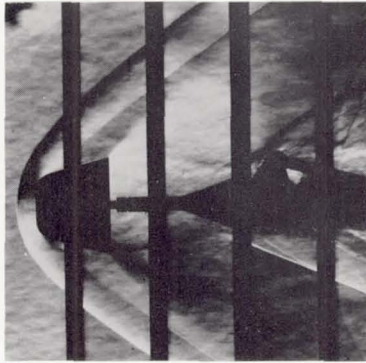


$$\alpha = 179.4^{\circ}$$

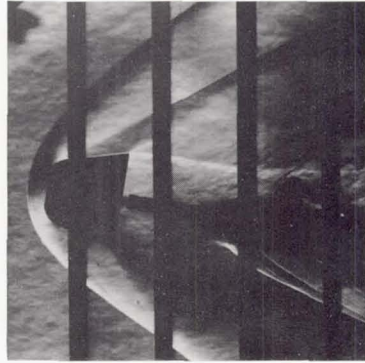
(e) Concluded.

L-63-43

Figure 4.- Continued.



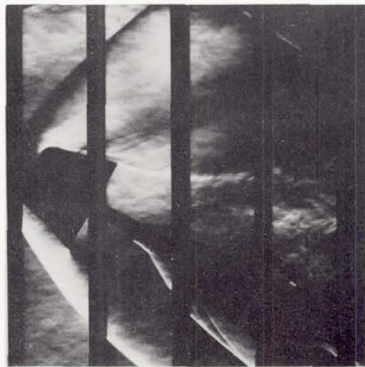
$\alpha = 1.5^\circ$



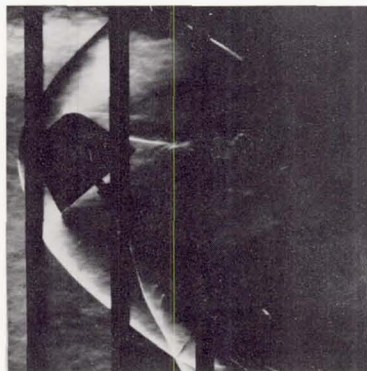
$\alpha = 11.6^\circ$



$\alpha = 21.7^\circ$



$\alpha = 31.7^\circ$

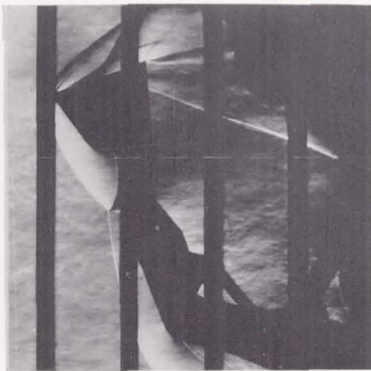


$\alpha = 51.8^\circ$

(f) Model 2223.

L-63-44

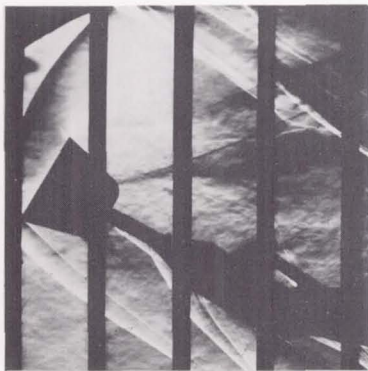
Figure 4.- Continued.



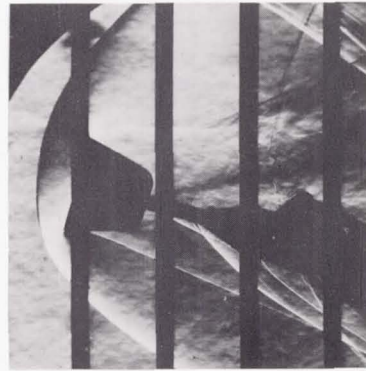
$$\alpha = 108.8^{\circ}$$



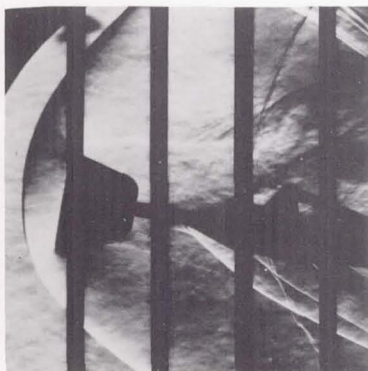
$$\alpha = 129.1^{\circ}$$



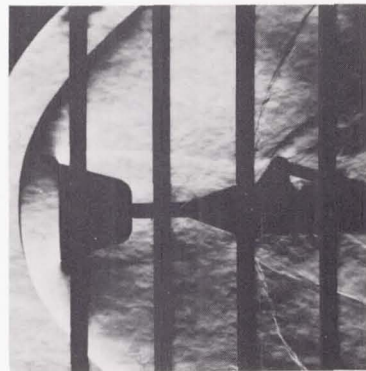
$$\alpha = 149.2^{\circ}$$



$$\alpha = 163.2^{\circ}$$



$$\alpha = 169.3^{\circ}$$



$$\alpha = 179.4^{\circ}$$

(f) Concluded.

L-63-45

Figure 4.- Concluded.

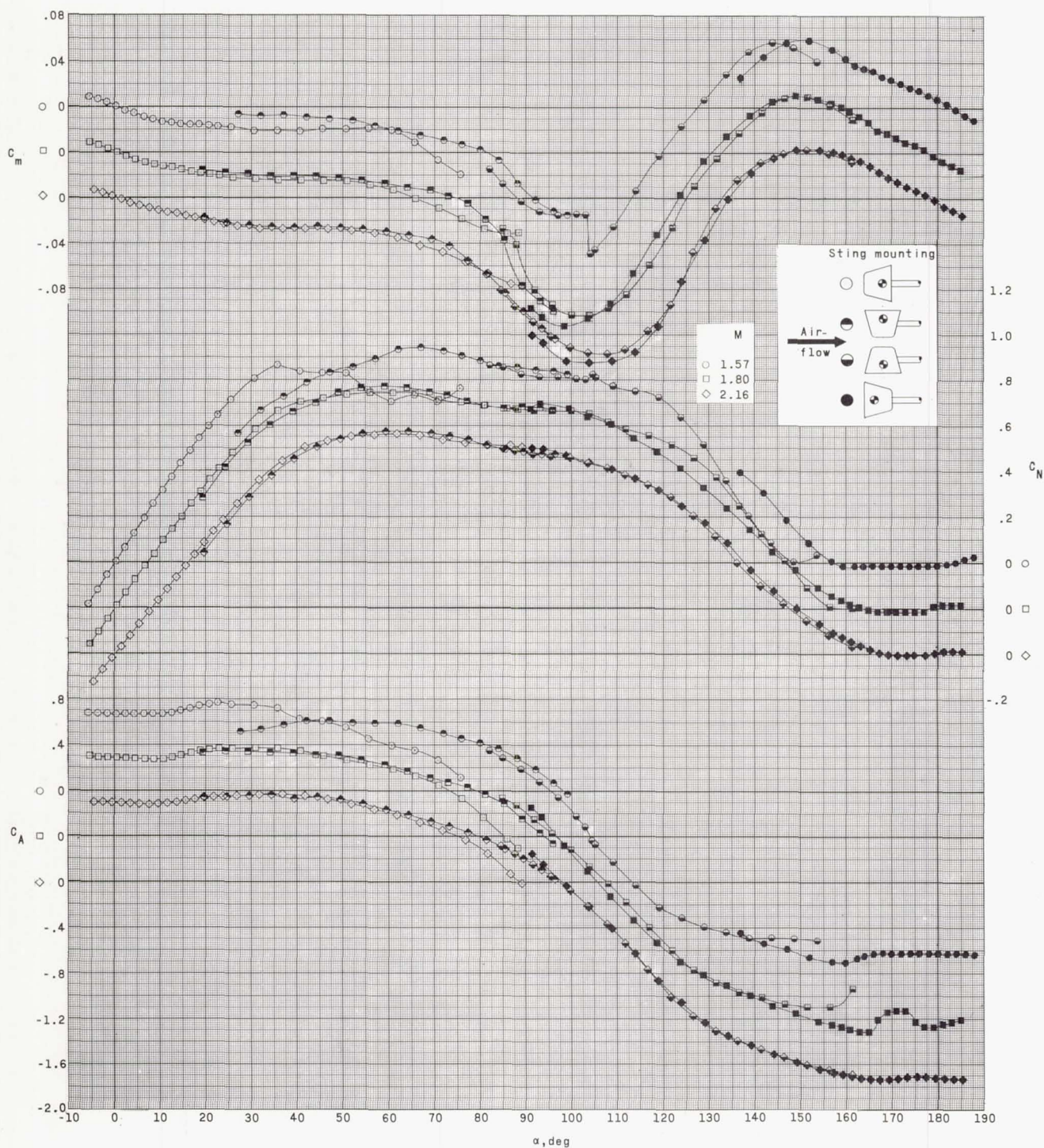
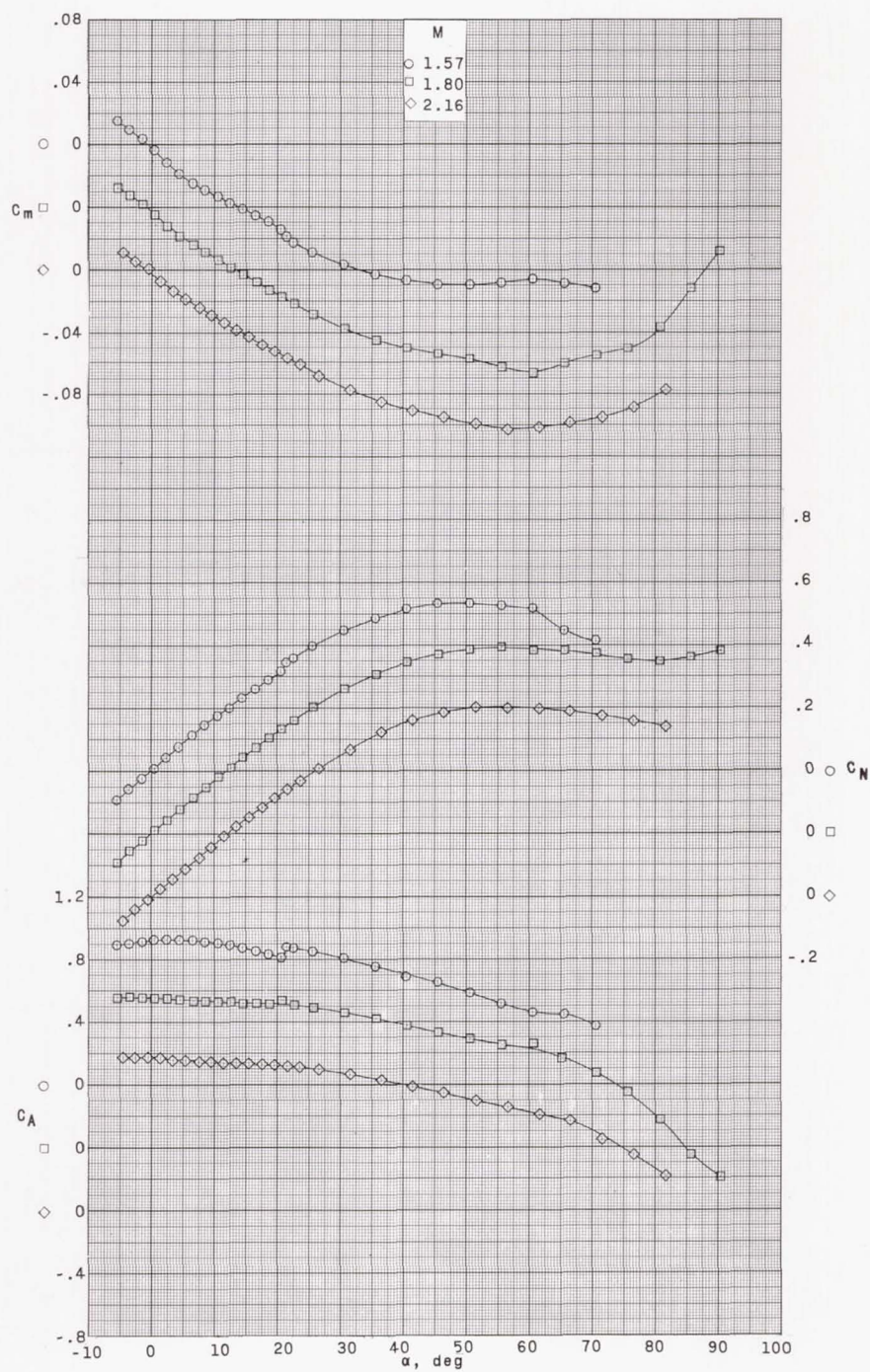
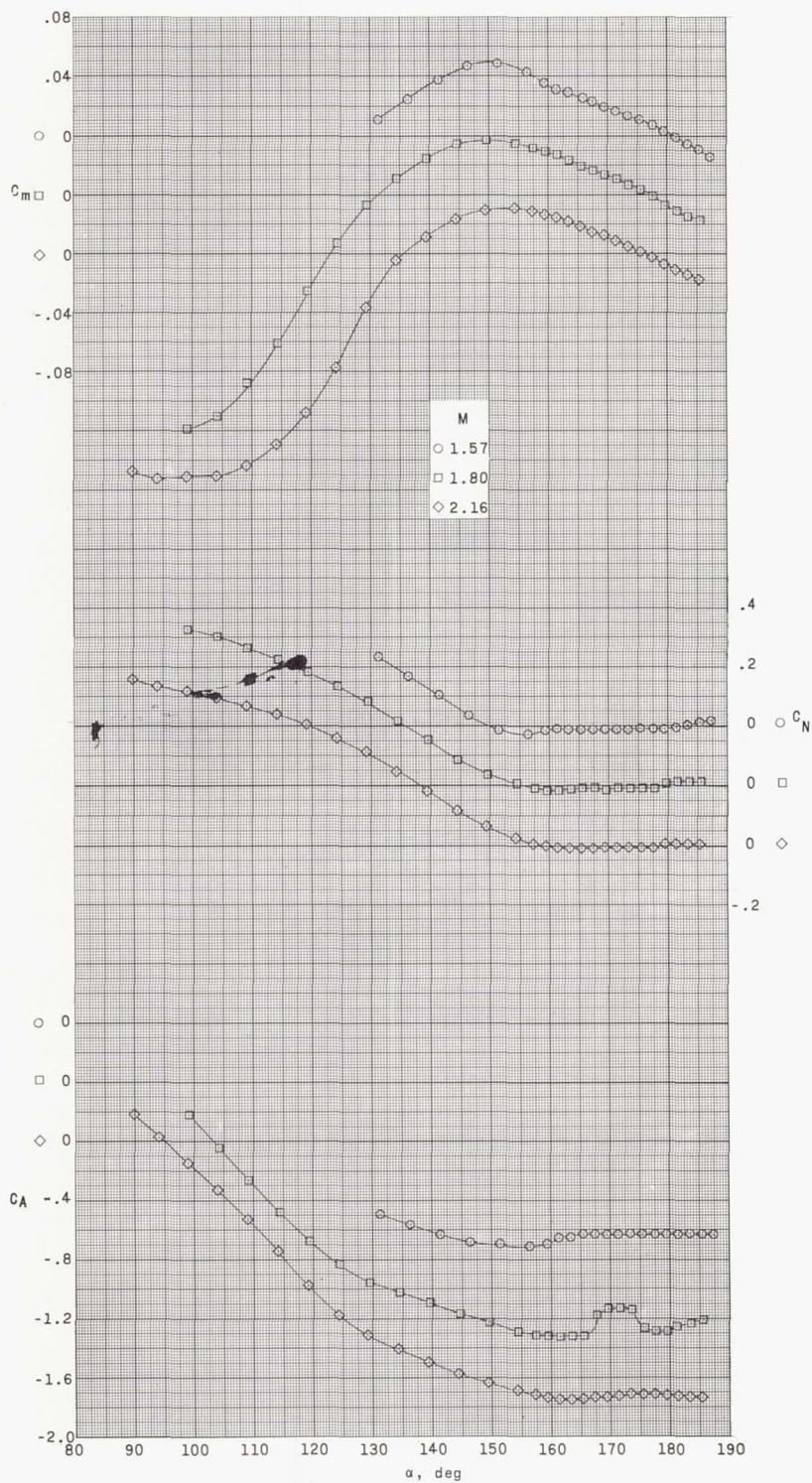


Figure 5.- Effect of sting-mounting position on aerodynamic characteristics in pitch of model 2223.
 $K = 50$ percent; $\lambda = 3/4$; $\theta = 15^\circ$; base, concave.



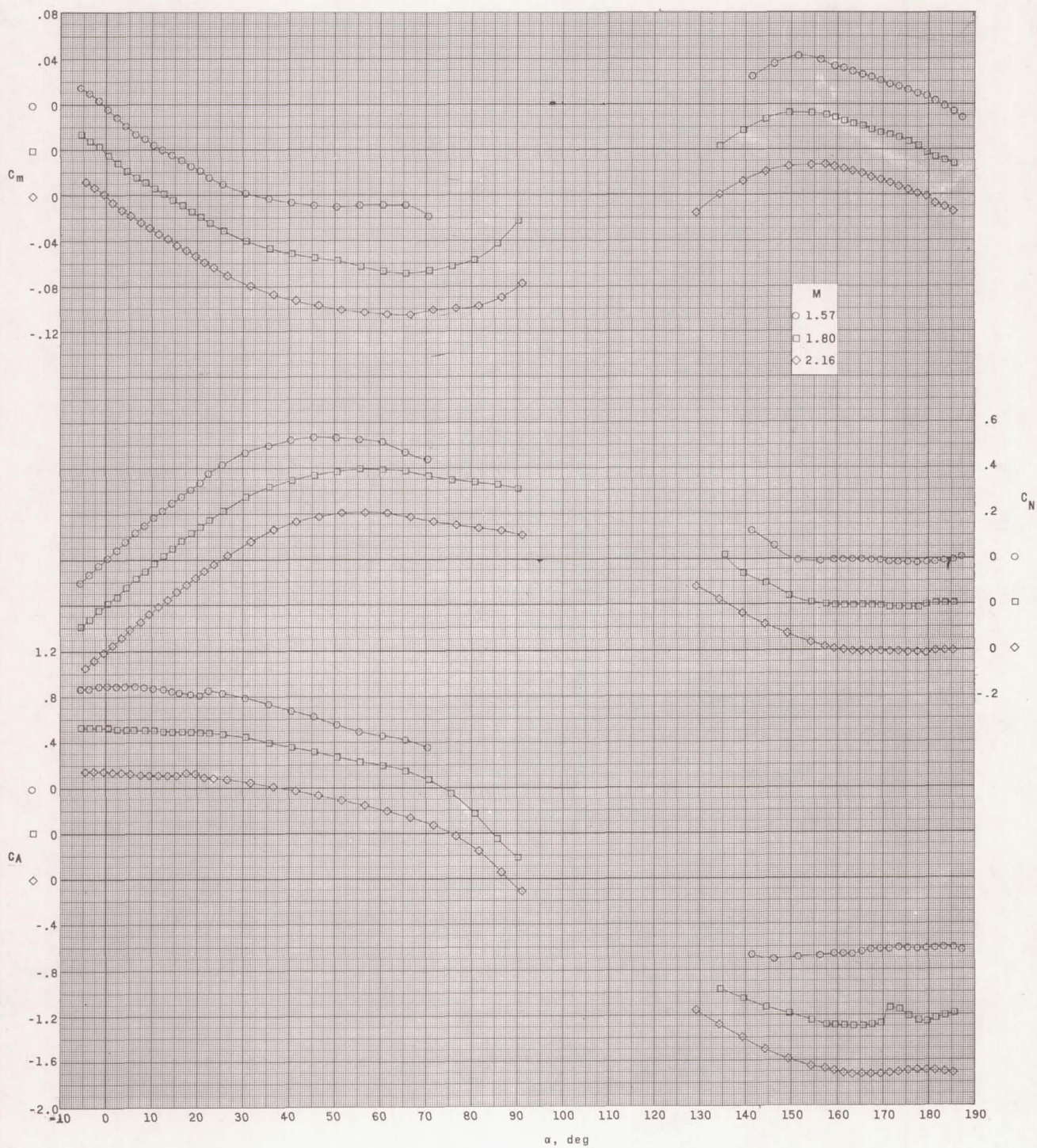
(a) Model 1112; $K = 0$ percent; $\lambda = 1/2$; $\theta = 10^\circ$; base, convex.

Figure 6.- Aerodynamic characteristics in pitch of models having a nose bluntness of 0-percent flat face (spherical).



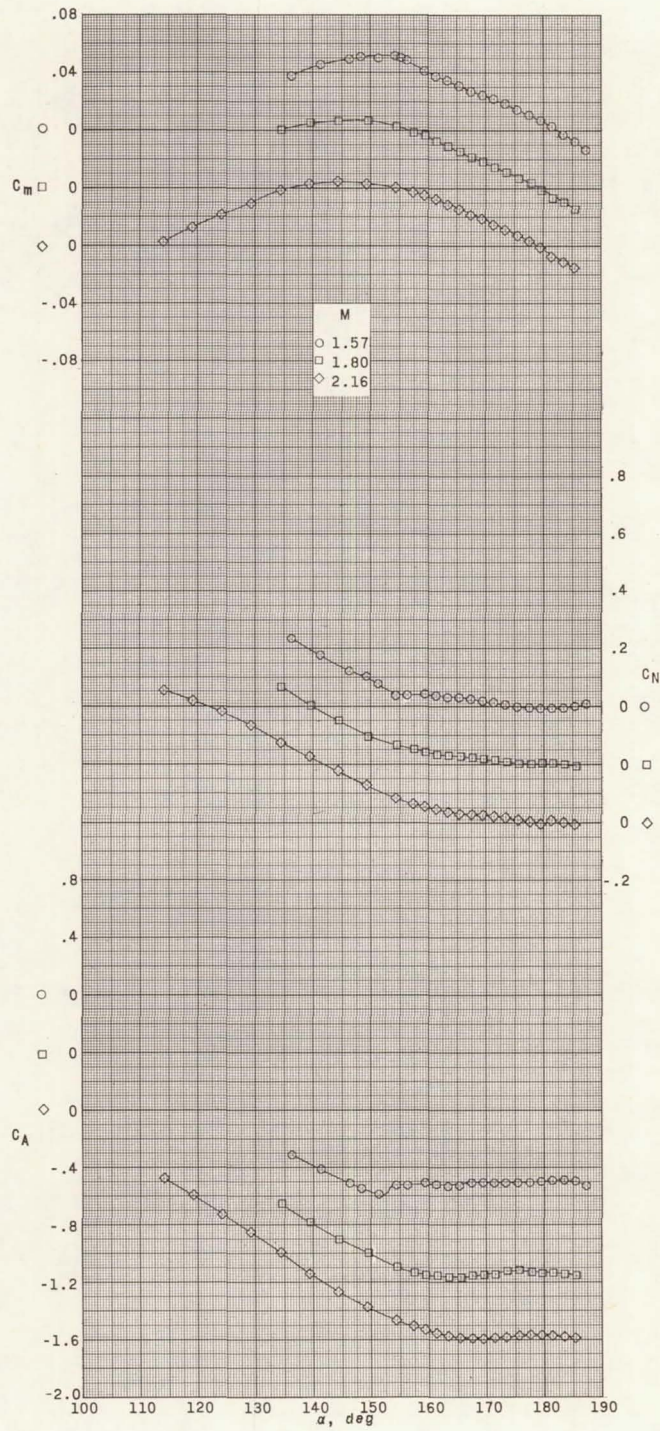
(b) Model 1113; $K = 0$ percent; $\lambda = 1/2$; $\theta = 10^\circ$; base, concave.

Figure 6.- Continued.



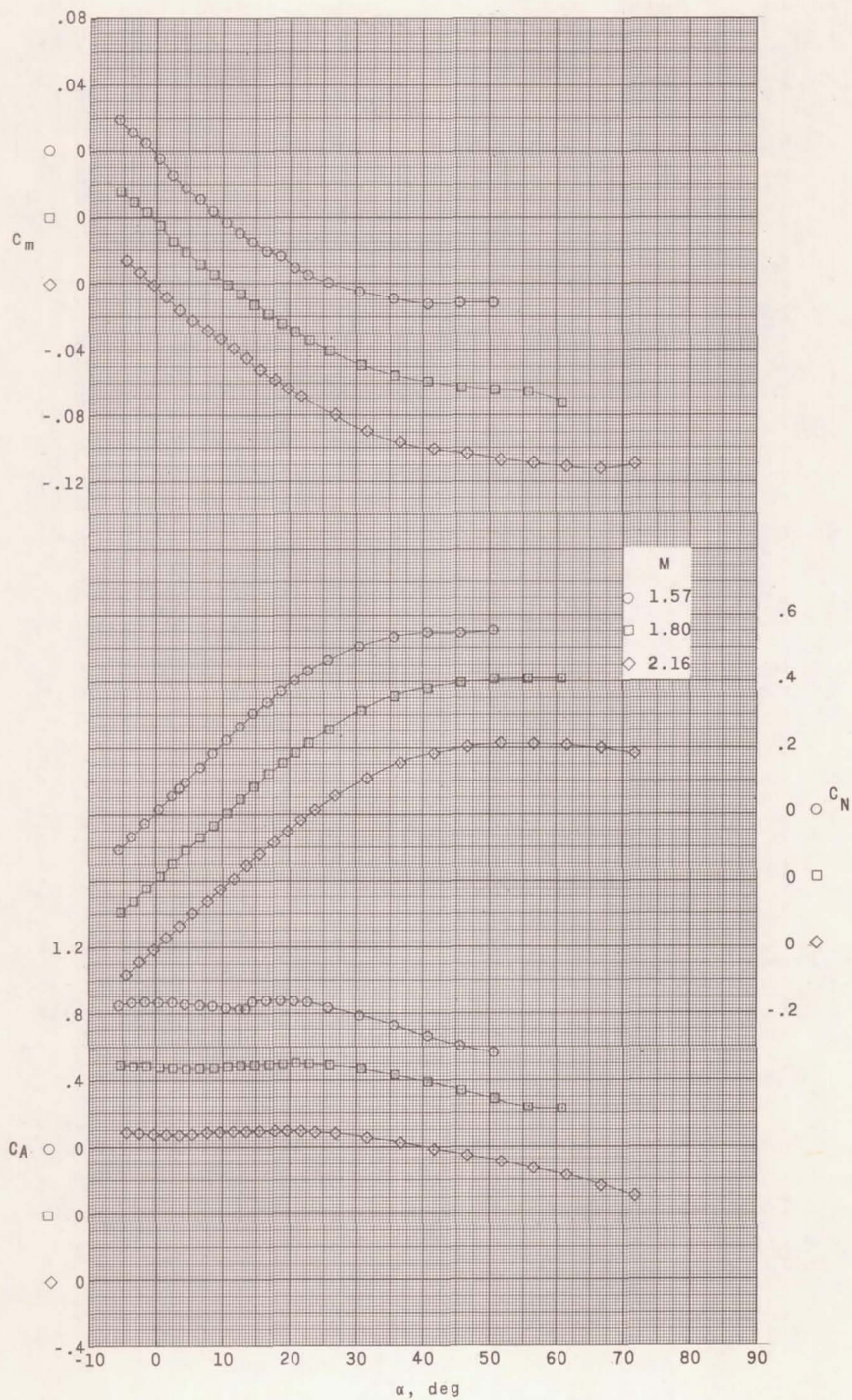
(c) Model 1121; $K = 0$ percent; $\lambda = 1/2$; $\theta = 15^\circ$; base, flat.

Figure 6.- Continued.



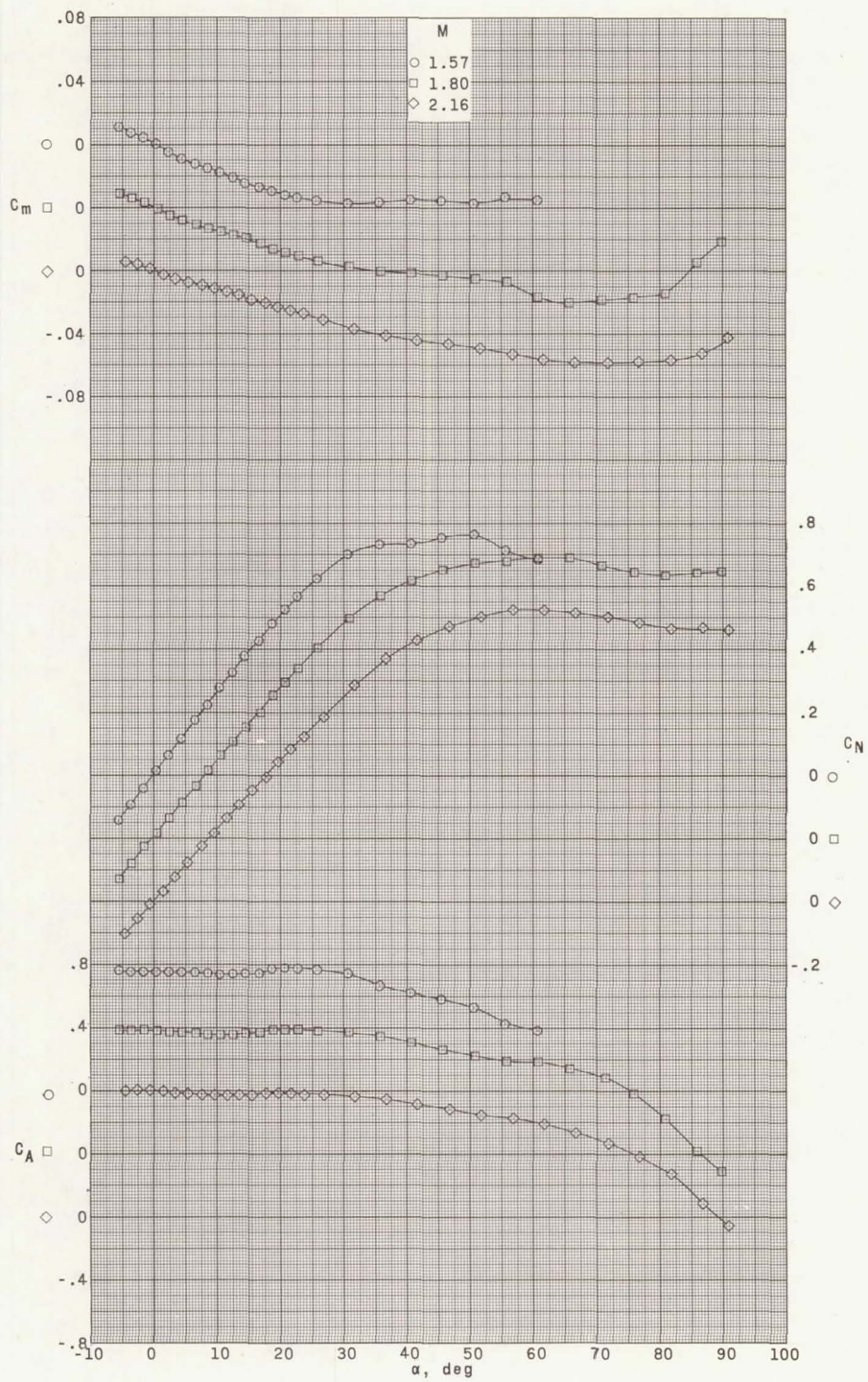
(d) Model 1122; $K = 0$ percent; $\lambda = 1/2$; $\theta = 15^\circ$; base, convex.

Figure 6.- Continued.



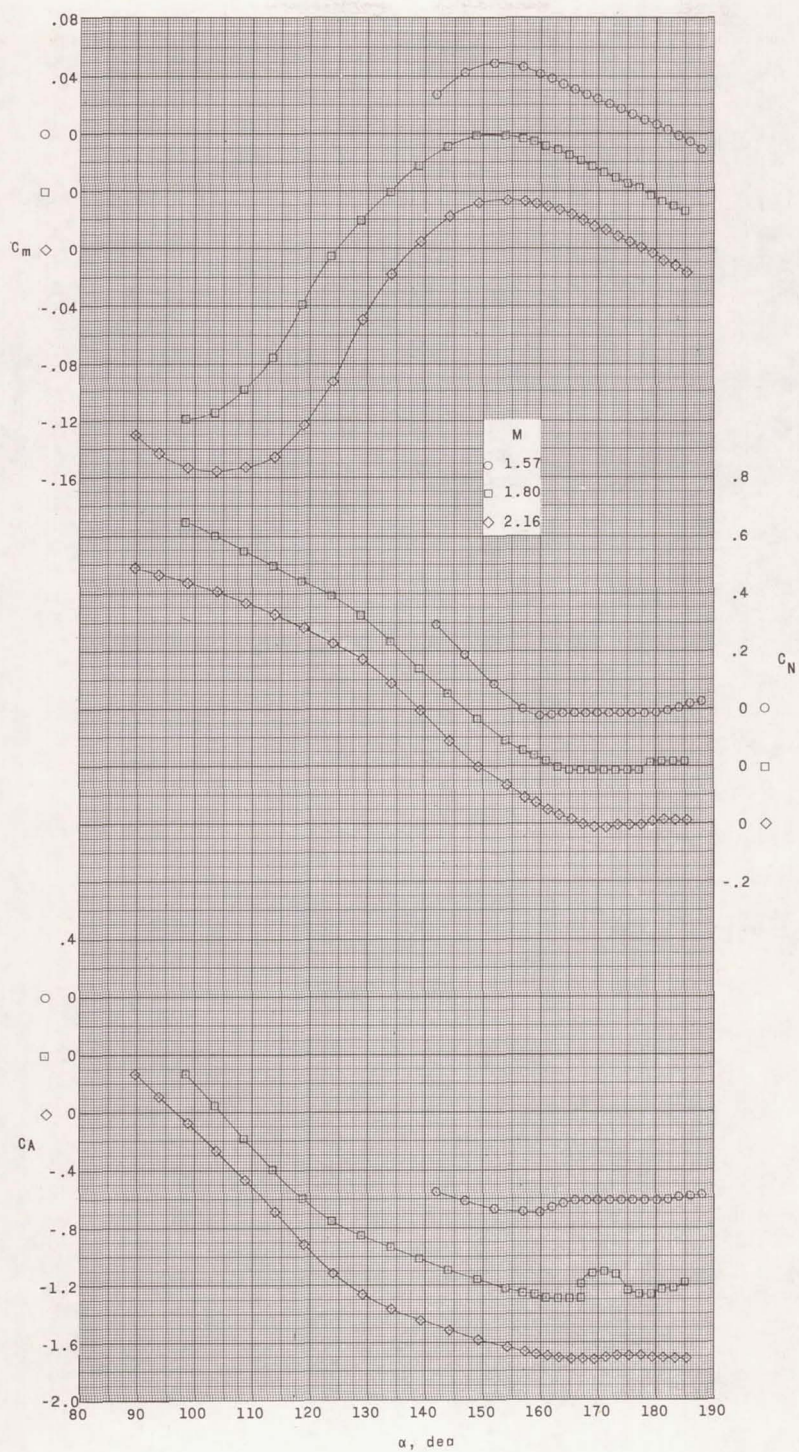
(e) Model 1131; $K = 0$ percent; $\lambda = 1/2$; $\theta = 20^\circ$; base, flat.

Figure 6.- Continued.



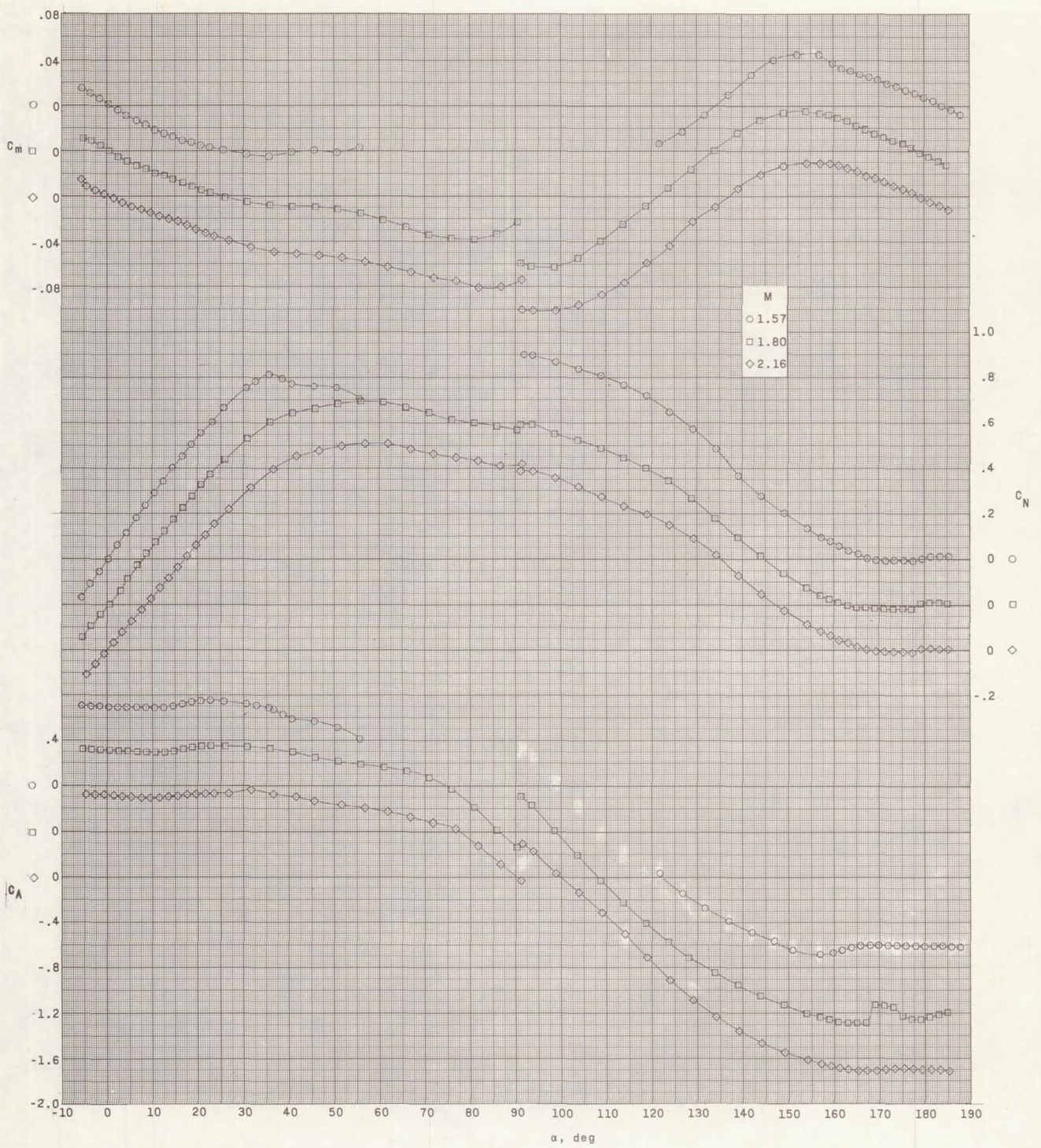
(f) Model 1212; $K = 0$ percent; $\lambda = 3/4$; $\theta = 10^\circ$; base, convex.

Figure 6.- Continued.



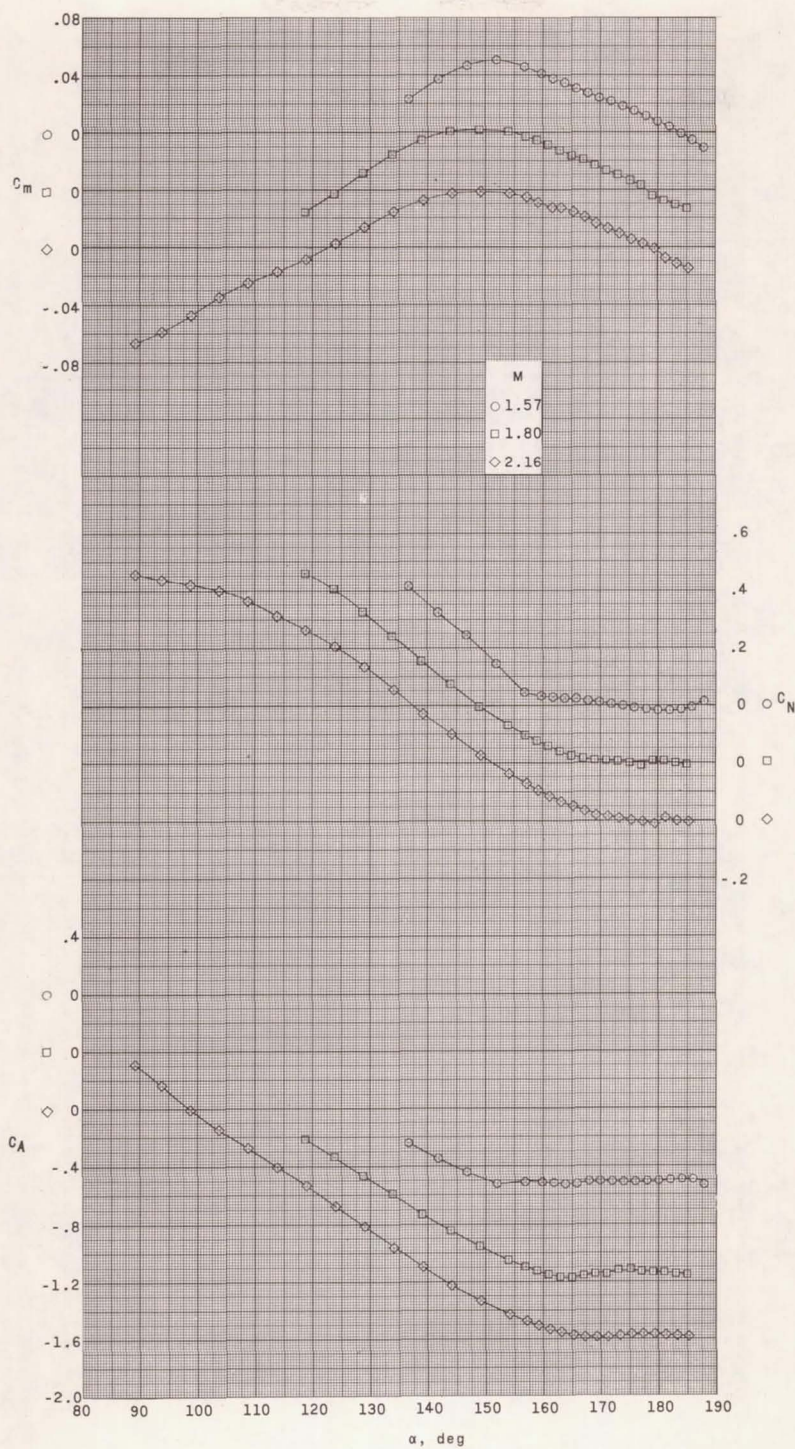
(g) Model 1213; $K = 0$ percent; $\lambda = 3/4$; $\theta = 10^\circ$; base, concave.

Figure 6.- Continued.



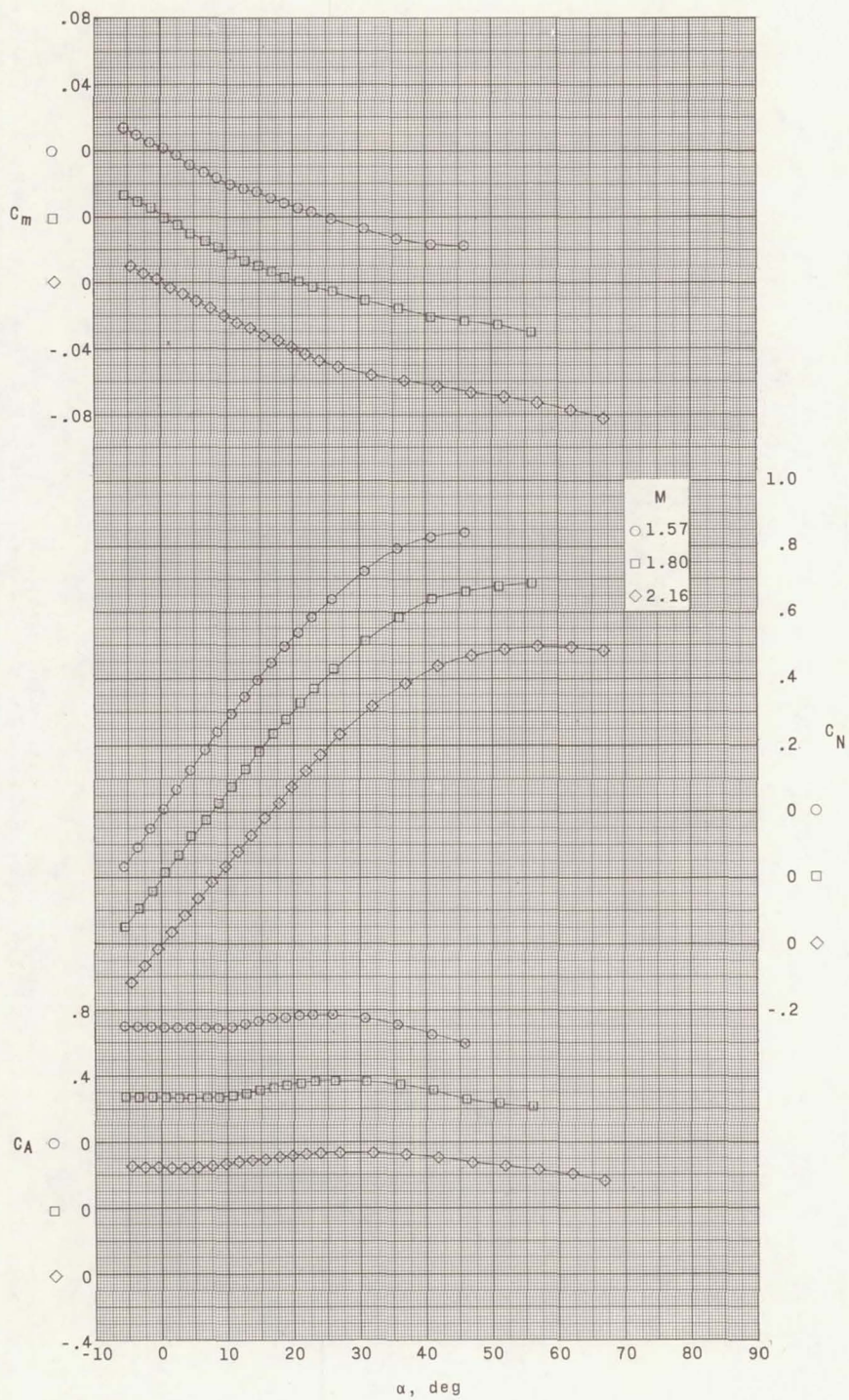
(h) Model 1221; $K = 0$ percent; $\lambda = 3/4$; $\theta = 15^\circ$; base, flat.

Figure 6.- Continued.



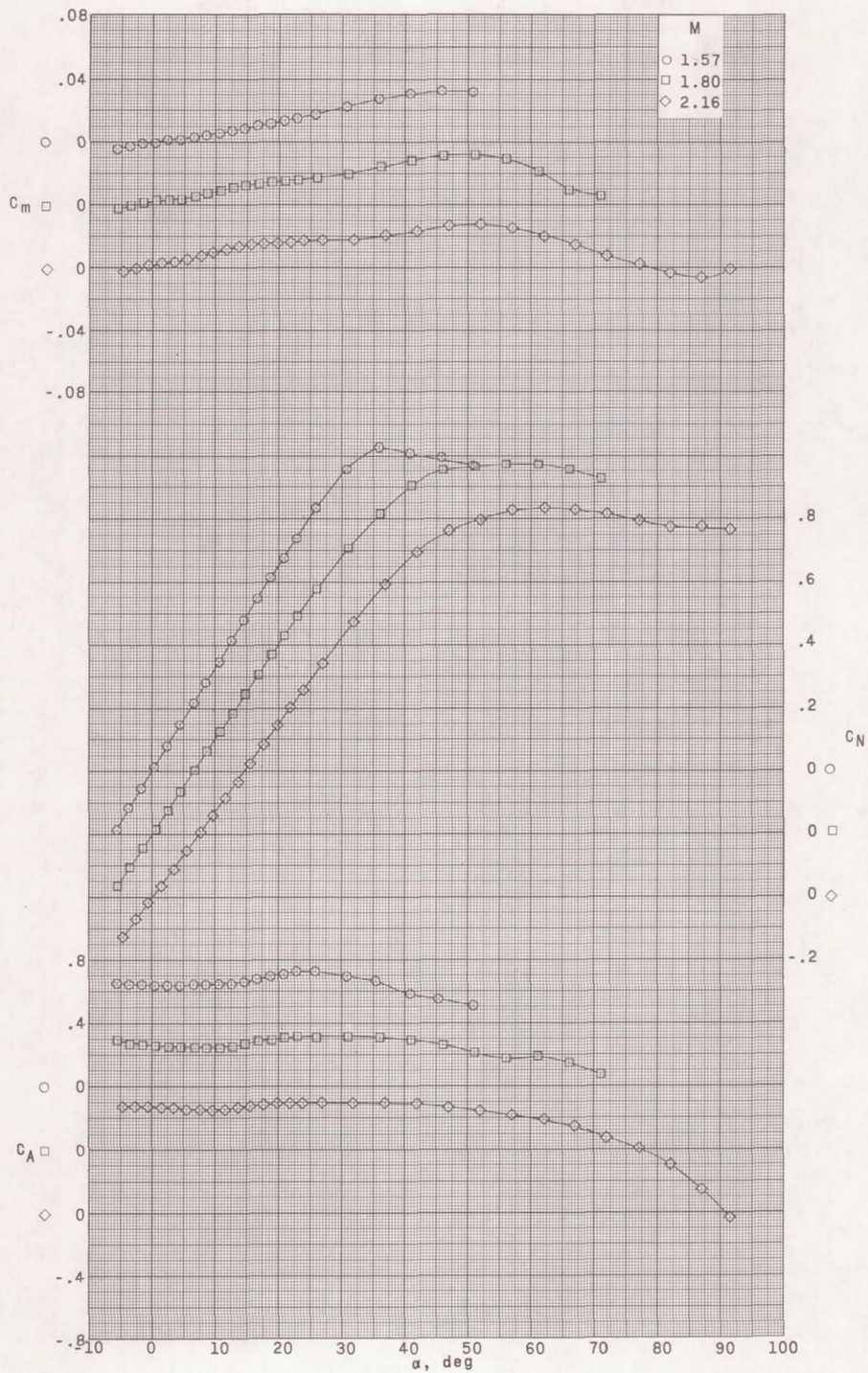
(i) Model 1222; $K = 0$ percent; $\lambda = 3/4$; $\theta = 15^\circ$; base, convex.

Figure 6.- Continued.



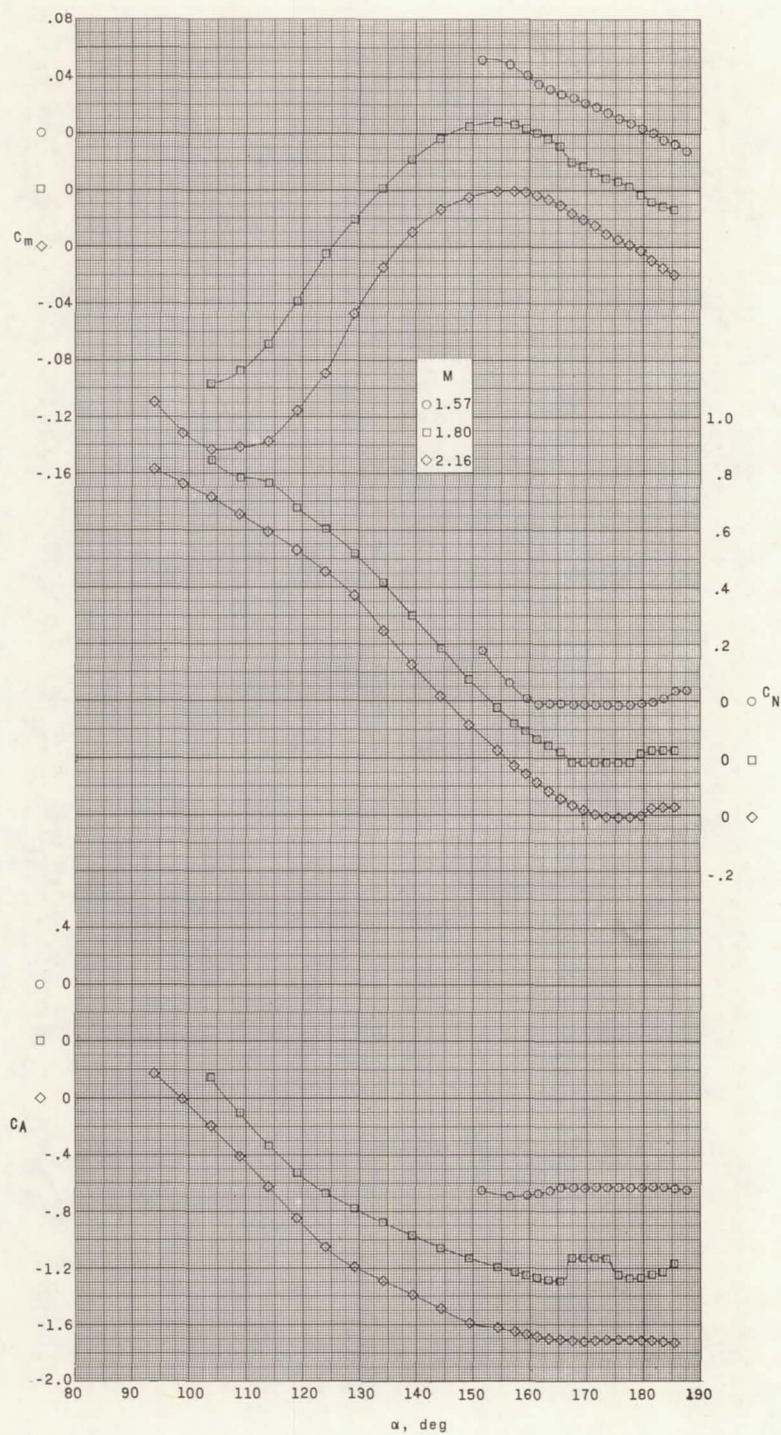
(j) Model 1231; $K = 0$ percent; $\lambda = 3/4$; $\theta = 20^\circ$; base, flat.

Figure 6.- Continued.



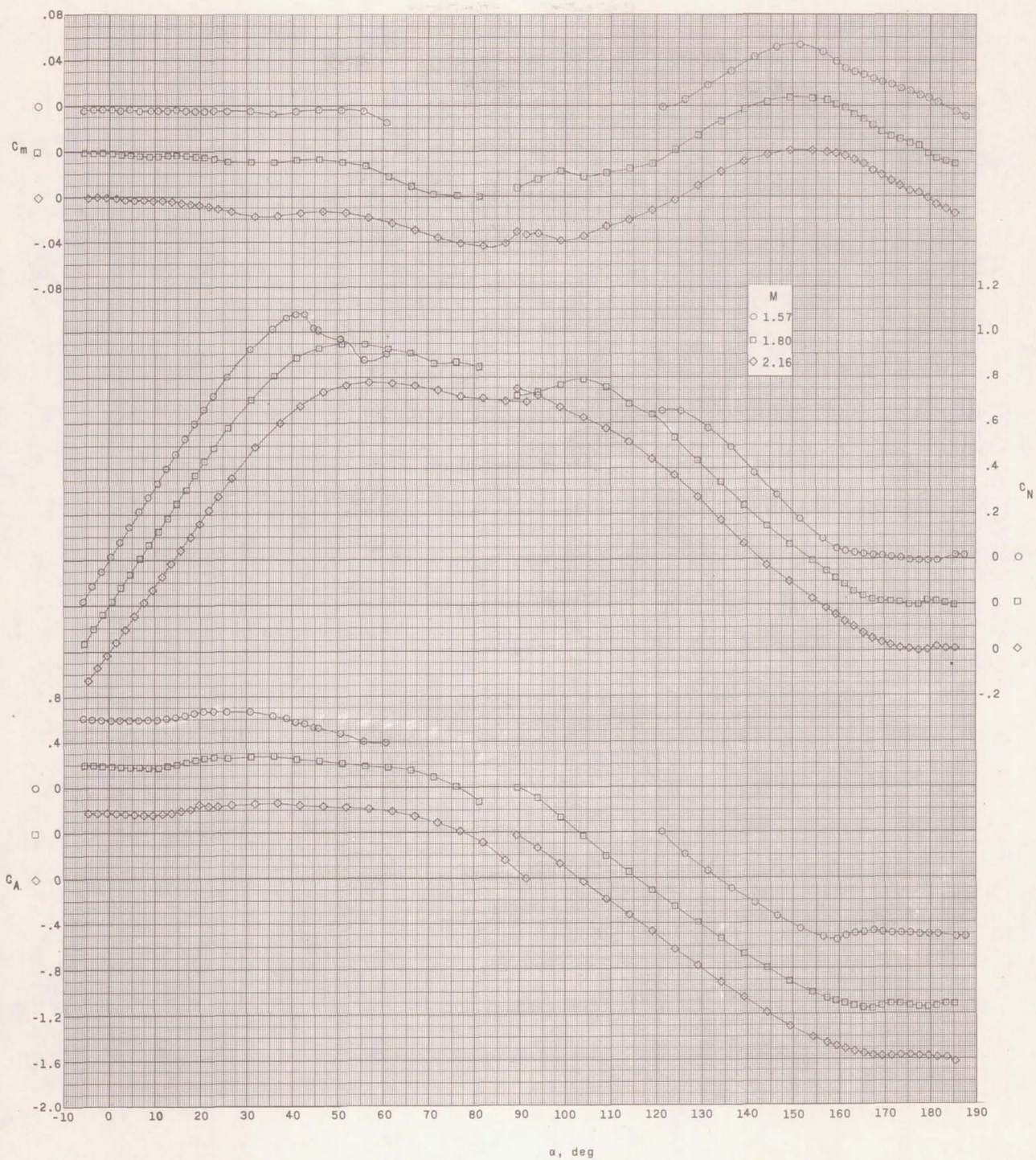
(k) Model 1312. $K = 0$ percent; $\lambda = 1$; $\theta = 10^\circ$; base, convex.

Figure 6.- Continued.



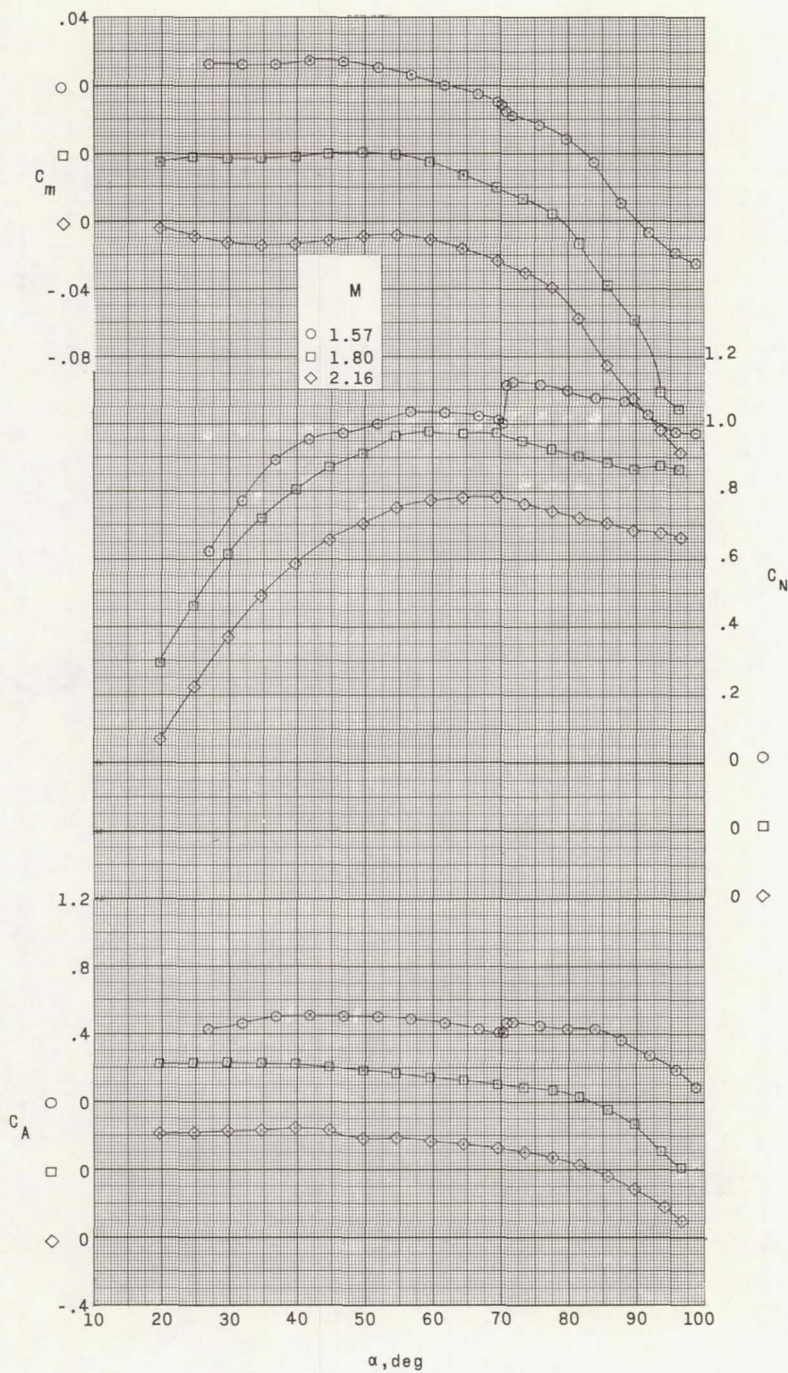
(1) Model 1313; $K = 0$ percent; $\lambda = 1$; $\theta = 10^\circ$; base, concave.

Figure 6.- Continued.



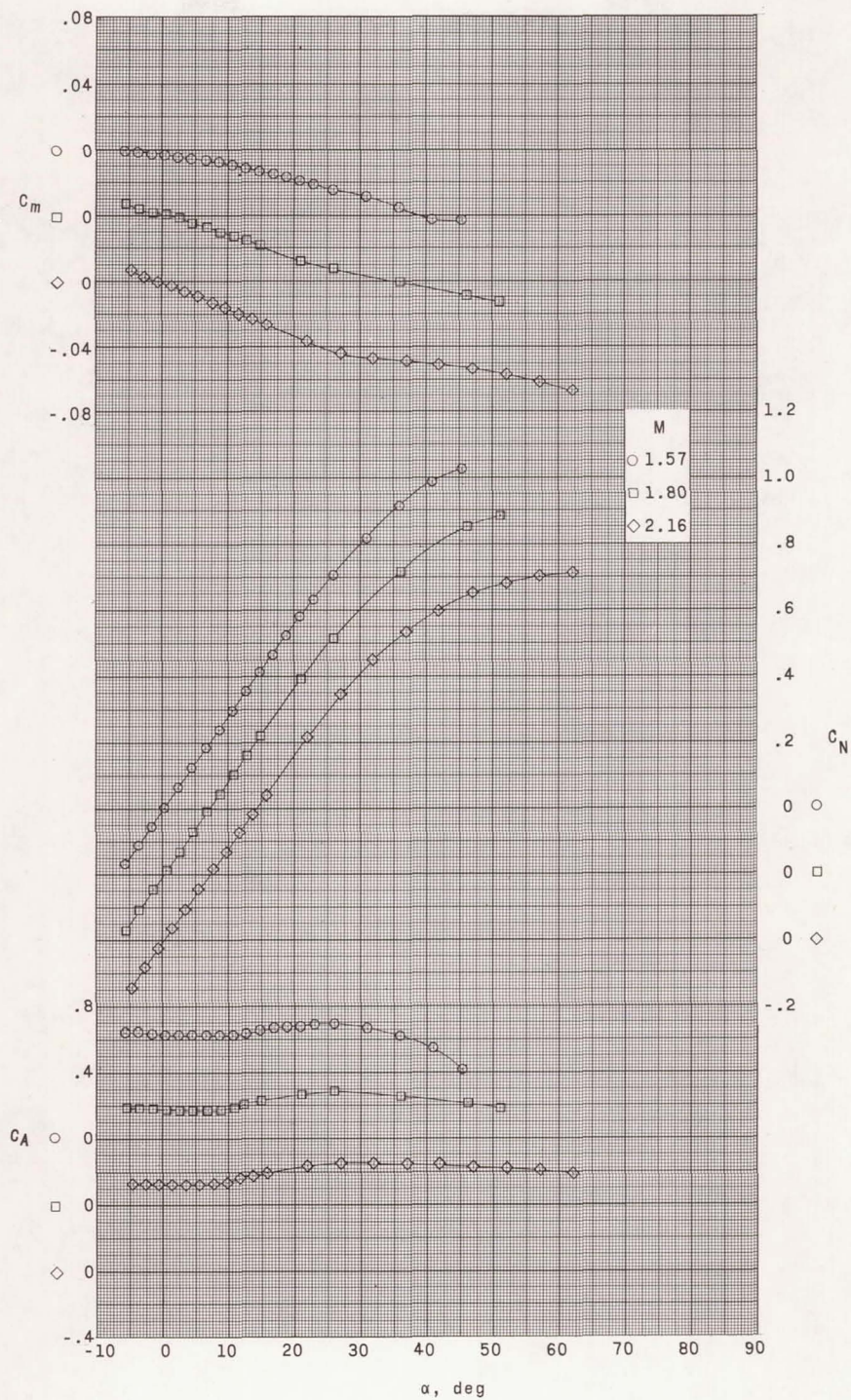
(m) Model 1322; $K = 0$ percent; $\lambda = 1$; $\theta = 15^\circ$; base, convex.

Figure 6.- Continued.



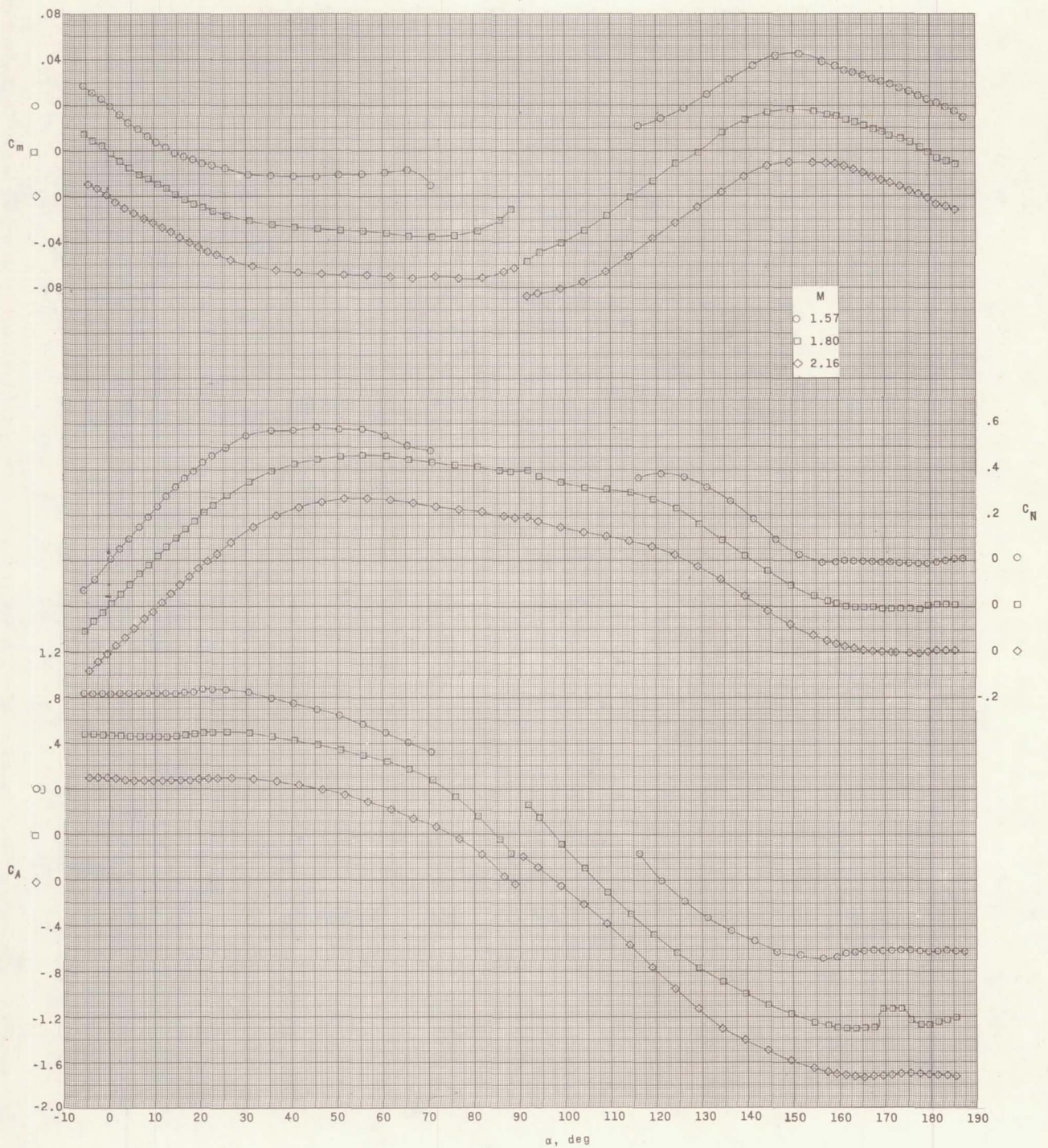
(n) Model 1323; $K = 0$ percent; $\lambda = 1$; $\theta = 15^\circ$; base, concave.

Figure 6.- Continued.



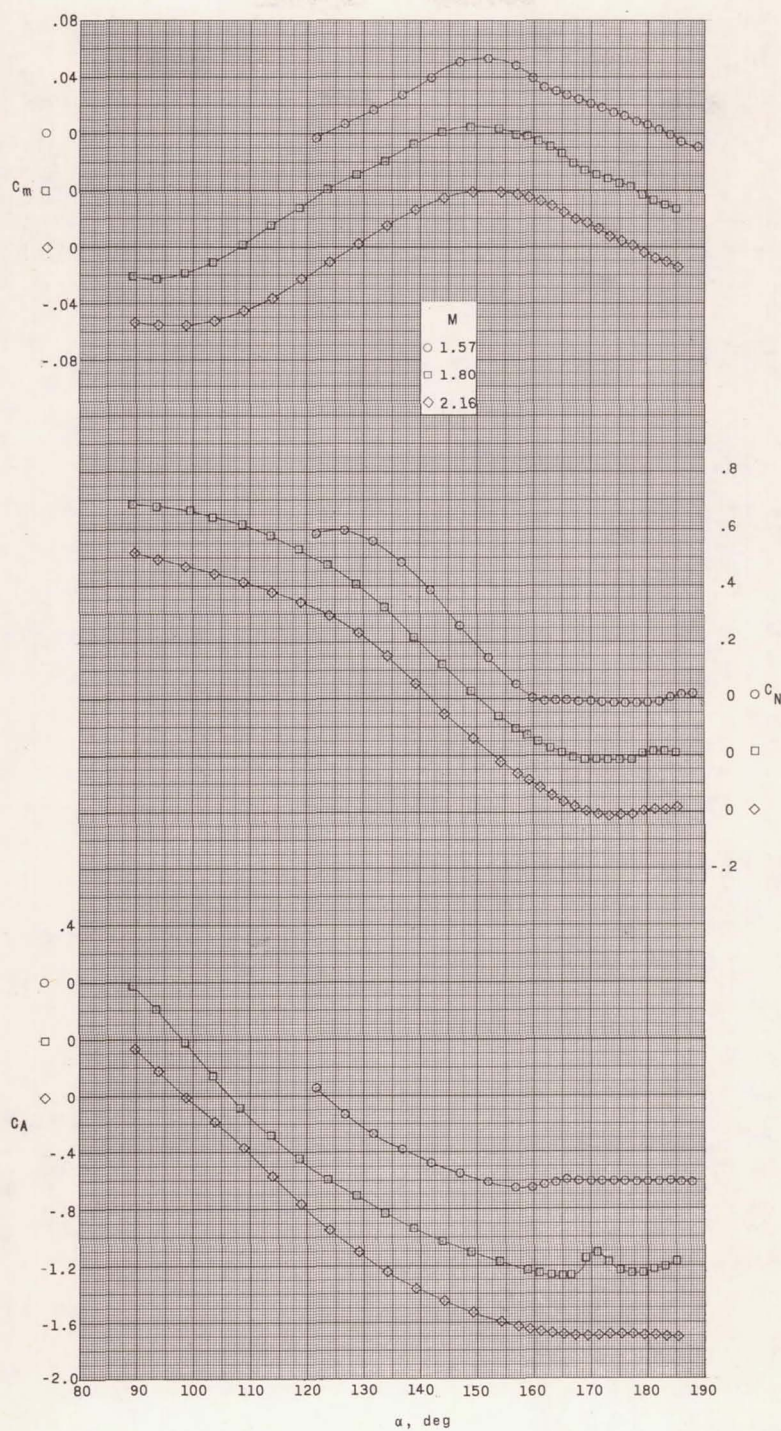
(o) Model 1331; $K = 0$ percent; $\lambda = 1$; $\theta = 20^\circ$; base, flat.

Figure 6.- Concluded.



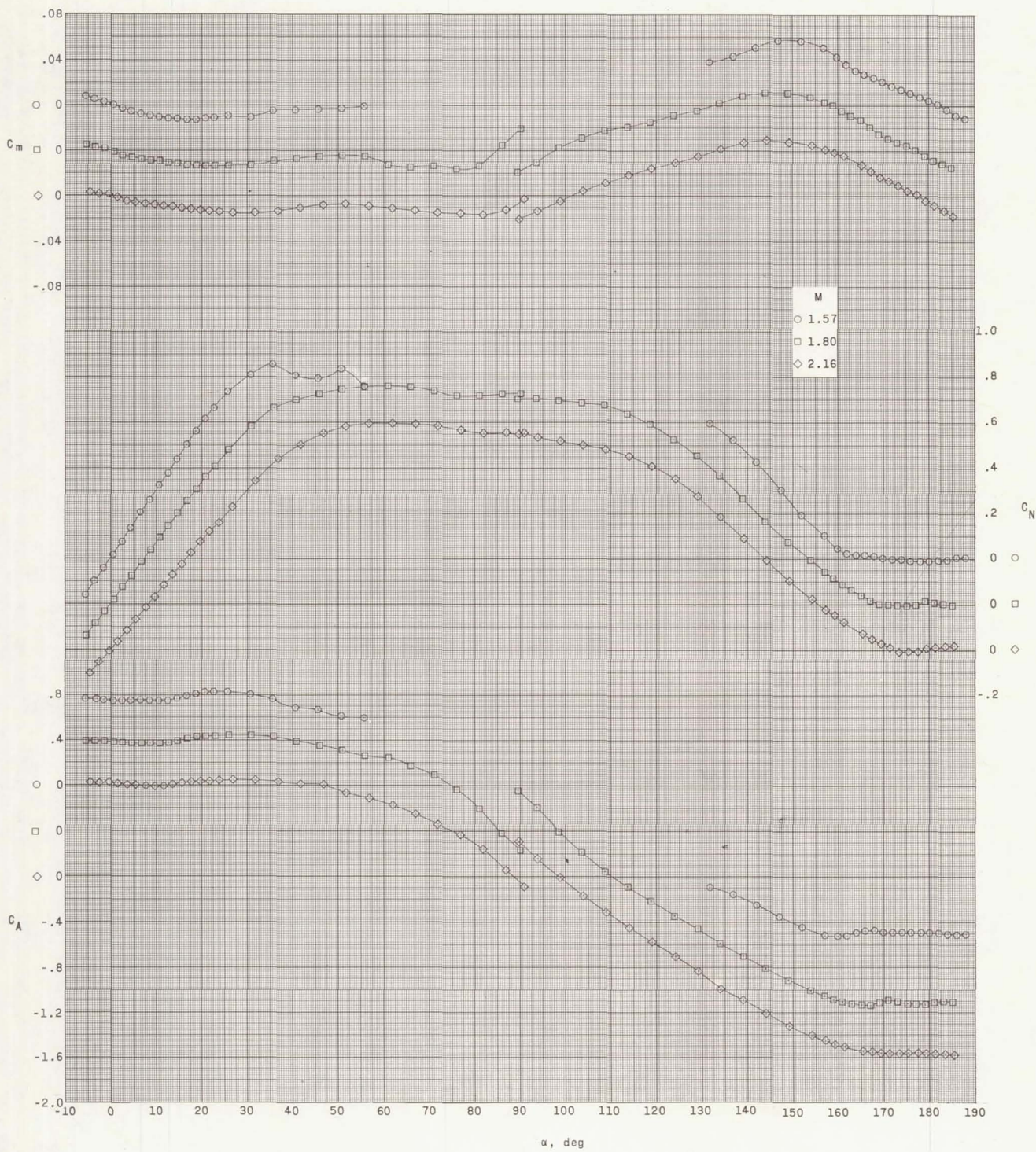
(a) Model 2121; $K = 50$ percent; $\lambda = 1/2$; $\theta = 15^\circ$; base, flat.

Figure 7.- Aerodynamic characteristics in pitch of models having nose bluntness of 50-percent flat face.



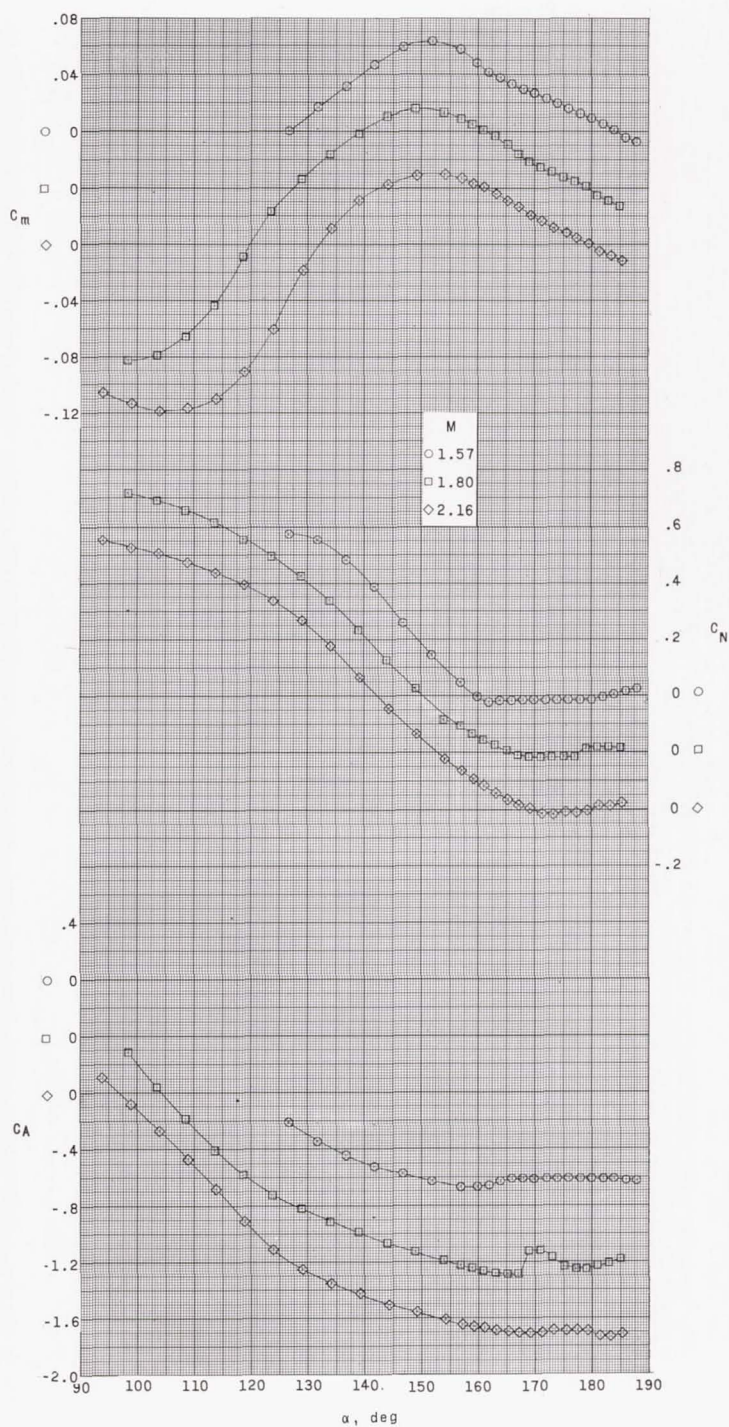
(b) Model 2211; $K = 50$ percent; $\lambda = 3/4$; $\theta = 10^\circ$; base, flat.

Figure 7.- Continued.



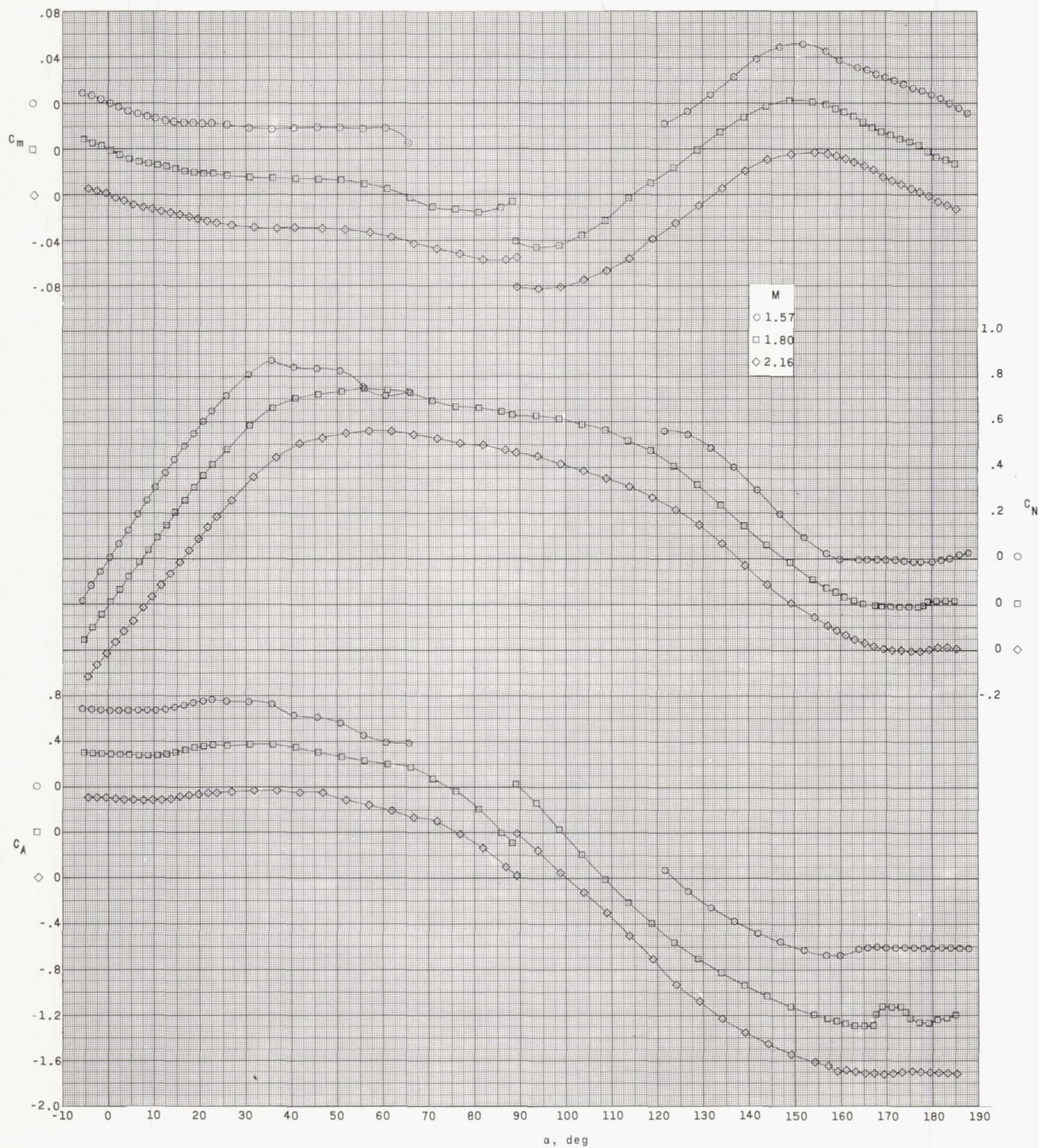
(c) Model 2212; $K = 50$ percent; $\lambda = 3/4$; $\theta = 10^\circ$; base, convex.

Figure 7.- Continued.



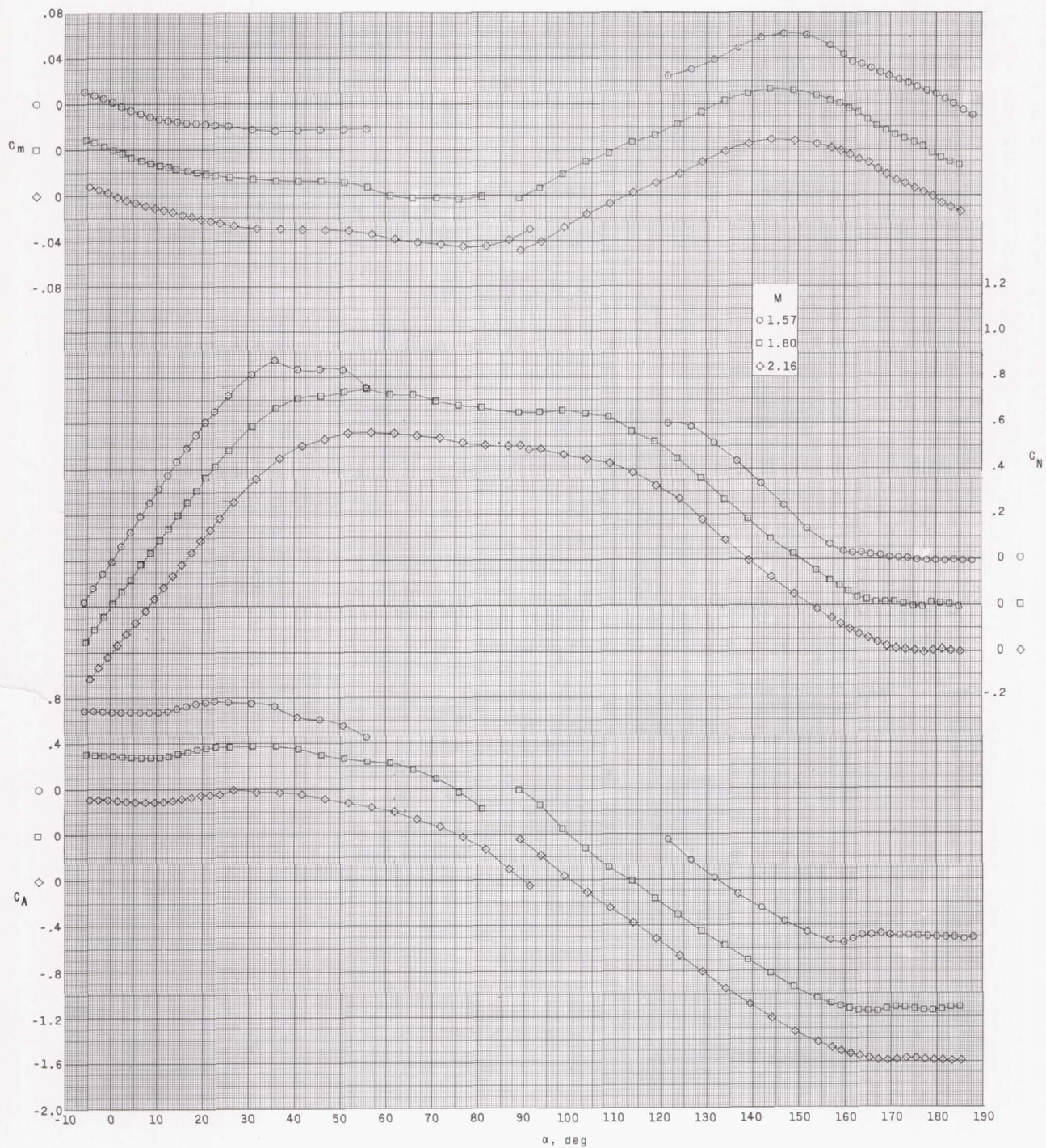
(d) Model 2213; $K = 50$ percent; $\lambda = 3/4$; $\theta = 10^\circ$; base, concave.

Figure 7.- Continued.



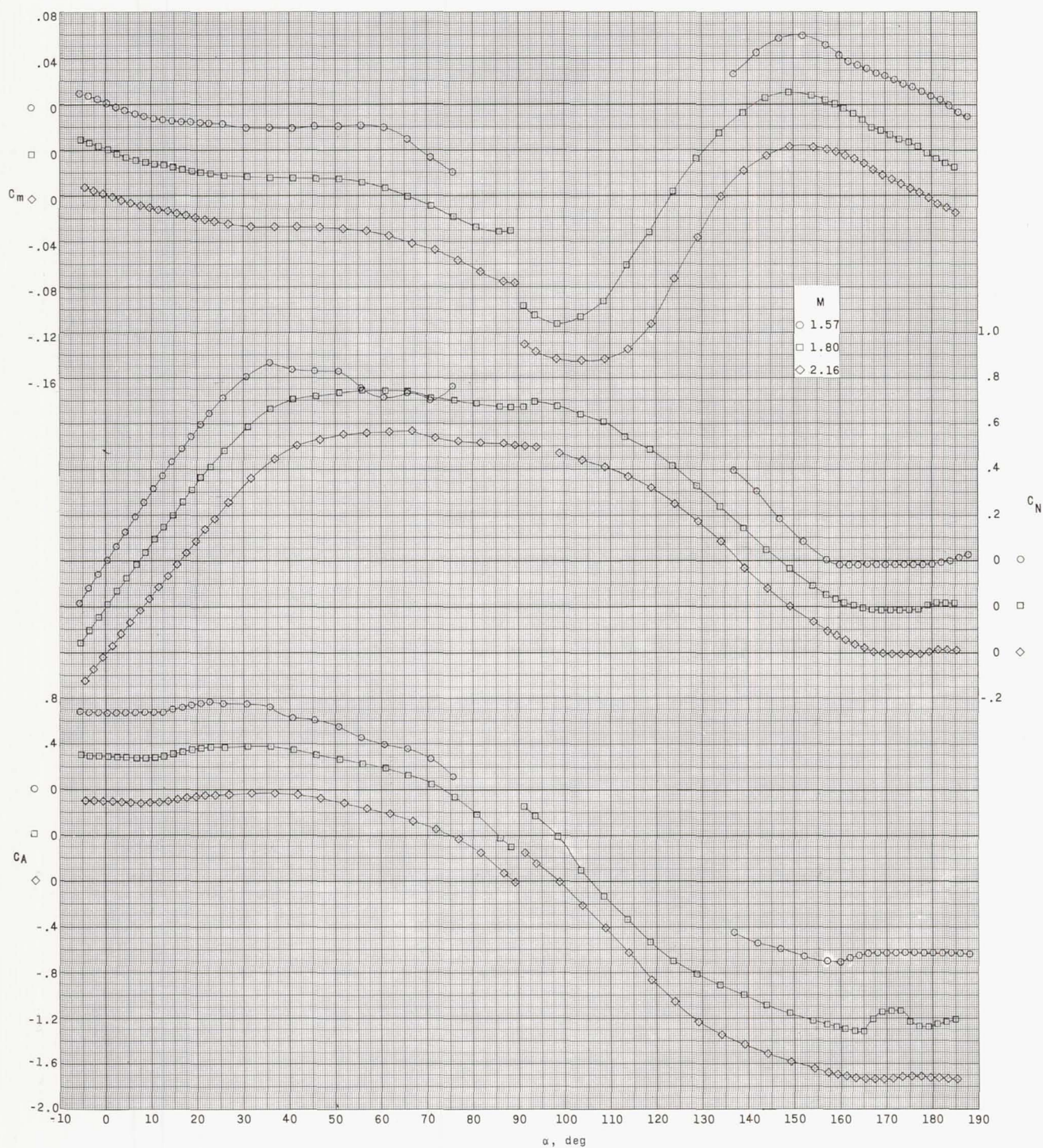
(e) Model 2221; $K = 50$ percent; $\lambda = 3/4$; $\theta = 15^\circ$; base, flat.

Figure 7.- Continued.



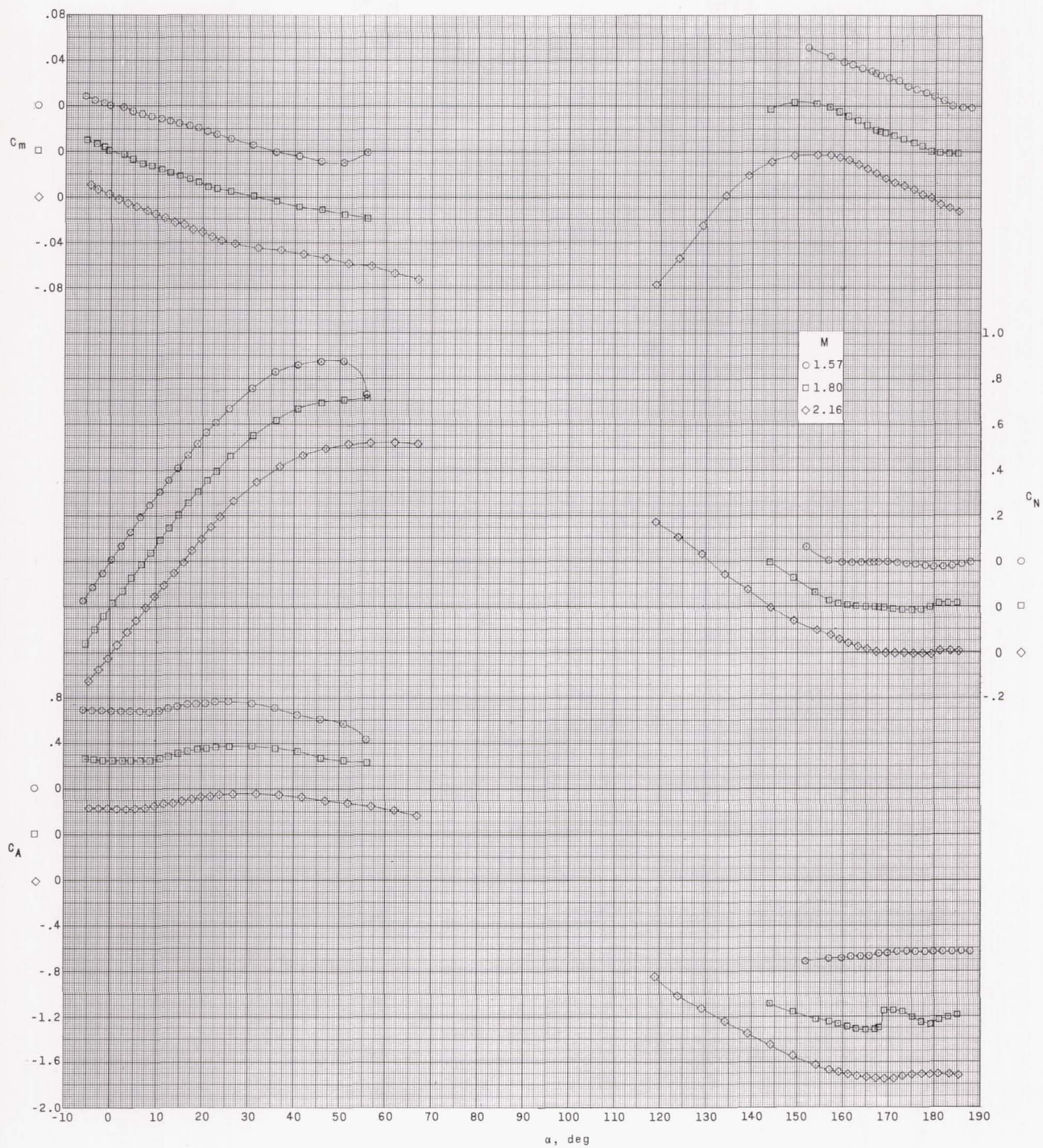
(f) Model 2222; $K = 50$ percent; $\lambda = 3/4$; $\theta = 15^\circ$; base, convex.

Figure 7.- Continued.



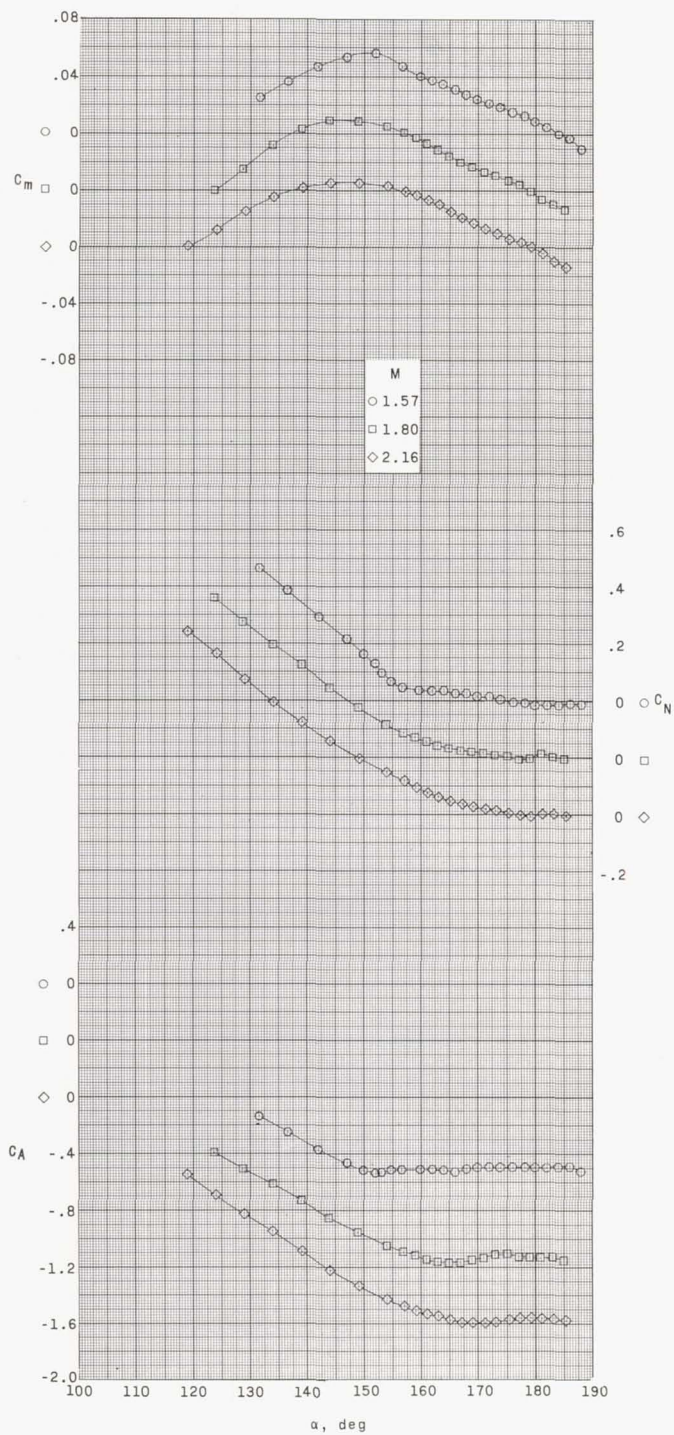
(g) Model 2223; K = 50 percent; $\lambda = 3/4$; $\theta = 15^\circ$; base, concave.

Figure 7.- Continued.



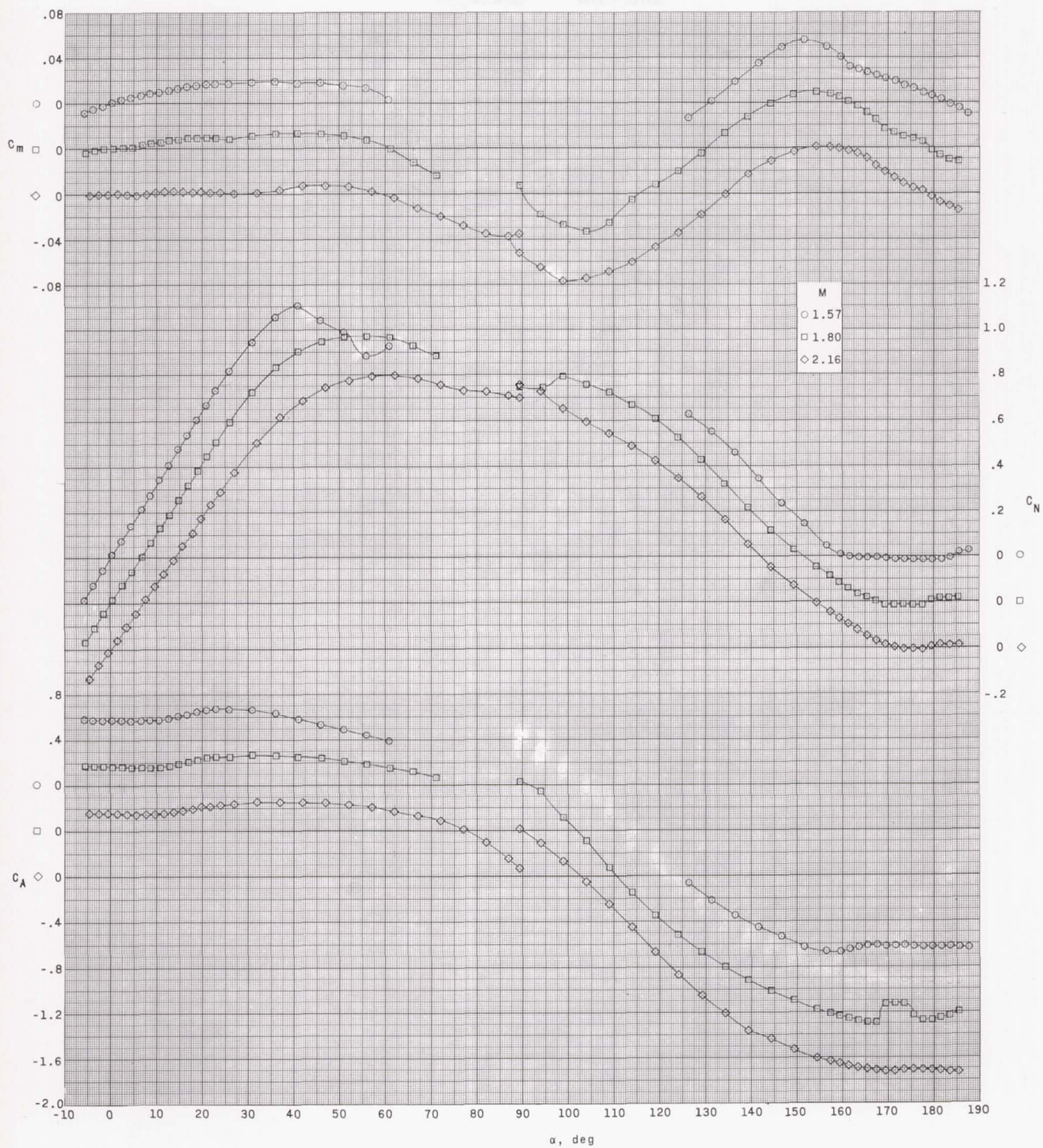
(h) Model 2231; $K = 50$ percent; $\lambda = 3/4$; $\theta = 20^\circ$; base, flat.

Figure 7.- Continued.



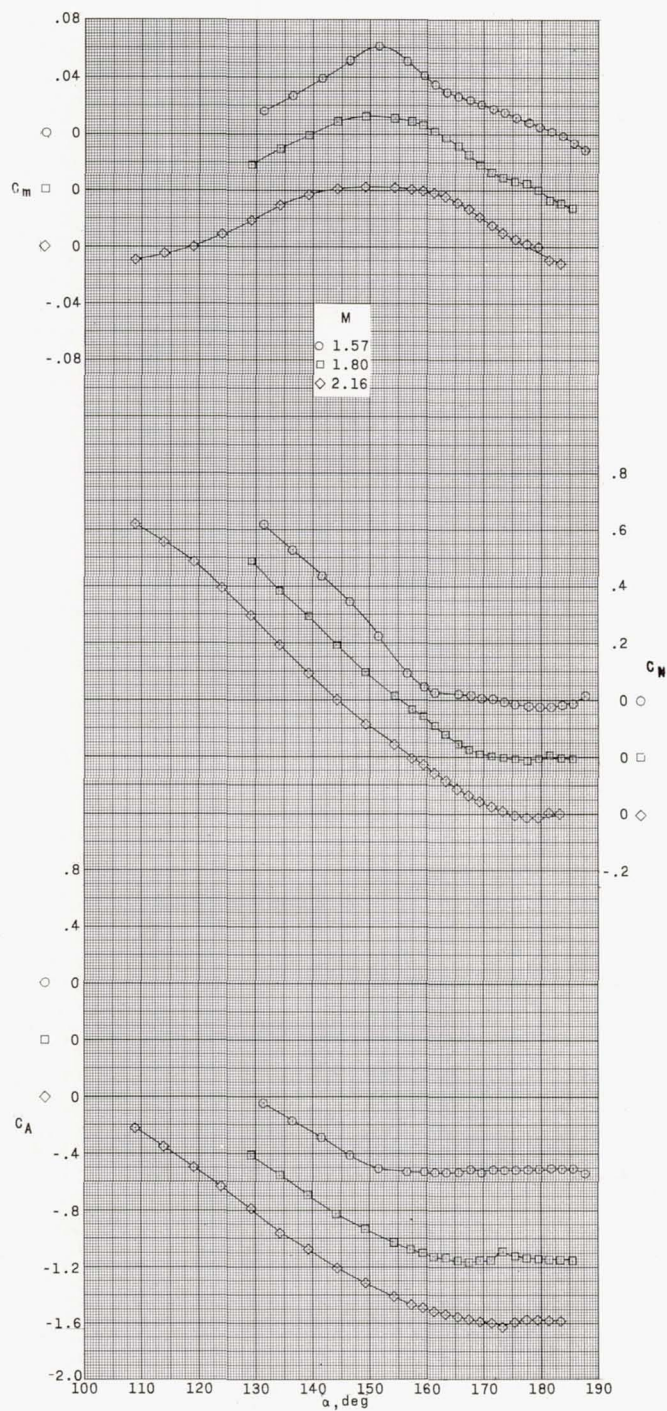
(i) Model 2232; $K = 50$ percent; $\lambda = 3/4$; $\theta = 20^\circ$; base, convex.

Figure 7.- Continued.



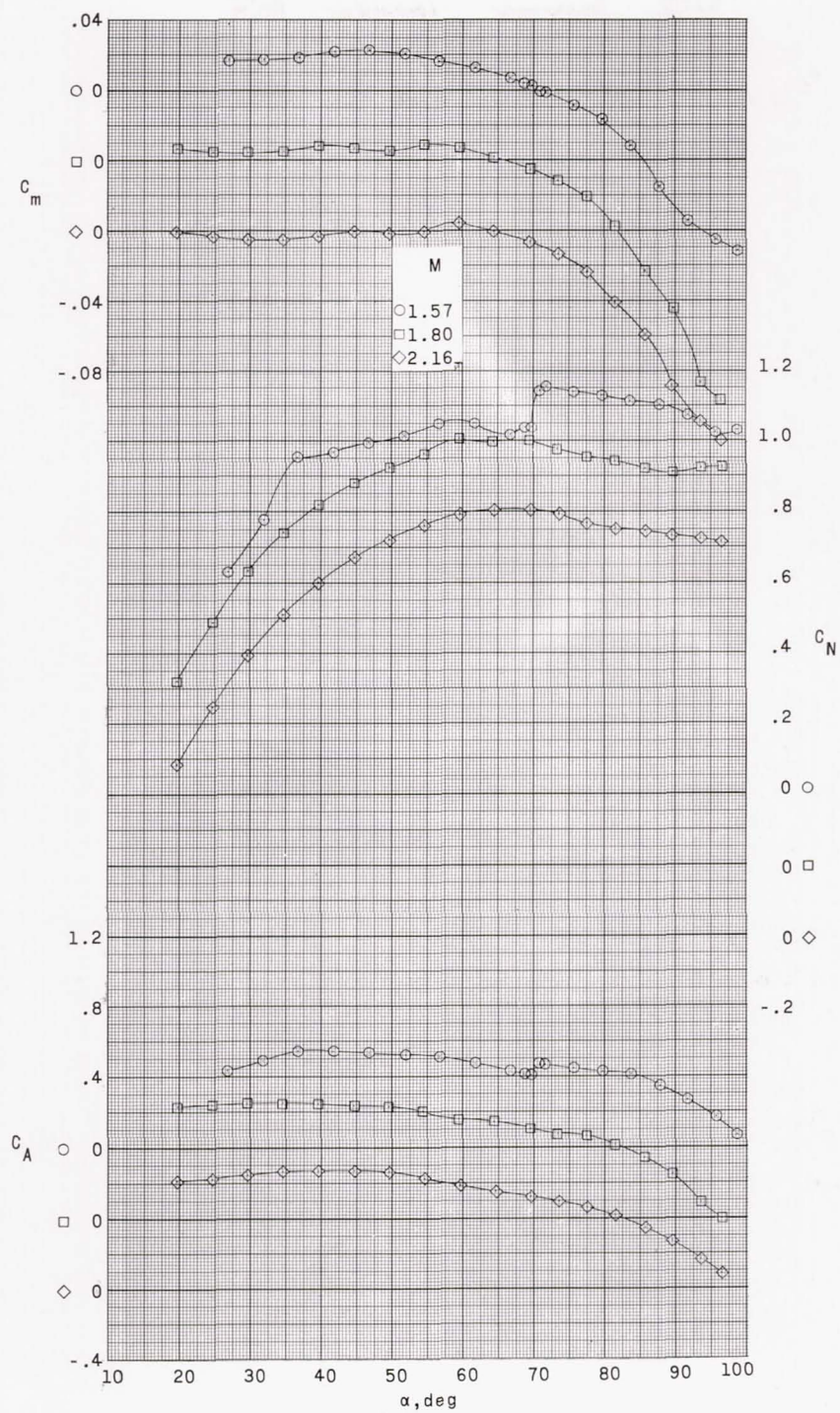
(j) Model 2321; $K = 50$ percent; $\lambda = 1$; $\theta = 15^\circ$; base, flat.

Figure 7.- Continued.



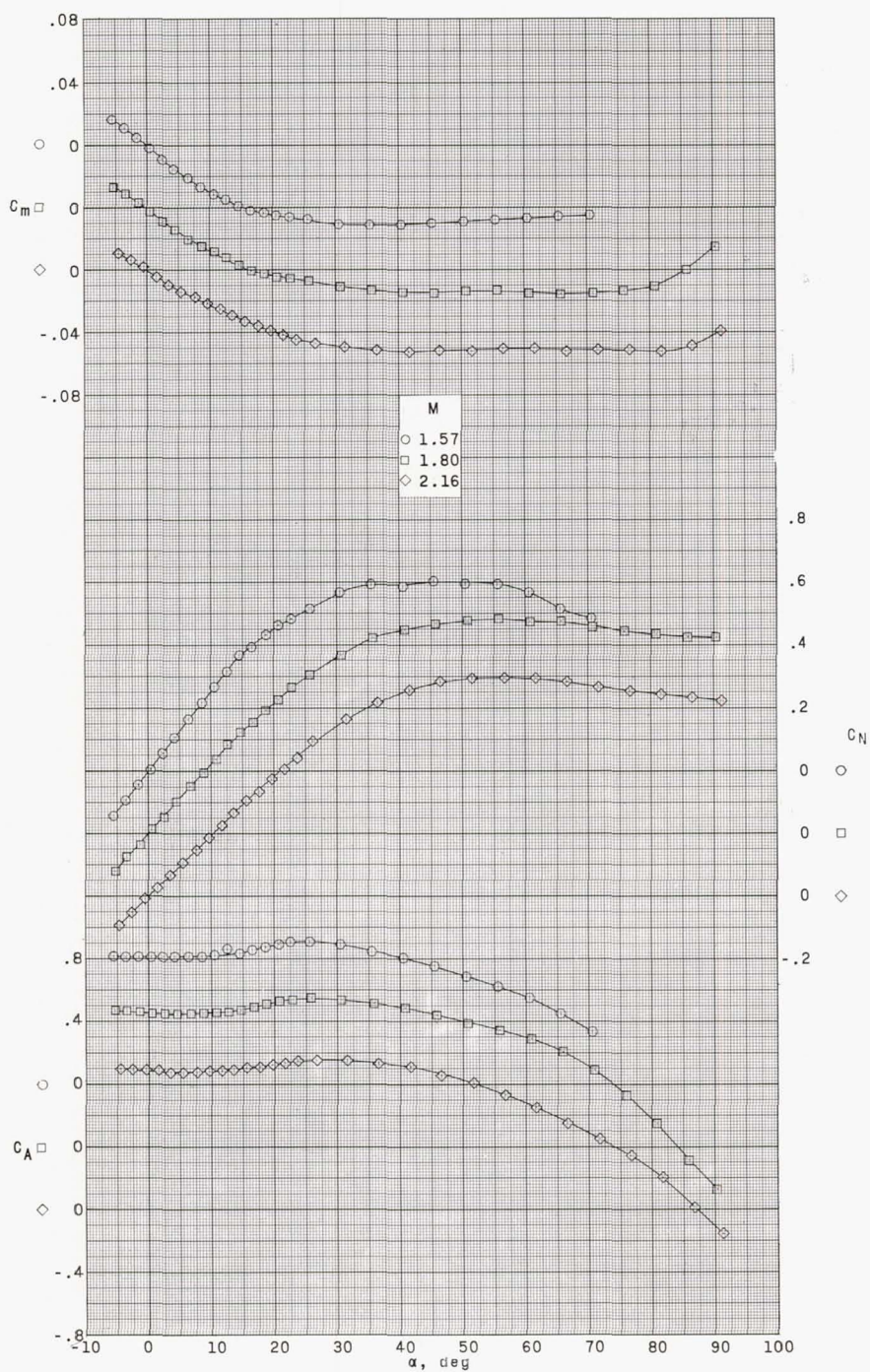
(k) Model 2322; $K = 50$ percent; $\lambda = 1$; $\theta = 15^\circ$; base, convex.

Figure 7.- Continued.



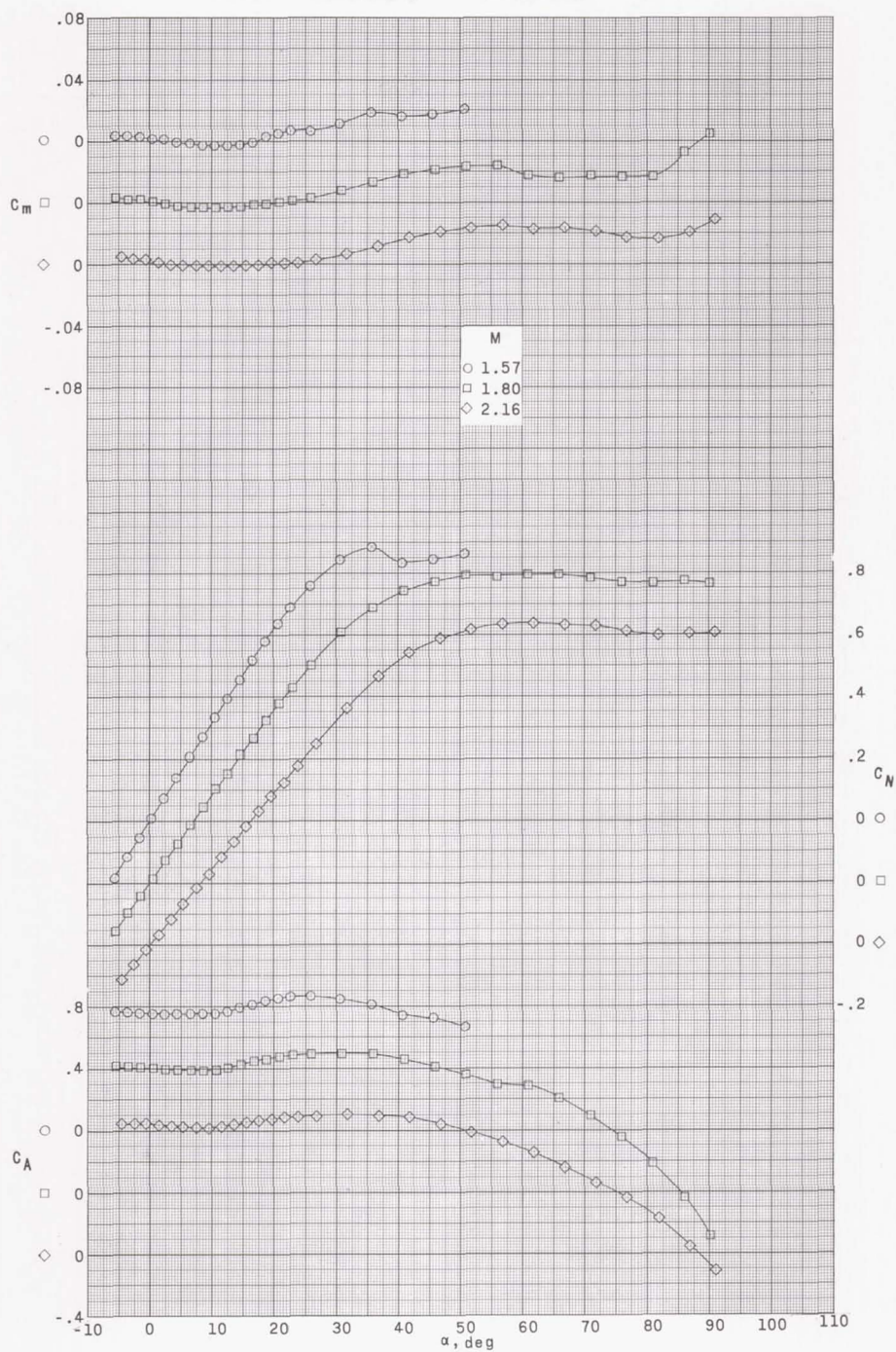
(1) Model 2323; $K = 50$ percent; $\lambda = 1$; $\theta = 15^\circ$; base, concave.

Figure 7.- Concluded.



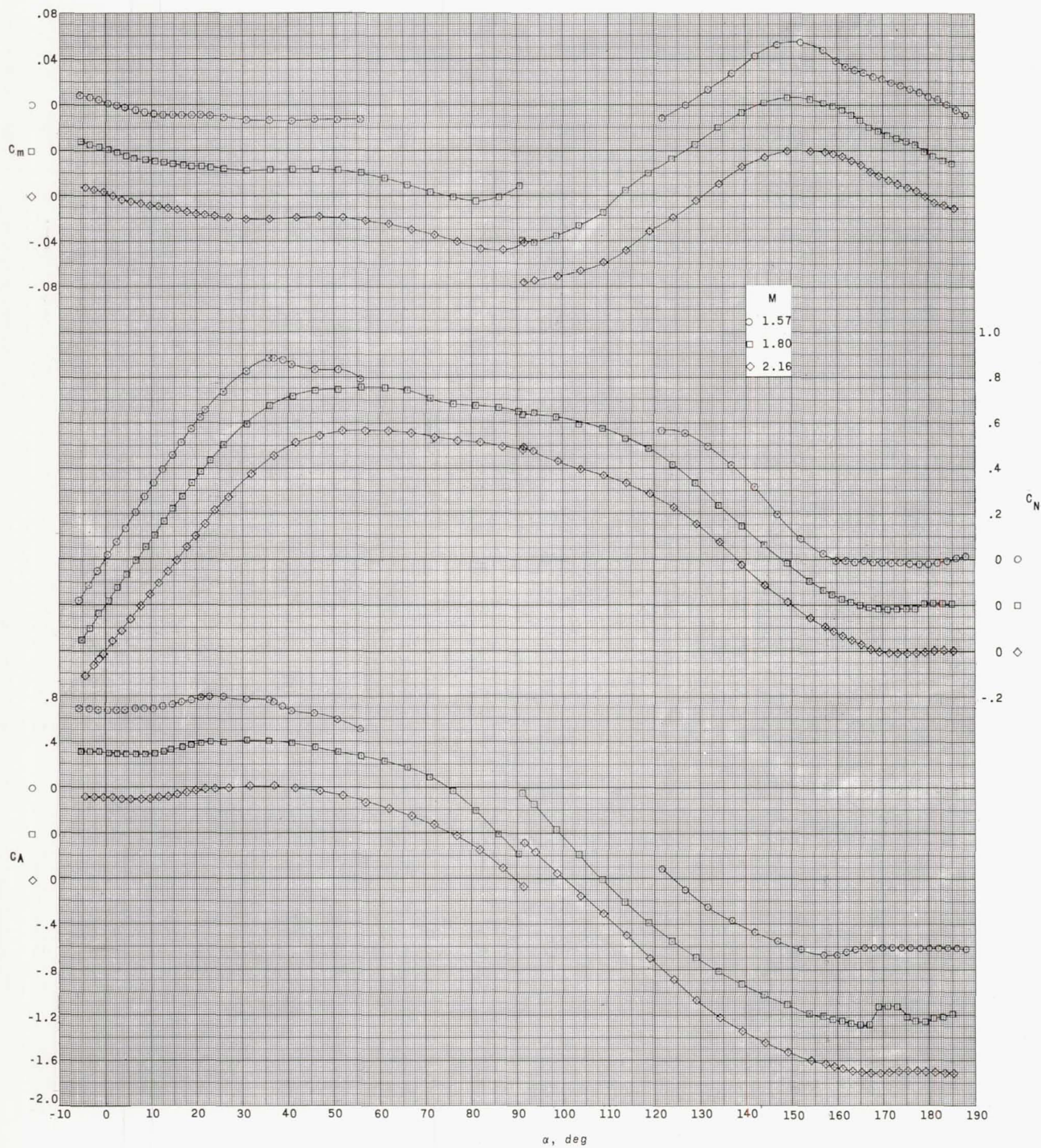
(a) Model 3121; $K = 75$ percent; $\lambda = 1/2$; $\theta = 15^\circ$; base, flat.

Figure 8.- Aerodynamic characteristics in pitch of models having a nose bluntness of 75-percent flat face.



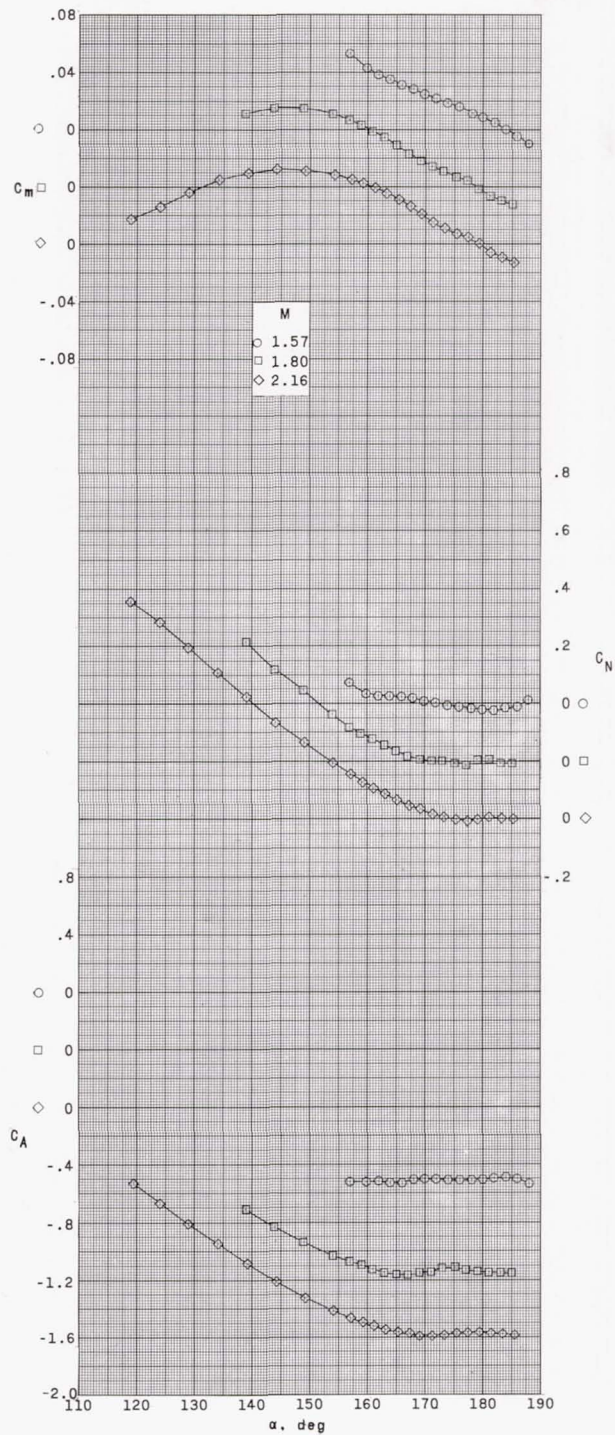
(b) Model 3212; $K = 75$ percent; $\lambda = 3/4$; $\theta = 10^\circ$; base, convex.

Figure 8.- Continued.



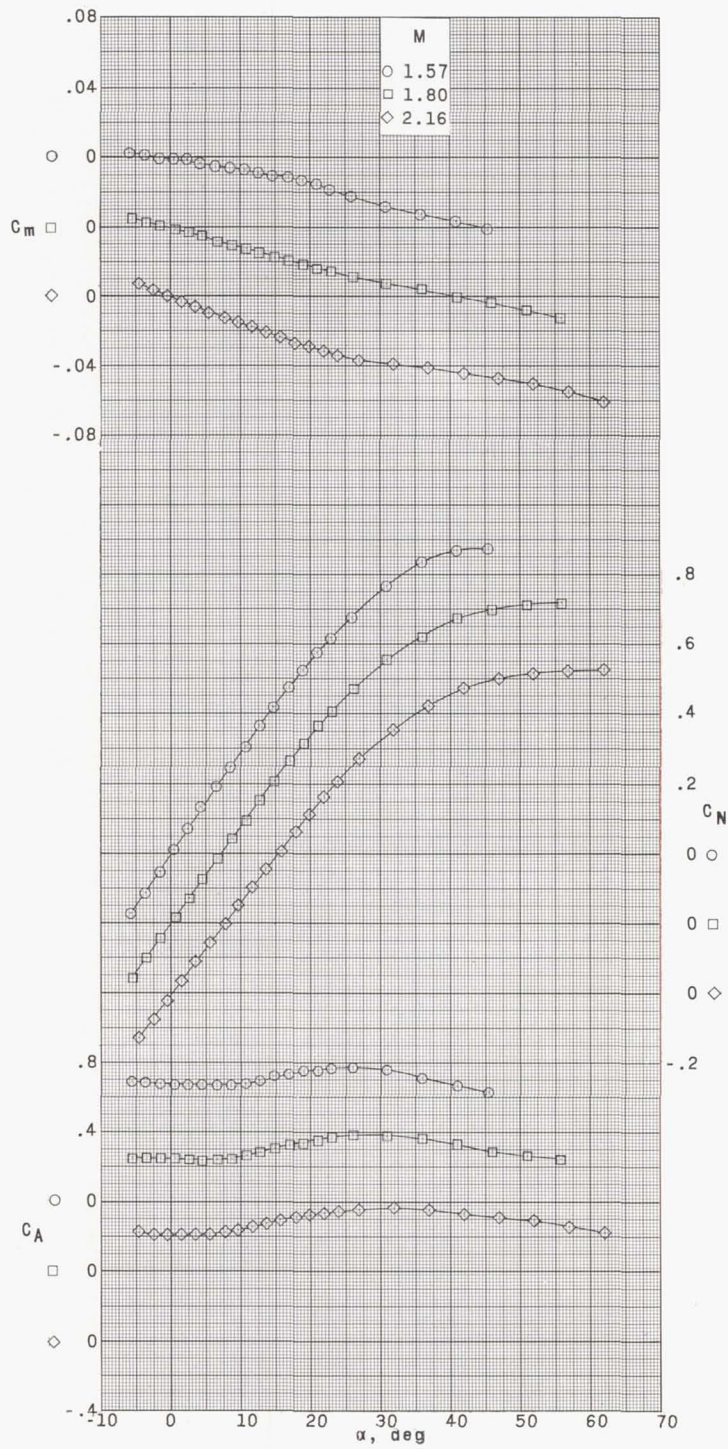
(c) Model 3221; $K = 75$ percent; $\lambda = 3/4$; $\theta = 15^\circ$; base, flat.

Figure 8.- Continued.



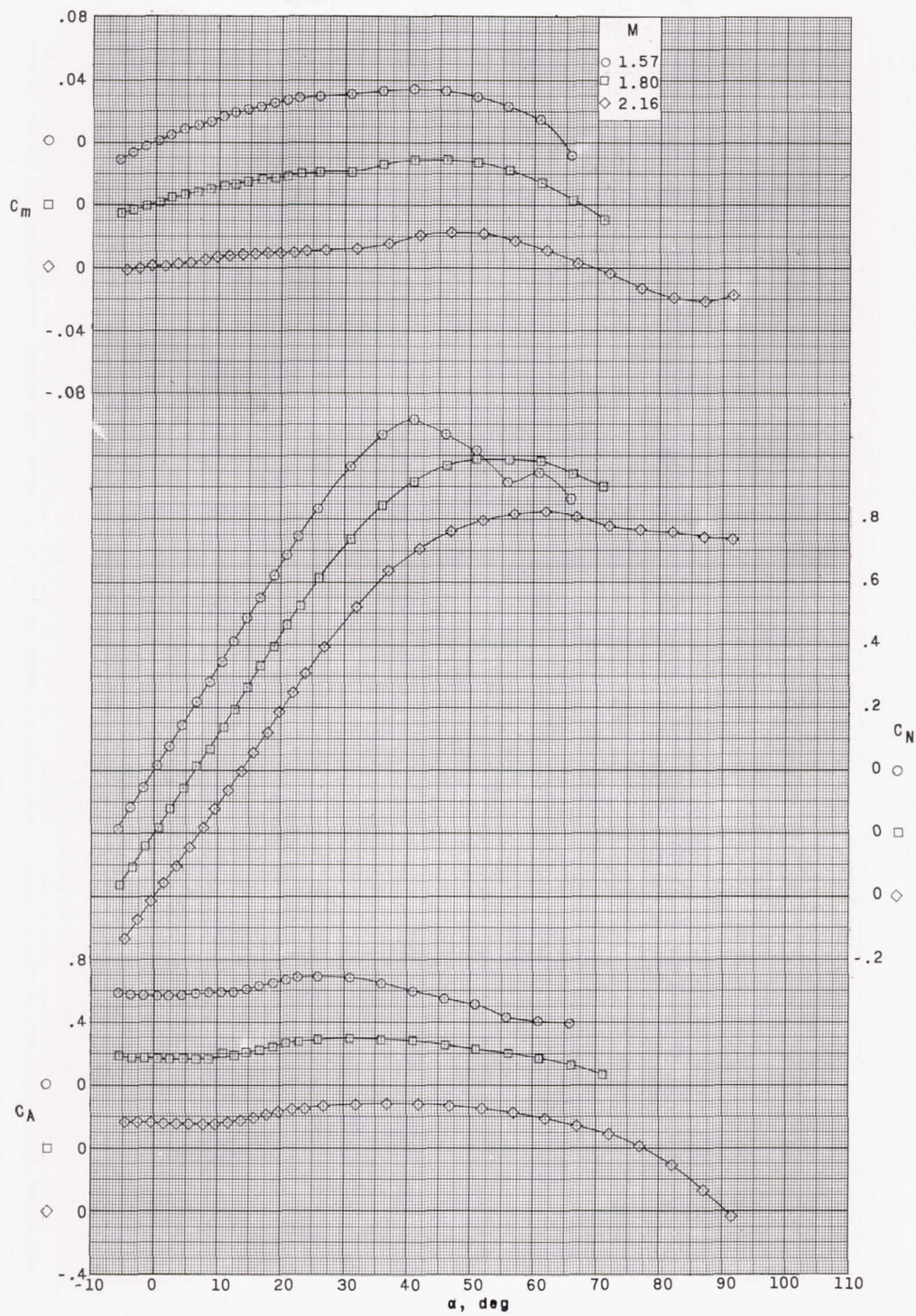
(d) Model 3222; $K = 75$ percent; $\lambda = 3/4$; $\theta = 15^\circ$; base, convex.

Figure 8.- Continued.



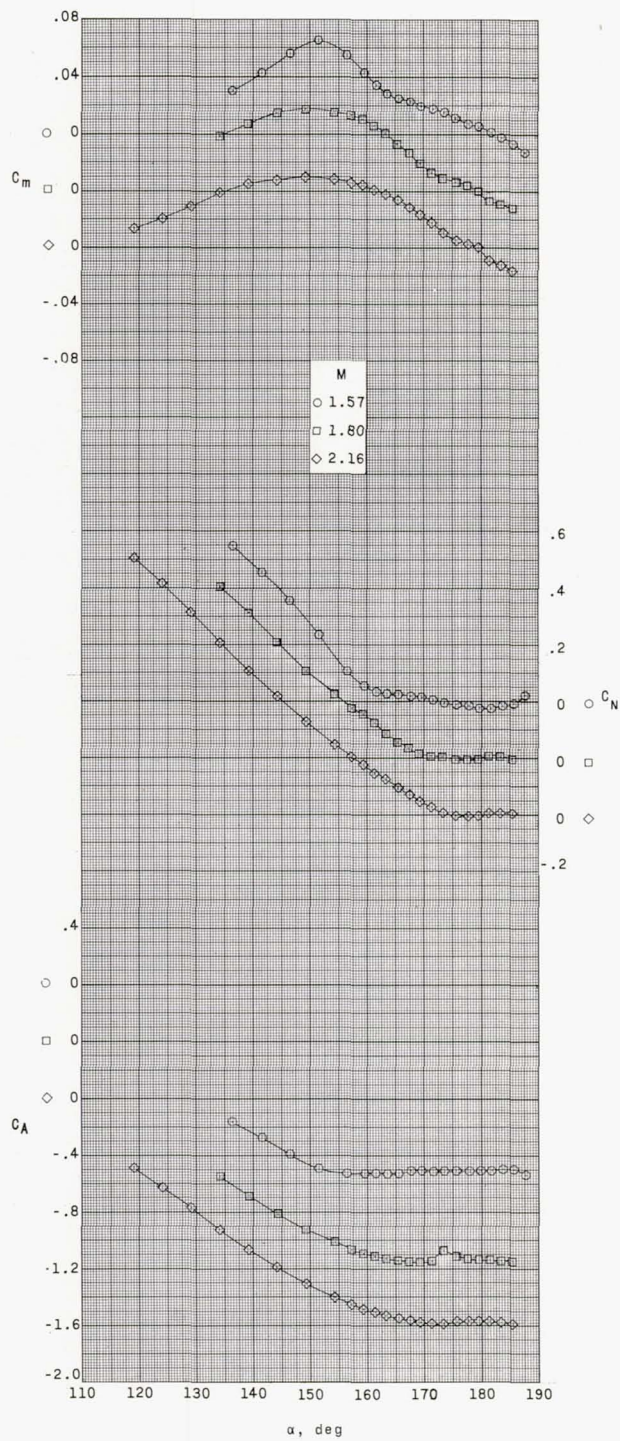
(e) Model 3231; $K = 75$ percent; $\lambda = 3/4$; $\theta = 20^\circ$; base, flat.

Figure 8.- Continued.



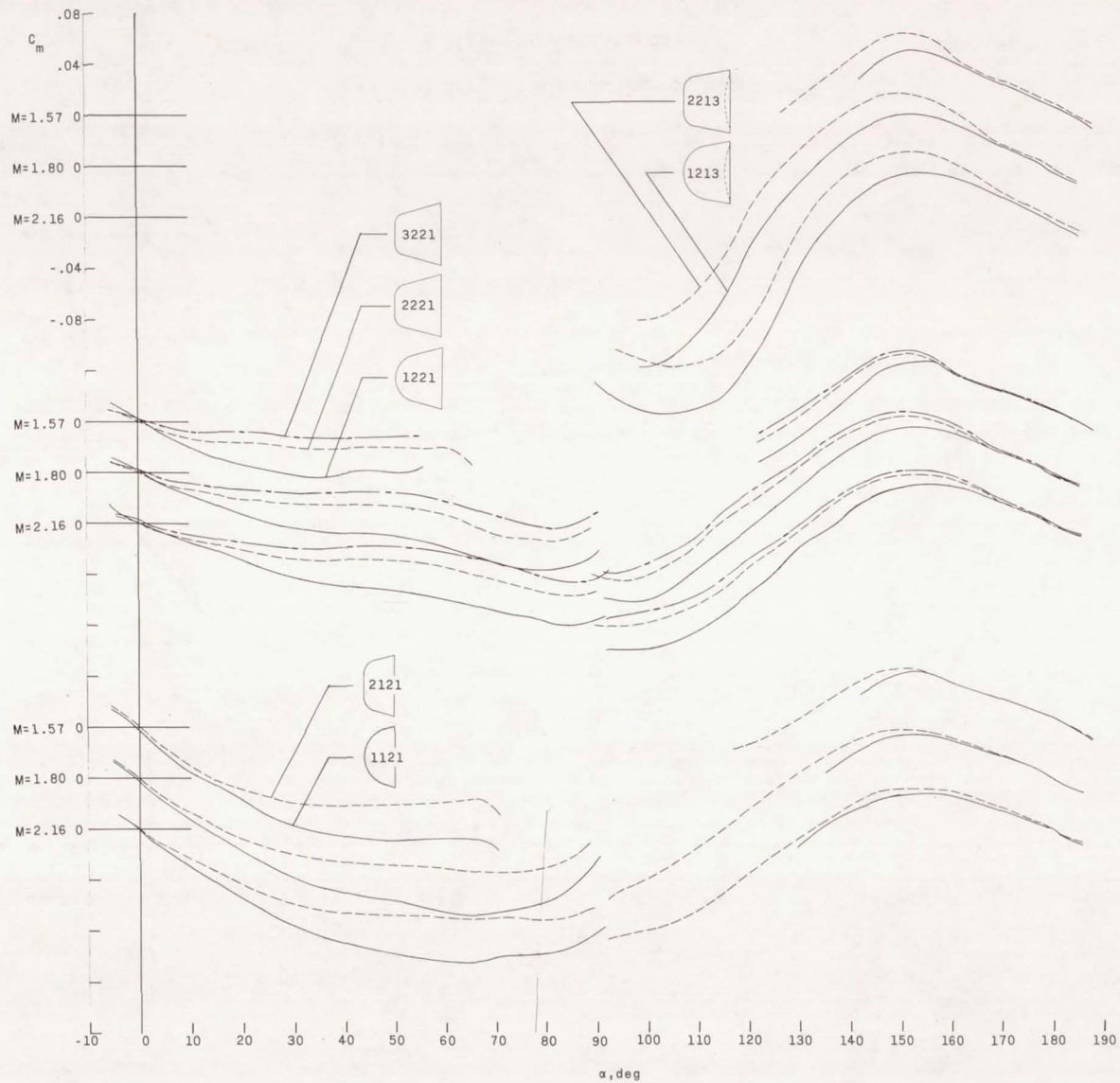
(f) Model 3321; $K = 75$ percent; $\lambda = 1$; $\theta = 15^\circ$; base, flat.

Figure 8.- Continued.



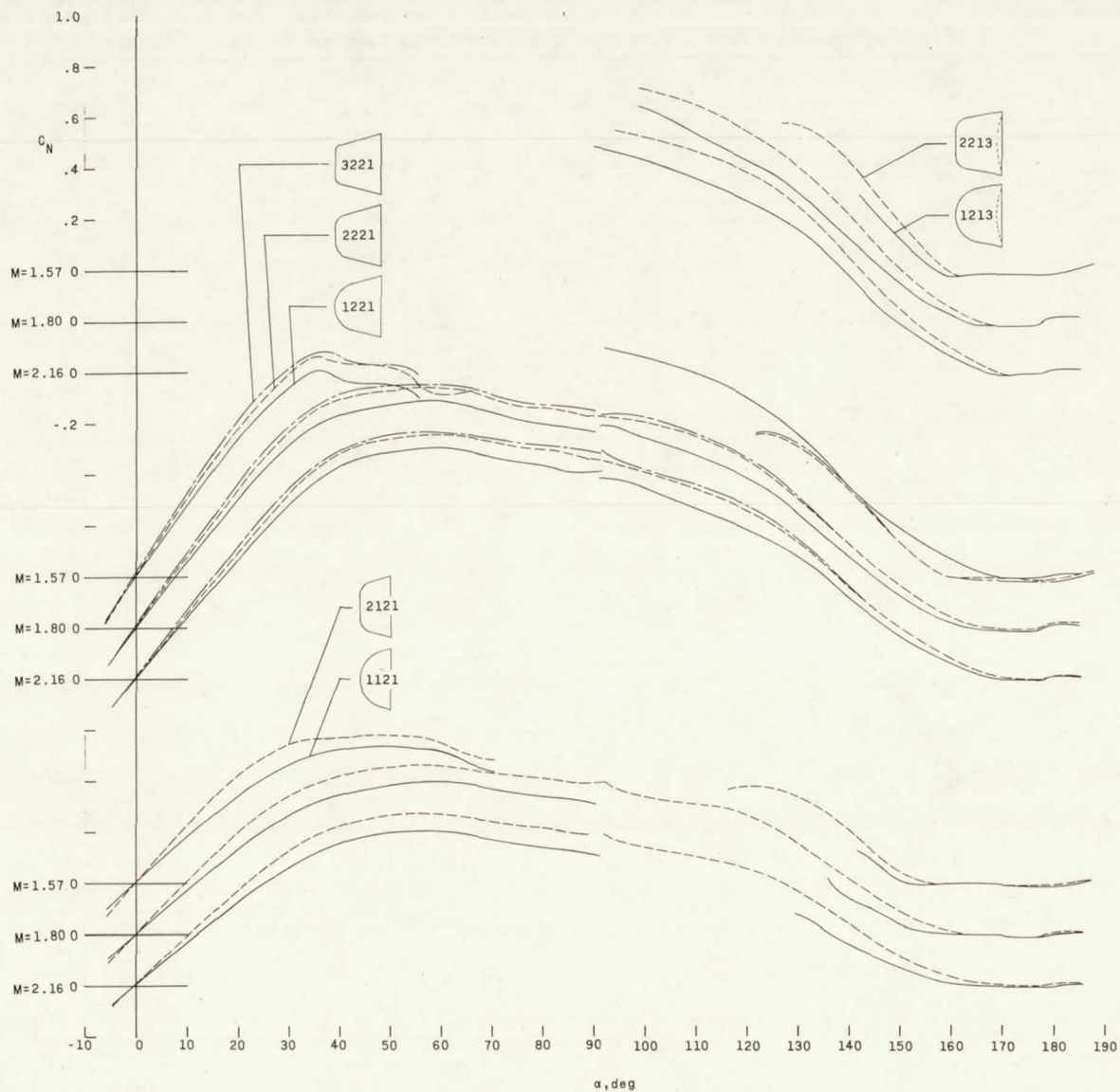
(g) Model 3322; $K = 75$ percent; $\lambda = 1$; $\theta = 15^\circ$; base, convex.

Figure 8.- Concluded.



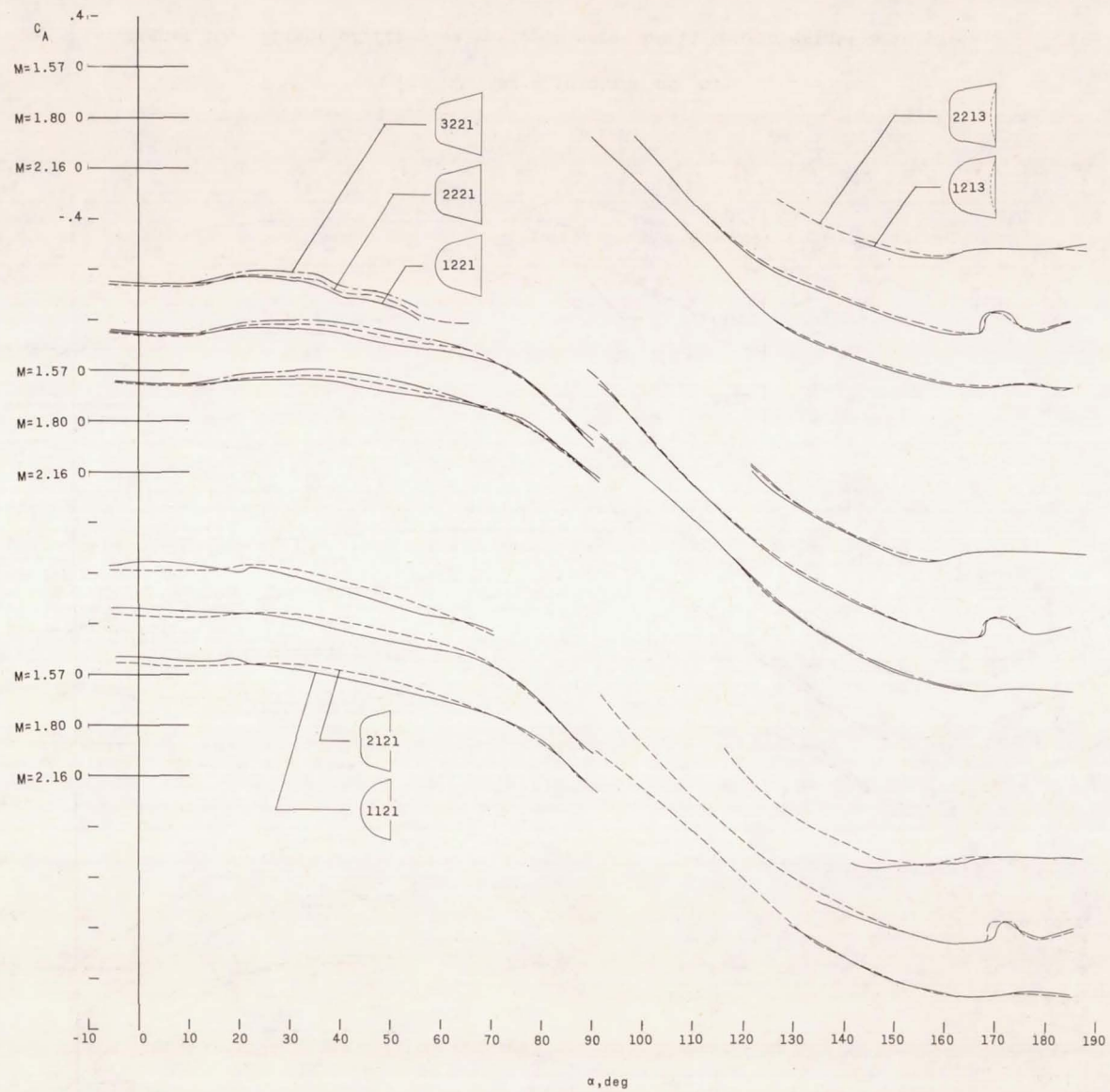
(a) C_m as a function of α .

Figure 9.- Effect of nose bluntness on aerodynamic characteristics in pitch.



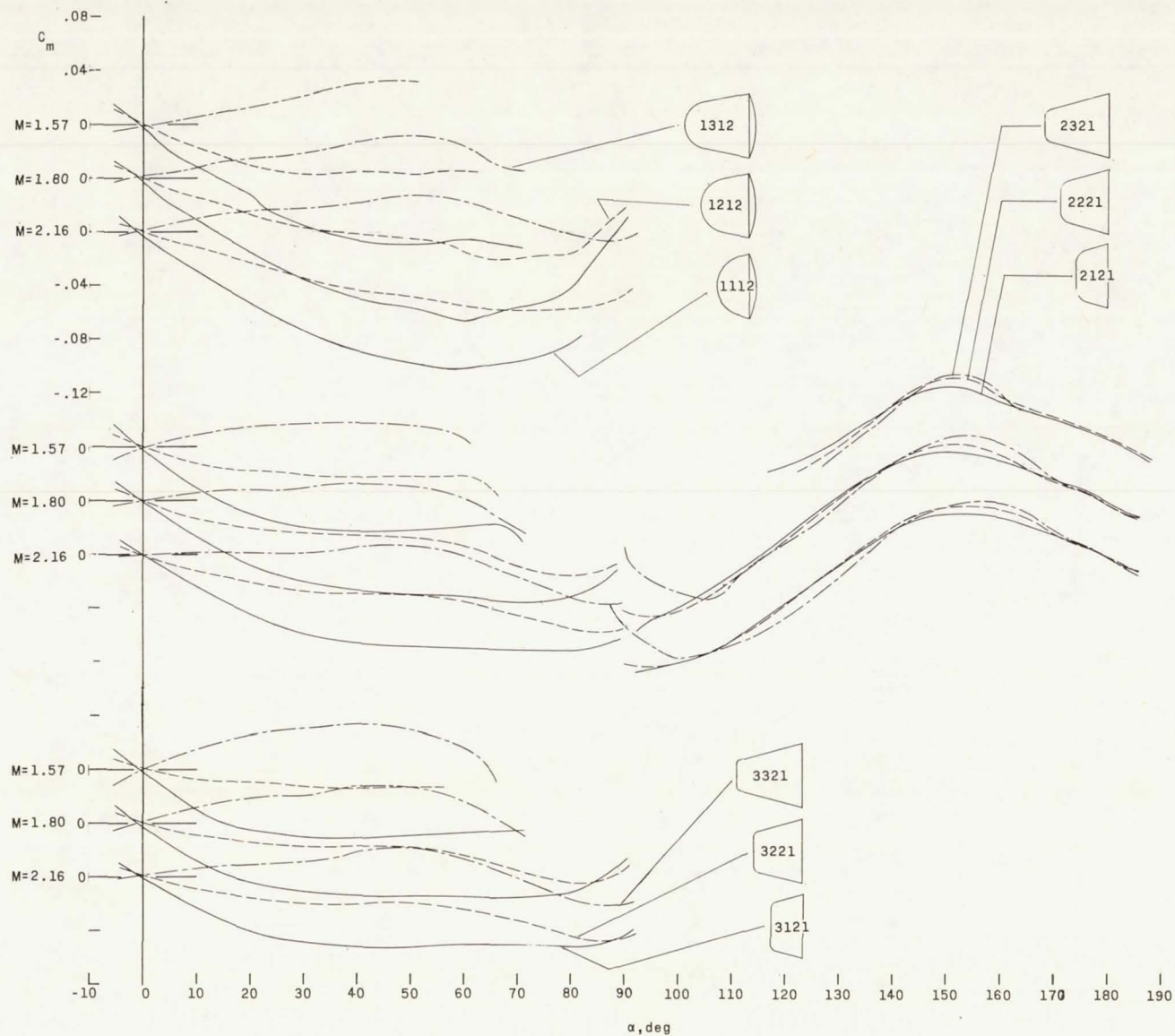
(b) C_N as a function of α .

Figure 9.- Continued.



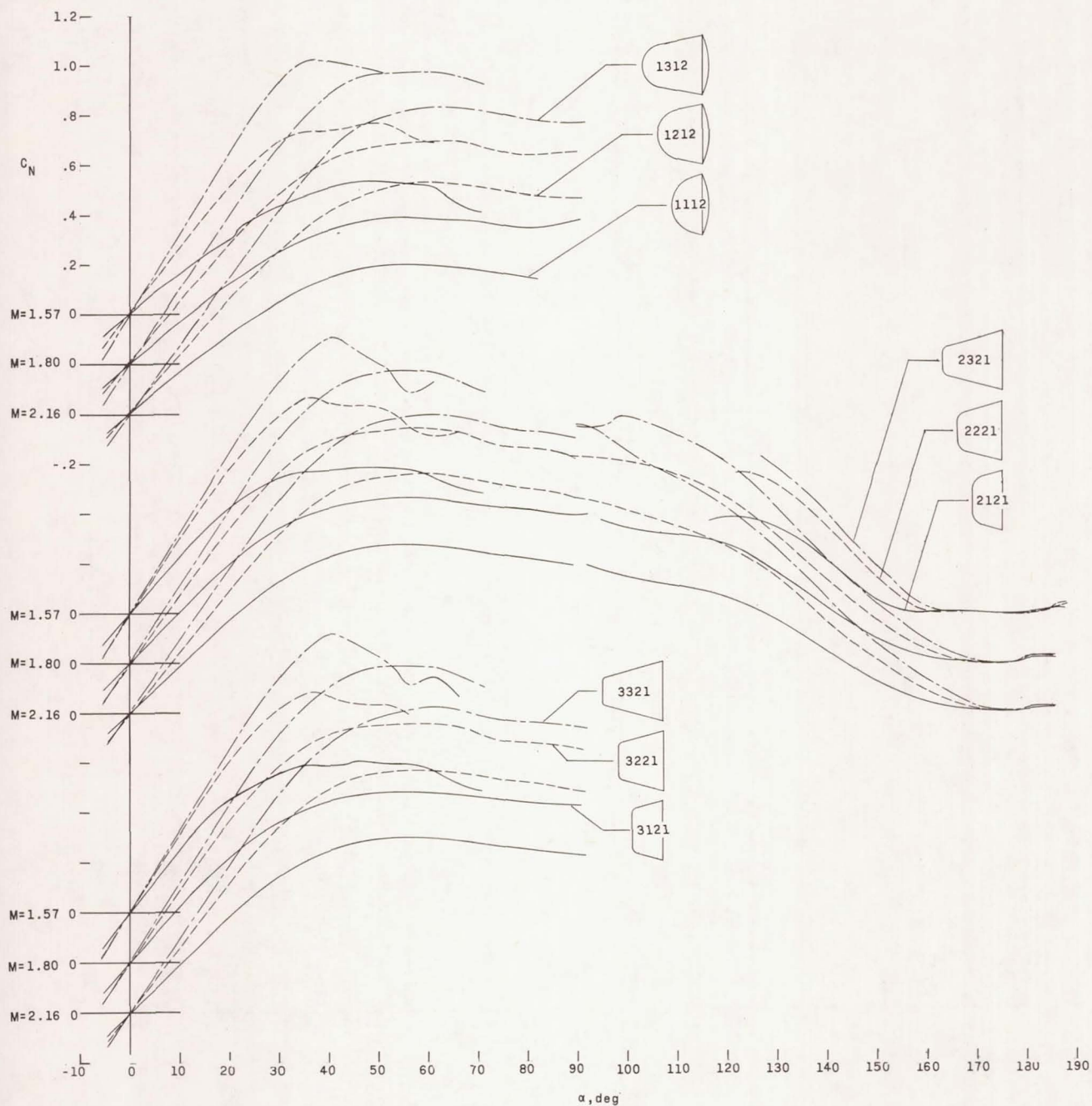
(c) C_A as a function of α .

Figure 9.- Concluded.



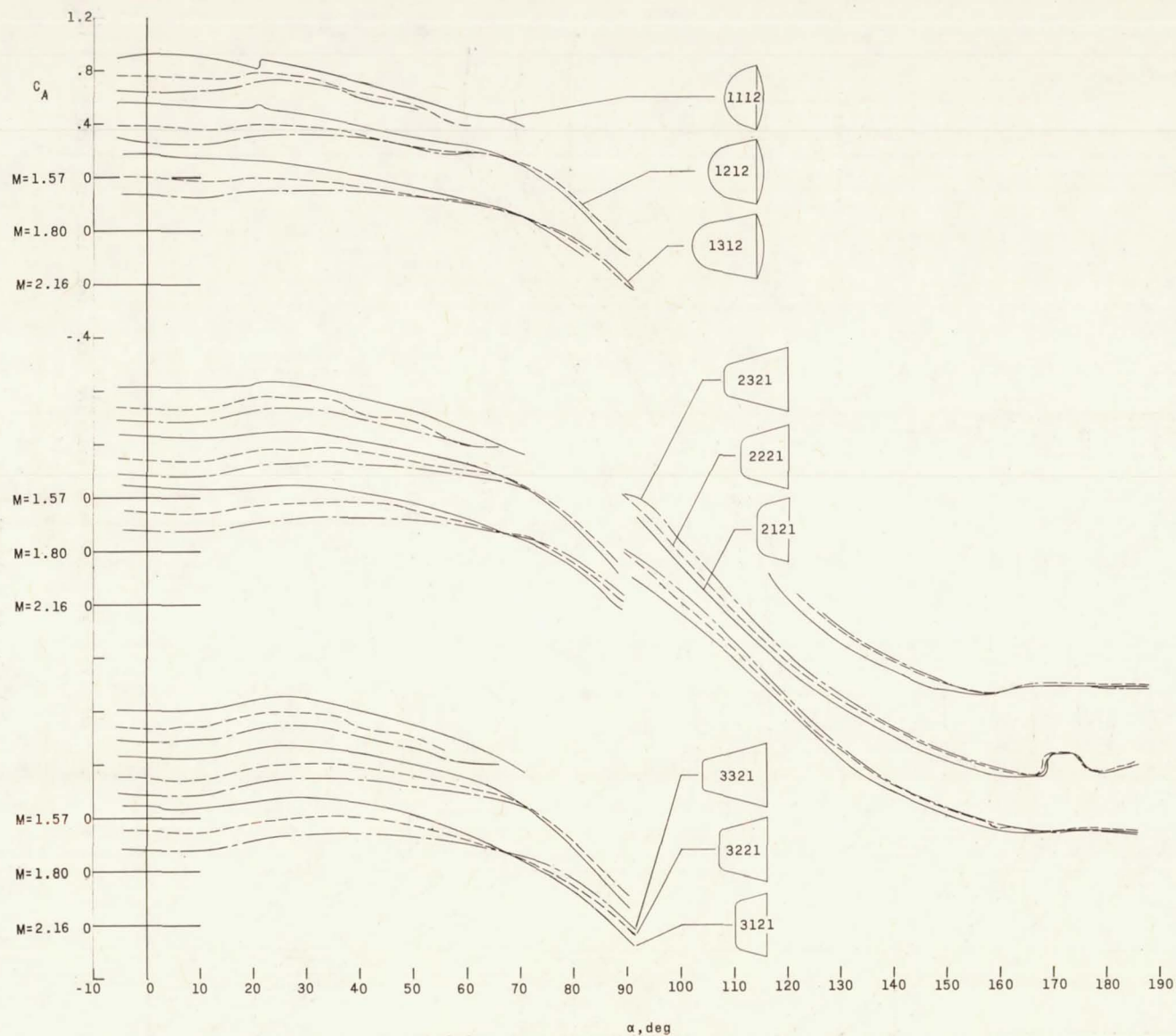
(a) C_m as a function of α .

Figure 10.- Effect of fineness ratio on aerodynamic characteristics in pitch.



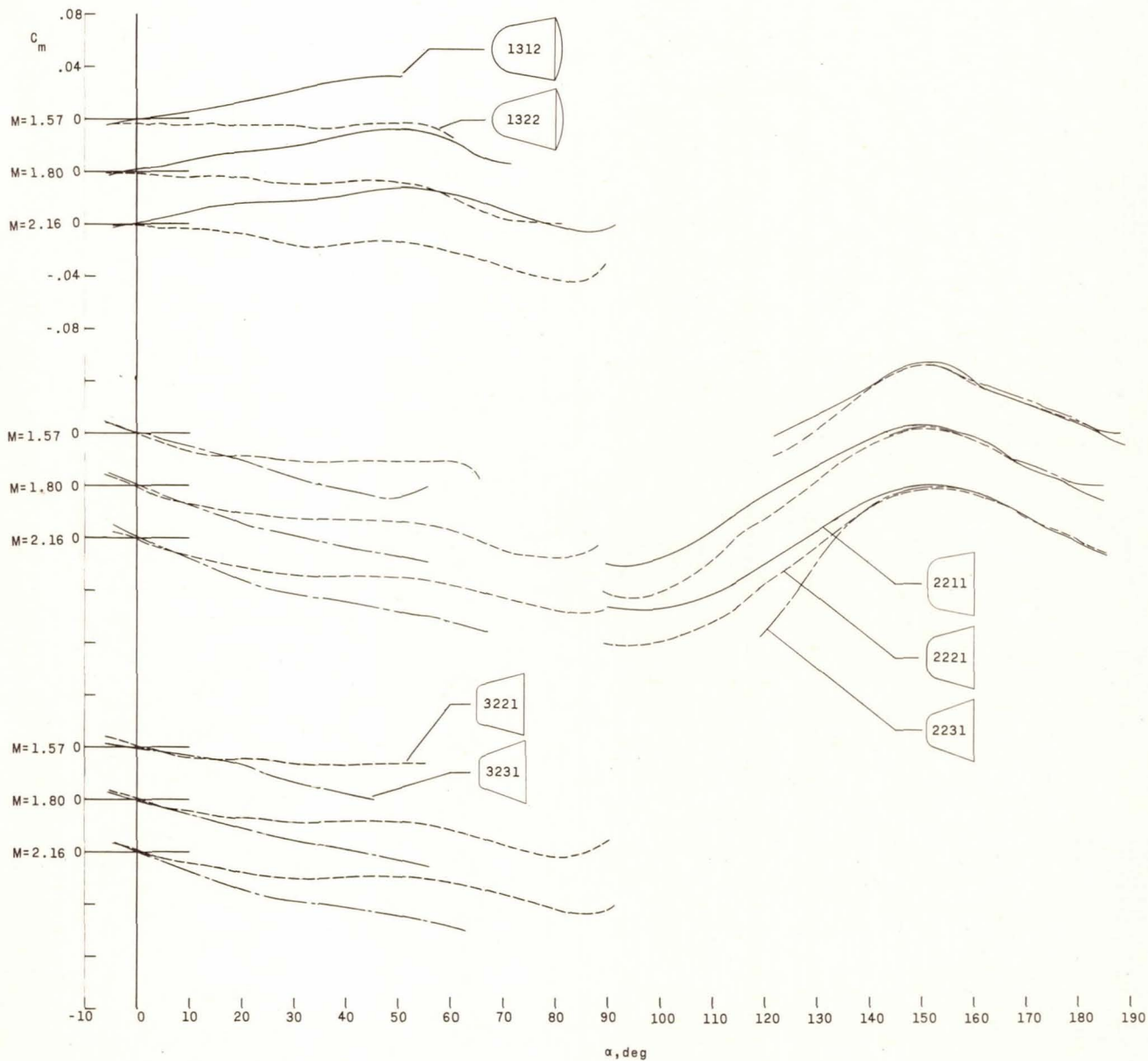
(b) C_N as a function of α .

Figure 10.- Continued.



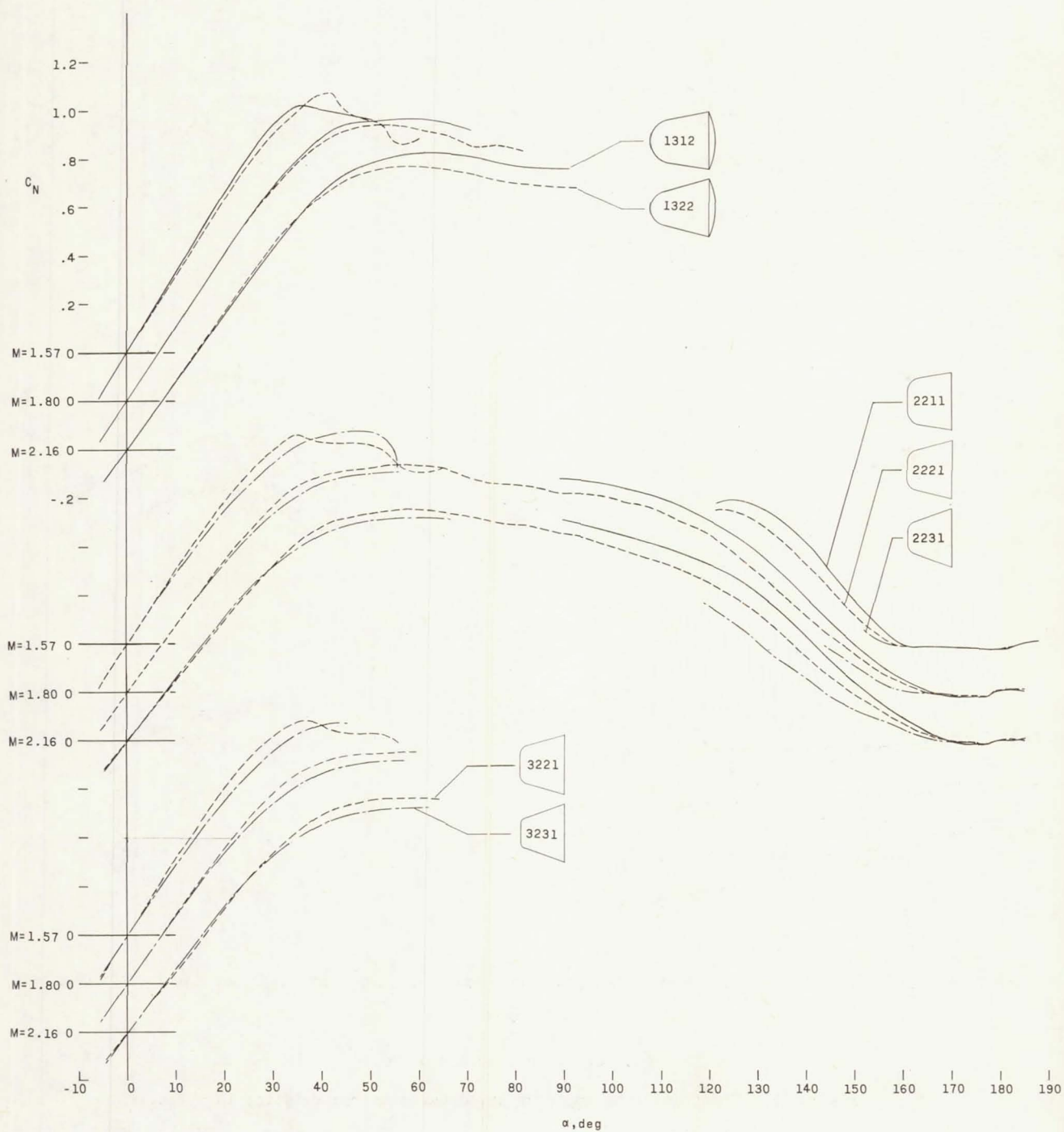
(c) C_A as a function of α .

Figure 10.- Concluded.



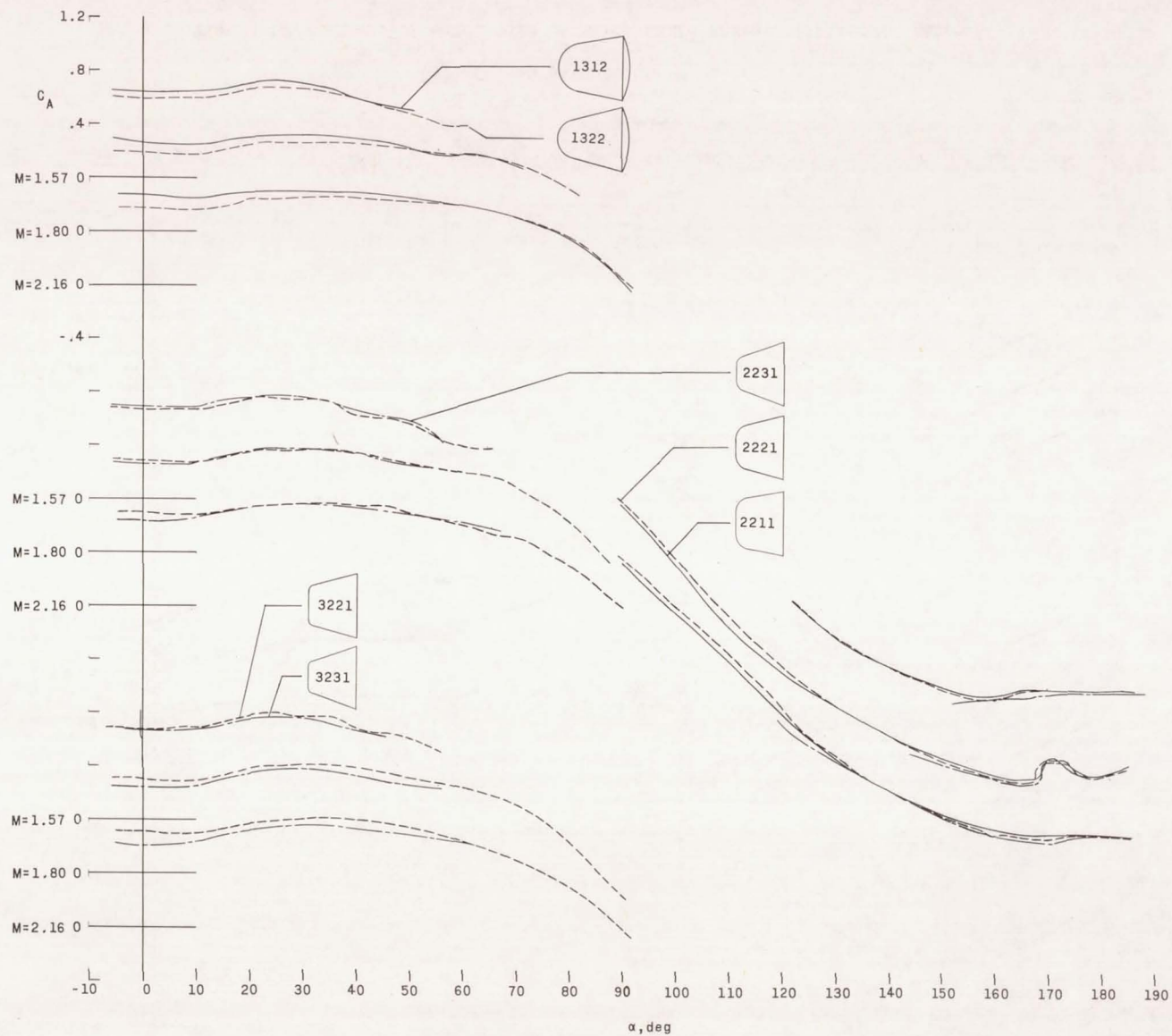
(a) C_m as a function of α .

Figure 11.- Effect of cone angle on aerodynamic characteristics in pitch.



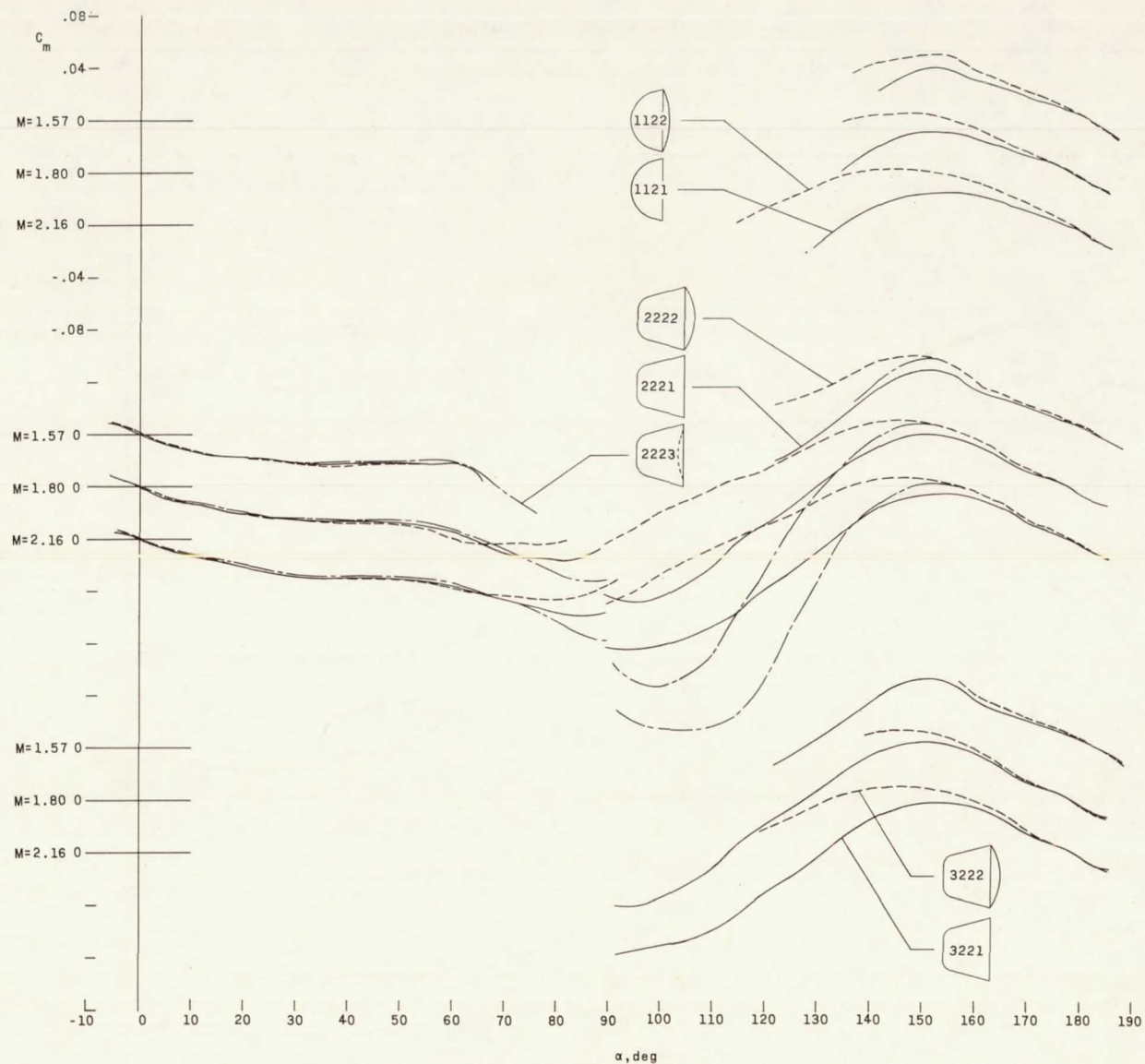
(b) C_N as a function of α .

Figure 11.- Continued.



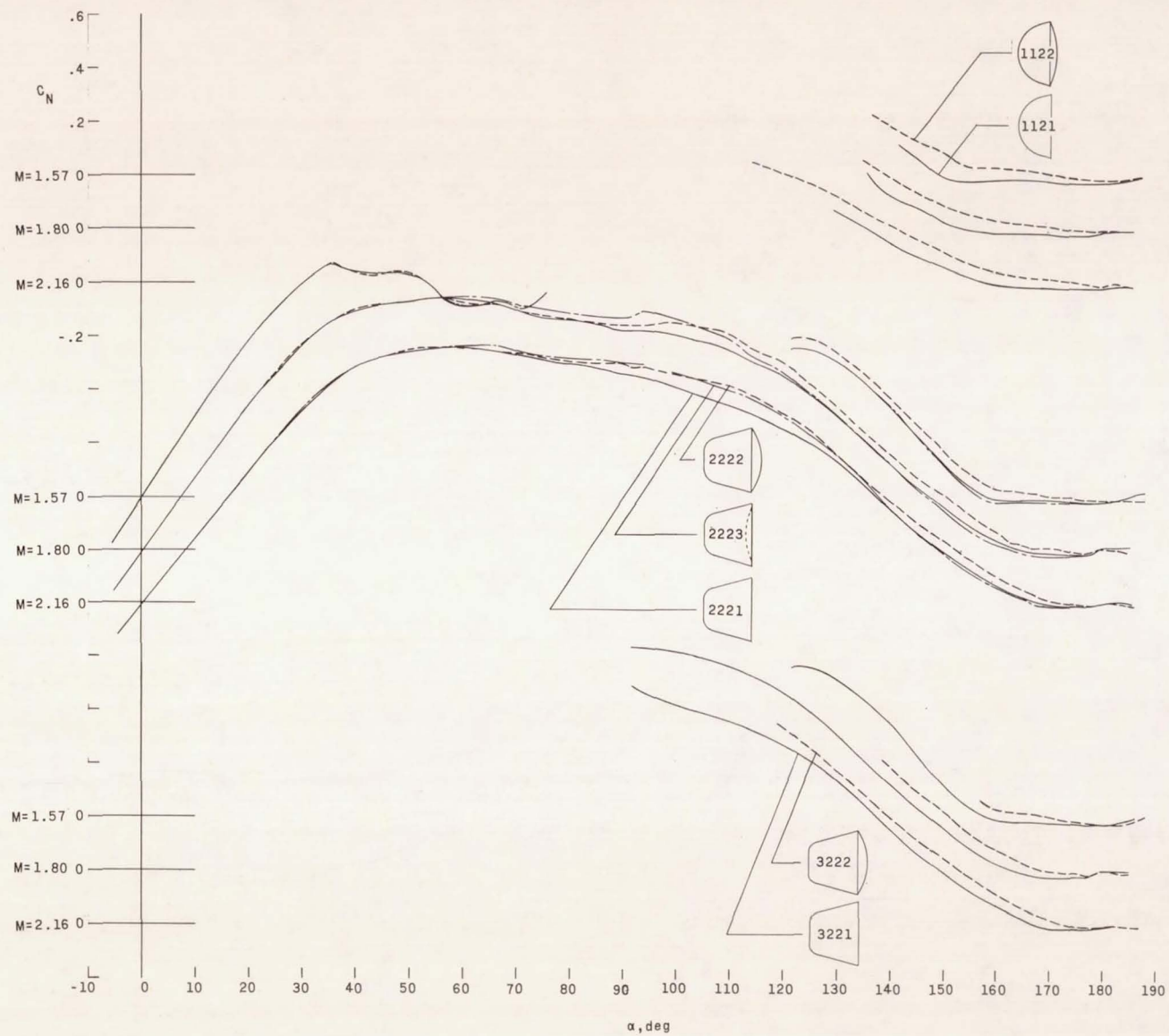
(c) C_A as a function of α .

Figure 11.- Concluded.



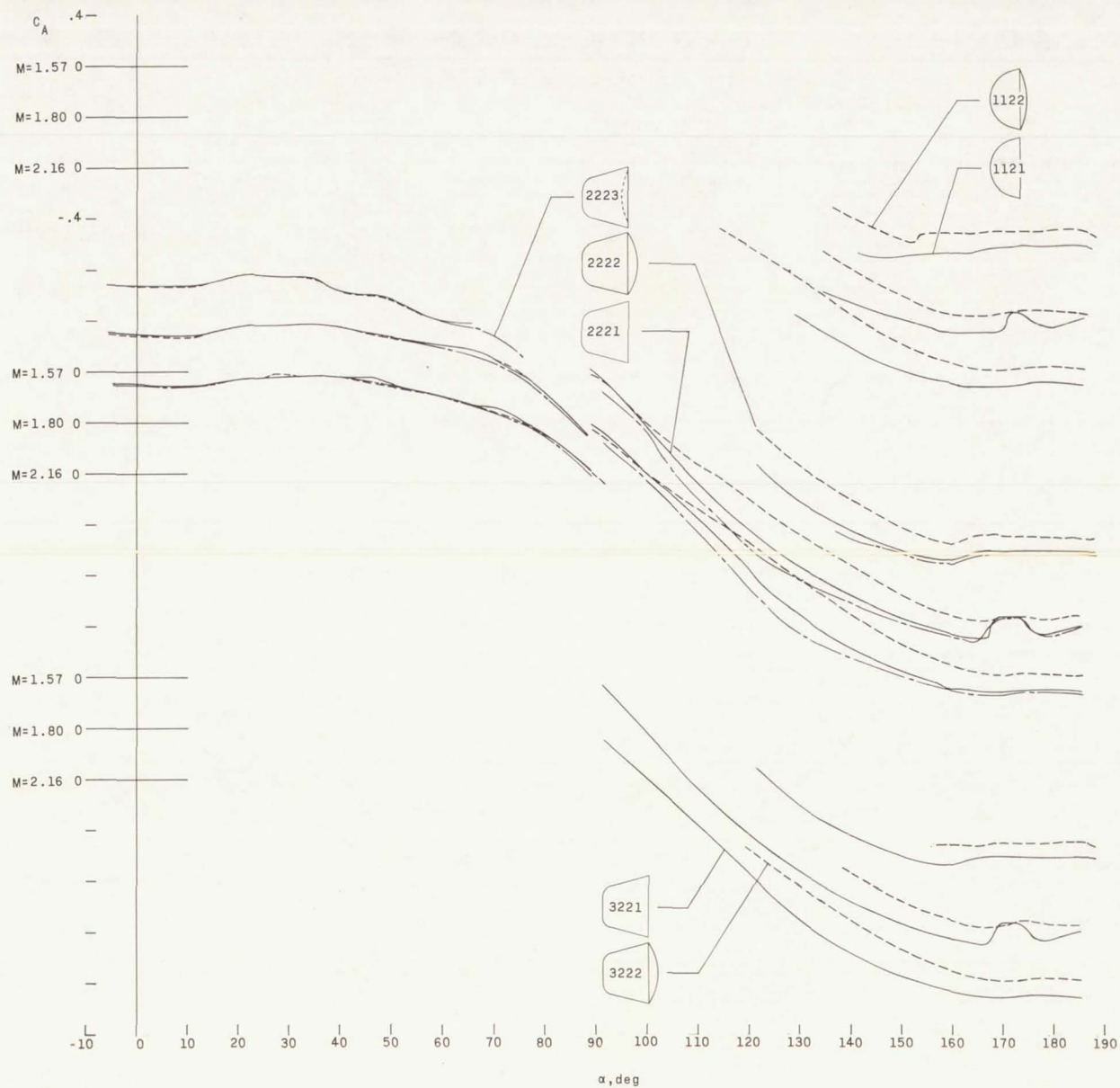
(a) C_m as a function of α .

Figure 12.- Effect of model base on aerodynamic characteristics in pitch.



(b) C_N as a function of α .

Figure 12.- Continued.



(c) C_A as a function of α .

Figure 12.- Concluded.

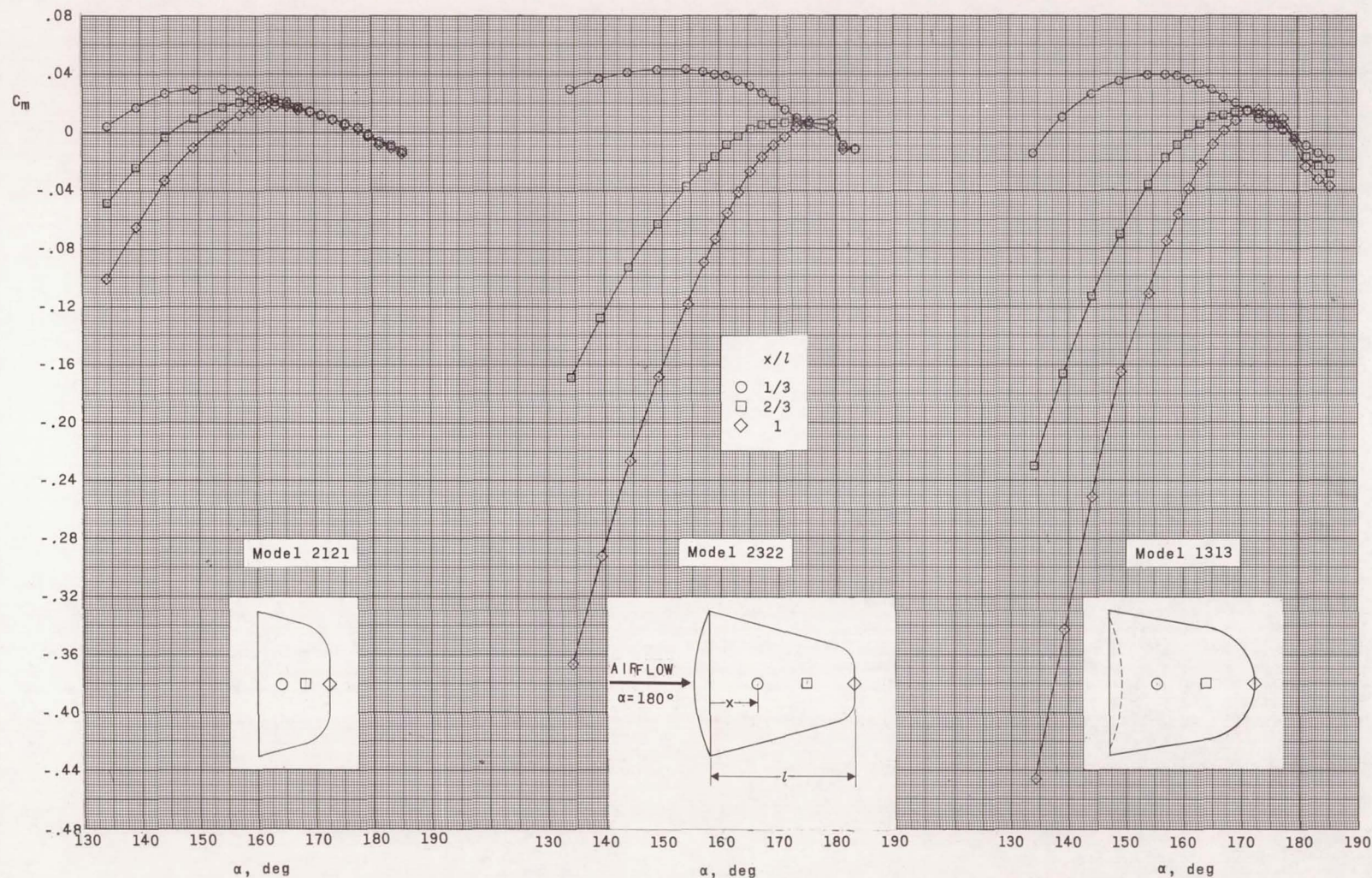


Figure 13.- Effect of longitudinal variation in moment reference center on characteristics in pitch near 180° for models 2121, 2322, and 1313 at $M = 2.16$. (Symbols denote location of moment reference center.)